ABSTRACT

Title of dissertation: HIGH RESOLUTION OPTICAL VELOCITY FIELDS OF LOW SURFACE BRIGHTNESS GALAXIES AND THE DENSITY PROFILES OF DARK MATTER HALOS

Rachel Kuzio de Naray
Doctor of Philosophy, 2007

Dissertation directed by: Professor Stacy S. McGaugh
Department of Astronomy

This dissertation investigates the behavior of cold dark matter (CDM) on galaxy scales. We present well-resolved Hα velocity fields of the central regions of 17 dark matter-dominated low surface brightness (LSB) and dwarf galaxies observed with the DensePak Integrated Field Unit. We derive rotation curves from the two-dimensional data and compare them to published long-slit and HI rotation curves. We find broad consistency between the independent data sets. Under several assumptions about the velocity contribution from the baryons, we fit the dark matter component with cuspy NFW and cored pseudoisothermal halos. We find the data to be better described by cored dark matter halos. For the majority of galaxies, NFW halo fits either cannot be made or the implied concentrations are too low for ΛCDM. The shapes of the NFW rotation curves are also inconsistent with the galaxy rotation curves. We find that CDM predicts a substantial cusp mass excess near the centers of the galaxies and that the ratio of predicted to observed dark matter increases as baryons become more important. We investigate claims that systematic effects including beam smearing, slit misplacement and noncircular motions

are responsible for slowly rising long-slit and HI rotation curves. We find the DensePak rotation curves to also be slowly rising, supporting the idea that this is an intrinsic feature of LSB rotation curves. We also model the two-dimensional NFW halo and test several modifications to the potential in an attempt to simultaneously reconcile both the NFW velocity field and rotation curve with observed galaxy data. We present mock DensePak velocity fields and rotation curves of axisymmetric and non-axisymmetric potentials. We find that a non-axisymmetric NFW potential with a constant axis ratio can reduce the cusp mass excess in the observed galaxy data, but the observer's line-of-sight must be along the minor axis of the potential, and the NFW pinch is not erased from the velocity field. We find that a non-axisymmetric NFW potential with a radially varying axis ratio tends to wash out the NFW pinch but introduces a twist to the velocity field.

HIGH RESOLUTION OPTICAL VELOCITY FIELDS OF LOW SURFACE BRIGHTNESS GALAXIES AND THE DENSITY PROFILES OF DARK MATTER HALOS

by

Rachel Kuzio de Naray

Dissertation submitted to the Faculty of the Graduate School of the
University of Maryland, College Park in partial fulfillment
of the requirements for the degree of
Doctor of Philosophy
2007

Advisory Committee:
Professor Stacy S. McGaugh, Chair/Advisor
Professor Massimo Ricotti
Professor Vera C. Rubin
Professor Roberta L. Rudnick
Professor Sylvain Veilleux
Professor Stuart N. Vogel

Preface

This dissertation examines the distribution of dark matter on galaxy scales through the optical observations of low surface brightness (LSB) galaxies. It investigates whether cuspy cold dark matter halos are consistent with high resolution Hα velocity fields of dark matter-dominated LSB galaxies. This study also investigates what conditions are necessary in order to reconcile the differences between the theory and the observations. Chapter 2 of this dissertation was published in the *Astrophysical Journal Supplement Series* as "High-Resolution Optical Velocity Fields of 11 Low Surface Brightness Galaxies" (Kuzio de Naray et al. 2006).

Acknowledgements

There have been many people over the years who have helped me get to this point in my education. Above all, I would like to thank Stacy for being my mentor and advisor. He has introduced me to some fascinating science and has provided valuable guidance on how to become a better scientist. He has supported and promoted my interests, and even made possible my unique living/working arrangement this last year. Thank you, Stacy.

I would like to acknowledge Dr. Chris Magri of the ADVANCE Program for Young Scholars for teaching my first astrophysics class in the summer after eighth grade, and Dr. Greg Carter, Dr. Marco Giardino, and the NASA Stennis Space Center for my first summer research experiences during high school. It was because of these early opportunities that I knew I wanted to become an astronomer. I would also like to thank Robin Ciardullo, my undergraduate advisor who gave me my first astronomy research project. His sincere interest in my progress and his continued friendship are greatly appreciated. The faculty and grad students at Maryland also deserve recognition for their contributions to a memorable six years.

And of course, many thanks go out to Paul and my parents and brother for their continued support and encouragement.

Table of Contents

List of Tables

List of Figures

Chapter 1

Introduction

1.1 The Current Cosmological Model

Our understanding of the universe has evolved tremendously over time. It was once believed that the Earth was flat, that the Sun and other planets revolved around the Earth, and that the universe was unchanging and not expanding. Today there is a much different picture of the universe:

- It is $\sim$ 13.7 billion years old,
- It is flat,
- It is expanding (and accelerating), and
- It is comprised of $\sim$ 4% ordinary matter, $\sim$ 23% dark matter, and $\sim$ 73% dark energy.

Living in a time of "precision cosmology," we can also give a very specific description of the universe (Spergel et al. 2007),

- $\Omega_m h^2$ (matter density) = $0.1324^{+0.0042}_{-0.0041}$
- $\Omega_b h^2$ (baryon density) = 0.02186 ± 0.00068
- H_0 (Hubble constant) = $70.4^{+1.5}_{-1.6}$

- Ω_Λ (dark energy density) = 0.716 ± 0.055
- Ω_k (spatial curvature) = -0.014 ± 0.017
- σ_8 (normalization of the power spectrum) = $0.776^{+0.031}_{-0.032}$
- n_s (scalar spectral index of the power spectrum) = 0.947 ± 0.015
- τ (optical depth) = $0.073^{+0.027}_{-0.028}$.

We can explain the expansion of the universe, the observed thermal background radiation, and the abundances of the light elements with the Big Bang. We think in the first 10^{-35} s of the universe there was a period of exponential expansion, called Inflation (Guth 1981), which enlarged quantum fluctuations to macroscopic scales and provided the origin of seeds for structure formation. When the early universe was radiation-dominated, non-baryonic cold dark matter (CDM) began clumping up in regions of overdensity. Once the universe transitioned into a matter-dominated state, baryonic matter was able to fall into the already-formed potential wells of CDM. The baryons began to first form small structures (stars and galaxies) before assembling into larger structures (galaxy clusters and superclusters), a process known as hierarchical structure formation, or "bottom-up" building. This complex scenario is thought to lead to the observed distribution of structure we see in the universe today.

1.2 Testing the Predictions of Cold Dark Matter

The framework of large scale structure formation relies heavily on the idea of cold dark matter. As such, CDM must be rigorously tested. The predictions of CDM on

large scales seem to be consistent with observations. N-body simulations successfully produce large scale filamentary structures and voids that are consistent with the findings of large galaxy surveys like the 2-degree Field Galaxy Redshift Survey (2dFGRS) and the Sloan Digital Sky Survey (see Figure 1 of Springel, Frenk, & White 2006; Springel et al. 2005). The predictions of the cuspy density profiles of CDM halos from numerical simulations (e.g., Navarro, Frenk, & White 1996, 1997) are consistent with galaxy cluster observations (e.g., Biviano & Girardi 2003; Rines et al. 2004). The linear power spectrum inferred from the Lyα forest in quasar spectra is consistent with the predictions of CDM (e.g., Croft et al. 2002). There is evidence in the 2dFGRS power spectrum for predicted baryon acoustic oscillations (e.g., Cole et al. 2005). There has also been a recent claim that collisionless dark matter was directly detected in a galaxy cluster merger known as the Bullet Cluster (Clowe et al. 2006).

What is not readily apparent is that the theory's success extends to small (galaxy) scales. For instance, there is the missing satellite problem (e.g., Moore et al. 1999a). Numerical simulations of CDM structure formation, while able to reproduce the observed abundance of galaxy clusters, predict far more satellites around Milky Way-size galaxies than are actually observed. There is also the dynamical friction time scale problem (e.g., Goerdt et al. 2006), as evidenced by the survival of globular clusters around dwarf spheroidal and dwarf elliptical galaxies. McGaugh et al. (2007) have recently used the rotation curves of 60 galaxies to show that the predicted halo density on small scales is wrong at all radii. What has arguably received the most attention, however, is the predicted density of the innermost region of galaxy dark matter halos. The conflict between the theory and observations at these small radii is known as the cusp-core problem.

1.3 The Cusp-Core Problem

One of the fundamental predictions of CDM is that all CDM halos, regardless of size, are cuspy at small radii: the density distribution shows a $\rho \sim r^{-\alpha}$ ($\alpha \gtrsim 1$) behavior (e.g., Cole & Lacey 1996; Navarro, Frenk, & White 1996, 1997; Avila-Reese, Firmiani, & Hernandez 1998; Moore et al. 1999b; Jing & Suto 2000; Klypin et al. 2001; Power et al. 2003; Reed et al. 2003; Ricotti 2003; Navarro et al. 2004; Diemand et al. 2005). Numerous studies of the rotation curves of low surface brightness (LSB) and dwarf galaxies have found the data to be inconsistent with a cuspy halo, and instead, to be more consistent with a halo having a nearly constant density core: $\rho \sim r^{-\alpha}$ ($\alpha \approx 0$) (e.g., Flores & Primack 1994; de Blok, McGaugh, & van der Hulst 1996; McGaugh, Rubin, & de Blok 2001; de Blok, Bosma, & McGaugh 2003; de Blok & Bosma 2002; Marchesini et al. 2002; Côté, Carignan, & Freeman 2000; Simon et al. 2005; Kuzio de Naray et al. 2006; Gentile et al. 2004, 2005). Cored halos such as the pseudoisothermal halo are empirical fits to the data and have no theoretical or cosmological motivation. Reconciling the predictions of numerical simulations with observations of dark matter-dominated galaxies is currently one of the greatest challenges for CDM.

1.3.1 LSB Galaxy Rotation Curve Data

There are a number of observed inconsistencies between LSB galaxy rotation curve data and the common analytic approximation of cuspy CDM halos known as the NFW halo (Navarro, Frenk, & White 1996, 1997). A simple visual comparison of rotation curves shows slowly rising LSB galaxy rotation curves that are in distinct contrast with

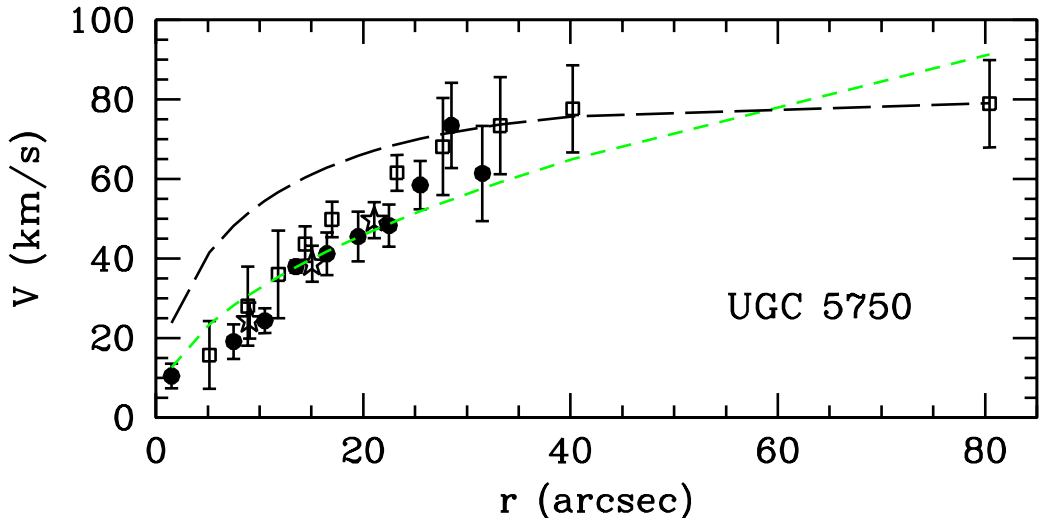

Figure 1.1: – DensePak (filled circles = Kuzio de Naray et al. (2006)) and long-slit (open squares = de Blok, McGaugh, & Rubin (2001); open stars = de Blok & Bosma (2002)) rotation curves for UGC 5750. The rotation curve predicted by CDM (black long-dash line) is much steeper than the galaxy data at small radii. The NFW fit to the data produces a rotation curve (green short-dash line) that does not match the shape of the observed galaxy rotation curve.

the steep rotation curves implied by numerical simulations. The observed linearly rising rotation curves indicate dark matter halos that have a nearly constant density core. In addition, the NFW rotation curves that are fit to galaxy data frequently have an overall shape that does not match that of the observed rotation curves (see Figure 1.1).

NFW halo fit parameters which are inconsistent with expectations for galaxies in a CDM, or more specifically ΛCDM, cosmology are also problematic. The derived concentrations from NFW fits to rotation curve data are persistently too low (e.g., de Blok, McGaugh, & Rubin 2001; de Blok & Bosma 2002; Swaters et al. 2003b; Gentile et al. 2007); CDM predicts much more massive halos than the data allow. The concentration

problem becomes even worse when baryons and physical processes in galaxy formation are taken into account. LSB galaxies are thought to be dark matter-dominated, so the velocity contribution to the rotation curve from the baryons is typically ignored (a point we return to later). When baryons are properly accounted for, the rotation velocity attributed to the dark matter is reduced, and the resulting halo concentration is even lower. Some physical processes involved in galaxy formation, such as adiabatic contraction, have the effect of increasing the halo density over its initial value (Gnedin et al. 2004), further widening the gap between the concentration allowed by the data and the concentration demanded by the theory. As a matter of statistical distribution, one should also expect to see *some* LSB galaxies with higher than nominal central densities; it is troubling that the data do not show this (de Blok & Bosma 2002; McGaugh, Rubin, & de Blok 2001). LSB galaxy rotation curves that are steeper than NFW rotation curves are not found.

Because the NFW description of dark matter halos has a direct link to cosmology, the NFW fits to galaxy rotation curves can also be used to put limits on cosmological parameters (Ω_m, σ_8, etc.). The observational constraints provided by these data are often at odds with the standard values of ΛCDM. If LSB galaxies are required to have cuspy halos, the values of cosmological parameters must be modified (McGaugh, Barker, & de Blok 2003; McGaugh et al. 2007).

1.3.2 Suggested Causes of the Cusp-Core Problem

Claims that LSB galaxy observations are incompatible with the predictions of CDM on small scales have been met with skepticism. If indeed galaxy dark matter halos are

cored rather than cuspy, then we do not understand galaxy formation in the context of CDM as well as we think. Before modifying CDM, or possibly requiring an entirely new theory, the data and systematic effects have been and are being scrutinized.

Among the earliest observations indicating cored halos were rotation curves derived from HI 21 cm velocity fields (e.g., de Blok, McGaugh, & van der Hulst 1996; Moore 1994). Beam smearing, or low spatial resolution, was suggested to have adversely affected these data (e.g., van den Bosch et al. 2000; Swaters, Madore, & Trewhella 2000). It was argued that low spatial resolution prevented cuspy halos from being distinguishable from cored halos. Subsequent long-slit Hα observations increased the spatial resolution by more than an order of magnitude (e.g., McGaugh, Rubin, & de Blok 2001; de Blok, McGaugh, & Rubin 2001) but cusps still did not appear. In only a handful of galaxies had beam smearing affected the interpretation of the data.

Systematic effects in the long-slit rotation curves have since become the focus of attention. Slit misplacement and insufficient assessment of noncircular motions are among the top systematic effects cited as afflicting long-slit data (Rhee et al. 2004; Simon et al. 2003; Spekkens, Giovanelli, & Haynes 2005; Swaters et al. 2003a). There is the concern that if the long-slit misses the dynamical center of the galaxy, then the galaxy halo will mistakenly appear cored. It has been shown more than once (e.g., McGaugh, Rubin, & de Blok 2001; de Blok & Bosma 2002; Marchesini et al. 2002), however, that multiple observations of the same galaxy by different observers give similar rotation curves. For slit misplacement to be the underlying cause of the cusp-core problem, not only must the slit position have been incorrect every time a cored galaxy halo is observed, but independent observers using different instruments on different telescopes must all make the same

mistake. Noncircular motions have also been used to try to explain cores (e.g., van den Bosch et al. 2000; Swaters et al. 2003a). The circular velocity may be underestimated when noncircular motions are present in a galaxy. Because they add in quadrature with the circular velocity, noncircular motions affect the rotation curve the most at small radii because there the magnitudes of the two velocity components are comparable. LSB rotation curve data typically require noncircular motions on the order of ~ 20 km s^{-1} in order for the data to match the predicted NFW rotation curve (de Blok, Bosma, & McGaugh 2003). Various authors have modeled long-slit data to quantify the effects of systematics. Some authors find the magnitude of these effects to be insufficient for masking the presence of a cusp (de Blok, Bosma, & McGaugh 2003), while others conclude cuspy halos cannot be ruled out (Swaters et al. 2003a).

Pinpointing the origin of the cusp-core problem has also been approached from the theoretical side. It has been proposed that dark matter itself may be to blame; rather than being cold, perhaps it is warm, self-interacting, or a type of meta-cold dark matter that initially forms cored rather than cuspy halos (e.g., Hogan & Dalcanton 2000; Strigari, Kaplinghat, & Bullock 2007). It may also be possible that cusps are destroyed by non-cosmological effects such as extremely explosive feedback or other methods of drastically redistributing the mass, although the effectiveness of such processes is uncertain (see McGaugh, Barker and de Blok (2003) and references therein). The numerical simulations themselves may also contribute to the discrepancy. While simulations may neglect to include relevant galaxy formation physics, such as adiabatic contraction, a more important drawback may be that both past and recent (Hayashi et al. 2004) numerical simulations lack the resolution required to fully describe CDM halos on the scale of an individual

galaxy. Simulations do not have adequate resolution at scales $\lesssim 1$ kpc, the critical resolution at which observations make distinctions between cusps and cores (de Blok 2003).

1.4 This Dissertation

1.4.1 Scientific Approach

To determine the radial density distribution of galaxy-size dark matter halos, what is needed, but not provided by the existing data, is a large sample of observations that simultaneously provides sub-kiloparsec resolution and two-dimensional information. It is the goal of this dissertation to provide these data.

We target LSB galaxies because they are thought to be dark matter-dominated down to small radii (de Blok & McGaugh 1996, 1997; but see Fuchs 2003), with the light simply providing a tracer for the dark matter. The stellar mass contribution is low, which reduces errors involving the uncertainty in the stellar mass-to-light ratio, and in turn, the isolation of the dark matter component. The observed galaxies are nearby so that we can obtain the critical sub-kiloparsec resolution necessary for distinguishing between cusps and cores. Our initial primary sample consists of 19 LSB galaxies having well-resolved long-slit Hα observations that show decent Hα emission for detectability in two-dimensional velocity fields, a lack of significant noncircular motions, and strong evidence for halos which prefer cores rather than cusps (de Blok & Bosma 2002; de Blok, McGaugh, & Rubin 2001; McGaugh, Rubin, & de Blok 2001). A large number of these galaxies also have HI 21 cm observations (van der Hulst et al. 1993; de Blok, McGaugh, & van der Hulst 1996).

We use the DensePak Integrated Field Unit (IFU) on the WIYN telescope at the Kitt

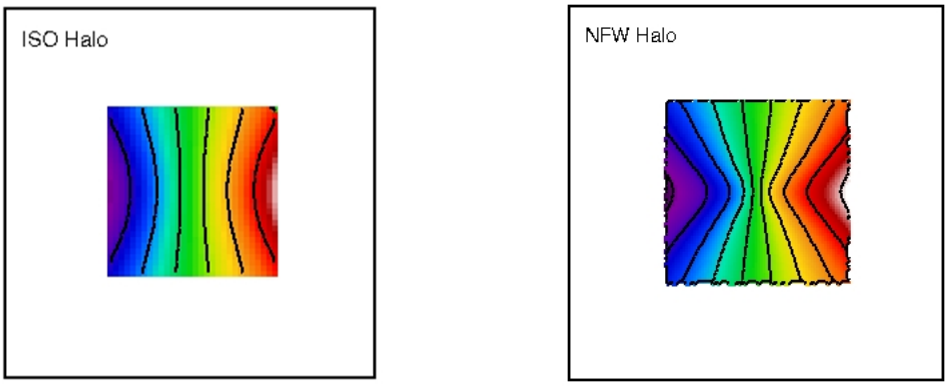

Figure 1.2: – *Left:* Isothermal (R_c = 1 kpc; V_∞ = 100 km s^{-1}) velocity field. *Right:* NFW (c = 8.6; V_{200} = 100 km s^{-1}) velocity field. Both velocity fields are inclined at 60° and have isovelocity contours at 10 km s^{-1} intervals. The NFW halo shows a distinctive pinch of the isovelocity contours compared to the gently rounded isovelocity contours of the cored isothermal halo.

Peak National Observatory to obtain Hα velocity fields of the centers of our sample of galaxies. Well-resolved optical velocity fields have a number of benefits over the equally well-resolved long-slit Hα observations. Cuspy NFW halos leave a distinctive signature in two-dimensional velocity fields (see Figure 1.2). The isovelocity contours are pinched, and the presence of this pinch, or lack thereof, can be used as an indication of whether or not the halo is cuspy. As these new data cover *x*-*y*-*v* space, proper placement of a single slit across the dynamical center of the galaxy is no longer a concern. Noncircular motions should be readily identifiable in a well-resolved velocity field, allowing concerns about their effects to be addressed. These velocity fields also provide an additional important constraint on the underlying dark matter halo potential. For instance, boosting the observed rotation curve with noncircular motions may make the rotation curve look NFW, but the observed velocity field must also be consistent with the velocity field of an NFW

halo + noncircular motions. Should the NFW potential be modified, or an entirely different halo potential be proposed, the resulting velocity field must be shown to be consistent with the observed velocity fields.

1.4.2 Goals and Overview

Using well-resolved optical velocity fields of the central regions of a large sample of LSB and dwarf galaxies, we aim to investigate the following questions in this dissertation:

1. Are galaxy rotation curves derived from well-resolved optical velocity fields more consistent with the cuspy NFW halos predicted by CDM or by cored isothermal halos?

2. How do these new rotation curves compare to rotation curves from previous long-slit and HI studies? How do the NFW halo fits compare? Have systematic effects significantly impacted the interpretation of these previous data?

3. If the NFW halo is inconsistent with the data, what level of noncircular motions are required to resolve this discrepancy, and are those noncircular motions consistent with constraints provided by the data?

4. Can a modification to the NFW halo potential, such as the introduction of an asymmetry, simultaneously cause the NFW velocity field to appear solid-body and the NFW rotation curve to appear linearly rising?

In Chapters 2 and 3 we present Hα velocity fields and derived rotation curves for 17 LSB and dwarf galaxies observed with the DensePak IFU. We also present the NFW

and pseudoisothermal halo fits to the dark matter halos. We compare our rotation curves and halo fits to published long-slit and HI results. In Chapter 4 we consider the effect of baryons and present isothermal and NFW halo fits for four assumptions of the stellar mass-to-light ratio. We also investigate what magnitude of noncircular motions are necessary to reconcile the NFW halo with the observations. In Chapter 5 we simulate the two-dimensional NFW halo and test several modificiations to the potential in an attempt to simultaneously reconcile both the NFW velocity field and rotation curve with observed LSB galaxy data. We summarize our main results and conclusions in Chapter 6.

Chapter 2

High-Resolution Optical Velocity Fields of 11 Low Surface Brightness Galaxies

Kuzio de Naray, R., McGaugh, S.S., de Blok, W.J.G., & Bosma, A. 2006, ApJS, 165, 461

2.1 Abstract

We present high-resolution two-dimensional velocity fields from integral field spectroscopy, along with derived rotation curves for 11 low surface brightness galaxies. We fit NFW and pseudoisothermal halo models to the new data combined with previous long-slit and HI data. In most cases, we find the pseudoisothermal halo to better represent the data than the NFW halo, as the NFW concentrations are often lower than expected for a ΛCDM cosmology. We also compare our results to previous studies and find that including the new two-dimensional optical data does not significantly alter the halo parameters but does decrease the uncertainties by roughly a factor of 2.

2.2 Introduction

Determining the mass density profiles of galactic dark matter halos has been an exciting, yet contentious, field for a number of years now. Although it is widely agreed that low surface brightness (LSB) galaxies are dark matter–dominated down to small radii (de Blok & McGaugh 1996, 1997; Pickering et al. 1997, 1999; Blais-Ouellette, Amram, & Carignan 2001; Borriello & Salucci 2001; Simon et al. 2003; but see Fuchs 2003) and, hence, are ideal test subjects for studying the dark matter distribution, a consensus on the interpretation of their rotation curves has been difficult to achieve.

The disagreement arises when comparing the data to numerical simulations of cold dark matter (CDM). The most common description of CDM halo behavior is given by the analytic approximation of Navarro, Frenk, & White (1996, 1997) and is known as the NFW profile. The cosmologically motivated NFW halo is characterized by a mass density that rises very steeply toward the center, a property which makes the halo "cuspy." Cuspy halos that rise more steeply than the NFW halo have also been suggested (e.g., Moore et al. 1999b; Reed et al. 2003; Navarro et al. 2004; Diemand et al. 2005). Whether or not the dark matter halos of LSB galaxies can be described by cuspy NFW-like profiles has been a matter of debate.

NFW halos can be fitted to the observations, but the fits are usually of lower quality than fits with pseudoisothermal halos. Moreover, the implied cosmological parameters are inconsistent with the standard ΛCDM picture. In particular, the observed concentrations of the NFW halos are too low (McGaugh, Barker, & de Blok 2003; Swaters et al. 2003b). Much better fits to LSB observations are found when using the pseudoisothermal halo

model (Simon et al. 2005; de Blok, Bosma, & McGaugh 2003; de Blok & Bosma 2002 (hereafter BB02); Marchesini et al. 2002; Bolatto et al. 2002; de Blok, McGaugh, & Rubin 2001 (hereafter BMR01); de Blok et al. 2001; Blais-Ouellette, Amram, & Carignan 2001; Côté, Carignan, & Freeman 2000). These halos have a mass density that remains at an approximately constant value toward the center; thus, they are referred to as "cored" halos. Unlike the NFW profile, however, the pseudoisothermal halo has no cosmological motivation or theoretical basis.

In its favor, the CDM model has been successful on large scales in explaining structure formation in the early universe, as well as abundances of galaxy clusters (Tegmark et al. 2004). It is more appealing to have a halo model with explanations rooted in cosmology than a model that is simply a convenient fit to the data. It is therefore no surprise that a number of reasons have been given in an attempt to salvage the appropriateness of the NFW profile as a description of galactic dark matter halos.

The earliest observations which indicated cores in LSB galaxies were two-dimensional 21 cm HI velocity fields (Moore 1994; Flores & Primack 1994; de Blok, McGaugh, & van der Hulst 1996, hereafter BMH96). Low spatial resolution (i.e., beam smearing) was suggested to be a systematic effect that would erroneously indicate cores (van den Bosch et al. 2000; Swaters, Madore, & Trewhella 2000). The question of beam smearing was addressed by long-slit Hα observations, which had an order-of-magnitude increase in spatial resolution (see for example, McGaugh, Rubin, & de Blok 2001 [hereafter MRB01]; BMR01); cusps did not appear when the resolution was increased, showing that beam smearing had been of only minor importance in the HI observations. Possible systematic errors in the long-slit spectroscopy (e.g., Simon et al. 2003; Rhee et al. 2004;

Spekkens, Giovanelli, & Haynes 2005) have since become the focus of attention, with slit misplacement (Swaters et al. 2003a) and noncircular motions among the top concerns. If the slit misses the dynamical center of the galaxy or if there are noncircular motions from, for instance, a bar, the circular velocity may be underestimated and lead to the false inference of a cored halo. de Blok, Bosma, & McGaugh (2003) conducted extensive modeling in which the rotation curves of both cuspy and cored halos were subjected to various effects and concluded that no systematic effect will entirely mask the presence of a cuspy halo for realistic observing conditions. Swaters et al. (2003a) performed a similar exercise with similar results but argued that it might still be possible to retain cuspy halos.

Clearly, there are a number of issues that new observations must simultaneously address. The data must be both high-resolution and two-dimensional in nature. Observations must have resolution $\lesssim$ 1 kpc, as that is the critical length scale at which the distinction between cusps and cores can be determined (de Blok 2003). Any noncircular motions should be readily identifiable in a two-dimensional velocity field. In addition, slit placement is not a concern of two-dimensional velocity fields. This observational approach has also been applied by such groups as Simon et al. (2003, 2005).

In this paper, we present the rotation curves derived from high-resolution two-dimensional velocity fields of a sample of LSB galaxies. In § 2.3, we discuss the sample and observations; data reduction is discussed in § 2.4. The results for the individual galaxies are presented in § 2.5. In § 2.6, we discuss halo fits to the minimum-disk case of the new data combined with previous long-slit and HI rotation curves and compare our results to those of previous studies. Noncircular motions are also briefly discussed. Our conclusions and goals for future work are stated in § 2.7.

2.3 Sample and Observations

Our primary targets were the galaxies in the "clean" sample of de Blok, Bosma, & McGaugh (2003). In brief, galaxies in the "clean" sample have inclinations between 30° and 85°, are likely to meet the minimum-disk assumption, have long-slit rotation curves that are well resolved in the inner 1 kpc, have small error bars, and lack large asymmetries. The minimum-disk assumption is considered applicable to those galaxies that require substantial amounts of dark matter at small radii even in the maximum-disk model. We then expanded our sample to include other LSB galaxies that nearly made the "clean" cut. We also searched for low-mass dwarf galaxies to fill out the range of right ascension available at the telescope, giving preference to those targets with diffuse Hα emission detected by long-slit observations.

We observed eight "clean" galaxies: UGC 4325, DDO 64, NGC 4395, F583-4, F583-1, DDO 185, DDO 189, and NGC 4455. These galaxies were selected from the "clean" sample because the well-resolved long-slit Hα observations (BB02;BMR01) show that there is diffuse Hα emission for detectability in two-dimensional velocity fields and that the galaxies lack indicators of significant noncircular motions (e.g., strong bars or gross asymmetries). While not a criterion considered in the selection process, it turns out that the long-slit observations of these galaxies imply that the galaxies either have unreasonably low NFW concentrations or do not have cusps at all. These kinds of galaxies pose the biggest problem for CDM and, as such, provide important test cases.

We observed four galaxies from MRB01 (F563-V2, F563-1, F568-3, and UGC 5750) that almost made the "clean" sample. They show diffuse Hα emission but either

did not have the required number of independent points in the inner 1 kpc of the long-slit rotation curve or had an inclination outside the "clean" range.

Finally, we observed 16 galaxies from the Nearby Galaxies Catalogue (Tully 1988). Selection criteria for these galaxies included positions satisfying $18^h \lesssim \alpha \lesssim 08^h$ and +10° $\lesssim \delta \lesssim$ +50°, inclinations between 30° and 85°, heliocentric velocities $\lesssim$ 2500 km s^{-1}, and an estimated V_{flat} (approximated by $V_{flat} \sim 0.5 W_{20} sin^{-1} i$) between roughly 50 km s^{-1} and 100 km s^{-1}.

Our sample of 28 observed galaxies is both weather- and signal-limited. Poor weather prevented us from observing more of the "clean" sample. Our sample is signal-limited in that not all of the galaxies have enough Hα emission to construct useful velocity fields. While preexisting long-slit observations can be used as a guide, there is no way of knowing how much Hα emission will be detected by the integrated field unit (IFU) until the experiment is done. Our sample is intentionally focused on the most dark matter–dominated objects. These tend to be very low surface brightness dwarfs that are hard to observe.

The galaxies were observed during the nights of 2004 April 12-15, 2004 November 14-19, and 2005 September 1-7. Observations were made using the DensePak IFU on the 3.5 m WIYN[1] telescope at the Kitt Peak National Observatory (KPNO). DensePak is comprised of 3″ diameter fibers arranged in a 43″ × 28″ rectangle. We measured the fiber separation to be 3″.84. The separation was determined by centering a bright star in a fiber

[1]Based on observations obtained at the WIYN Observatory. The WIYN Observatory is a joint facility of the University of Wisconsin-Madison, Indiana University, Yale University, and the National Optical Astronomy Observatory.

and repeatedly shifting between fibers and across the array. There are 85 working fibers in this arrangement; an additional four sky fibers are arranged outside the main bundle. We used the 860 line mm^{-1} grating in second order, centered near Hα, giving a 58 km s^{-1} velocity resolution. The distances to the galaxies in the sample are such that a $3''$ fiber provides subkiloparsec resolution.

Because the galaxies were too faint to be visible on the guide camera, we centered the DensePak array on a nearby star and then offset to the optical center of the galaxy. Subsequent pointings on the galaxy were made by shifting the array by small amounts from its current position. For a number of galaxies, these moves were the fine shifts required to observe the spaces between the fibers. These interstitial pointings effectively increased the resolution to $\sim 2''$. The fiber bundle orientation on the sky and the total number of pointings per galaxy were tailored to each galaxy so that the critical central regions were covered by the DensePak fibers. Each exposure was 1800 s, and two exposures were taken at each pointing. A CuAr lamp was observed before and after each pointing to provide wavelength calibration.

2.4 Data Reduction

The observations were reduced in IRAF [2] using the HYDRA package. The data were bias-subtracted and flattened. The IRAF task `dohydra` was used to extract the spectra. A wavelength solution created from the observations of the CuAr lamp was applied

[2]IRAF is distributed by the National Optical Astronomy Observatory, which is operated by the Association of Universities for Research in Astronomy (AURA), Inc., under agreement with the National Science Foundation.

to the spectra. The two exposures per pointing were combined to increase the signal-to-noise ratio and to remove cosmic rays. Sky subtraction was not performed, because the DensePak sky fibers often fell inside the galaxies rather than on the sky and were therefore contaminated by galactic emission. We made use of the night-sky emission lines by using them as the reference wavelengths (Osterbrock et al. 1996) by which the velocities of the galactic emission lines were measured. We also tried using the CuAr calibration to measure the velocities, but the night-sky lines gave cleaner results. Velocities were measured by fitting Gaussians to both the sky lines and the four galactic emission lines of interest: Hα, [N II]λ6584, [S II]λ6717, and [S II]λ6731. The average error on individual emission-line velocities due to centroiding accuracy was roughly 1.5 km s^{-1}. We used the arithmetic mean of the measured emission-line velocities in each fiber as the fiber velocity. The maximum difference between the measured velocities and the mean was taken to be the error on the fiber velocity. Many of these errors were less than 5 km s^{-1}, though a few were as high as $\sim$ 20 km s^{-1}. If only Hα was observed in a fiber, the observed Hα velocity was taken as the fiber velocity and the error was set to 10 km s^{-1}.

The observed velocity fields were made by combining the individual DensePak pointings using the input shifts at the telescope. To confirm the accuracy of the offsets, an Hα flux image of the galaxy constructed from the DensePak observations was compared to an actual Hα image. Relative positions between features in the galaxy (i.e., bright HII regions) in the two images were measured and compared. The fluxes in any overlapping fibers were also compared. The accuracy of the fiber positions is $\sim 0''.6$, and we found the telescope to be capable of accurately shifting from the nearby bright offset stars (typically $1'$ - $2'$ shifts), as well as the smaller distances ($\sim 0''.7$ shifts) required to observe the spaces

between the DensePak fibers. The telescope pointing is robust and repeatable.

We used the NEMO (Teuben 1995) program ROTCUR (Begeman 1989) to derive rotation curves from our two-dimensional data. ROTCUR treats the observed velocity field as an ensemble of tilted rings and then fits for the center, systemic velocity, inclination, position angle, and rotation velocity in each ring. Specifically, ROTCUR does a nonlinear least-squares fit to the following equation:

$$V(x,y) = V_{sys} + V_{rot} \cos\theta \sin i, \tag{2.1}$$

where

$$\cos\theta = \frac{-(x-x_0)\sin(PA) + (y-y_0)\cos(PA)}{r} \tag{2.2}$$

and

$$r^2 = (x-x_0)^2 + (y-y_0)^2/\cos^2 i. \tag{2.3}$$

The observed velocity at position x,y, $V(x,y)$, is a function of the systemic velocity (V_{sys}), the rotation velocity (V_{rot}), the inclination (i), the position of the center of rotation (x_0,y_0), and the position angle (PA) of the major axis. The position angle is defined as the angle between north and the receding side of the major axis, measured from north through east. Each point is weighted by the inverse square of the error on the fiber velocity times $\cos(\theta)$, the angle away from the major axis.

The DensePak data cover the centers of the galaxies. We find these to be in the regime of solid-body rotation. Consequently, neither the center nor the inclination could be determined by the observations. The center was therefore fixed to the position of the optical center, and the inclination was fixed to published values (BMR01; BB02; Tully 1988). The systemic velocities were determined by ROTCUR. We also used ROTCUR to

determine the position angle of the major axis, using published long-slit values as the initial guess. If the position angle could not be well constrained by ROTCUR, then it was fixed to the long-slit value. The long-slit position angles are generally from either the HI velocity field or the surface photometry, or in some cases, are the position angles indicated in a catalog such as the UGC (Nilson 1973). Only two galaxies, UGC 477 and UGC 1281, had position angles well constrained by ROTCUR.

Ring radii were set to the effective fiber resolution for each galaxy. The resulting rotation curve was inspected for rings with considerably higher or lower velocities than neighboring rings. These highly deviant points in the rotation curve were investigated and were usually attributable to a single fiber in the ring having an extreme velocity. These extreme fibers were removed, and the rotation curve was recalculated. Finally, we added in quadrature to the error bars on the final rotation curve the velocity error from centroiding accuracy, corrected for inclination. We did not impose a minimum error on the rotation curve points, as was the case in some previous works (e.g., 5 km s^{-1} in Swaters et al. (2003a) and 4 km s^{-1} in BMR01). The nature of the errors on the rotation curve points from the velocity fields is different from that of the errors on long-slit rotation curves. In the long-slit case, the error is on a single velocity measurement and gives the accuracy with which a Gaussian could be fitted to an emission-line profile, or the error is given by the consistency of the observed emission lines (Hα, [N II]λ6584, [S II]λ6717 and [S II]λ6731). The error does not contain information about the uncertainty in the rotation velocity. Errors can become arbitrarily small in high signal-to-noise ratio data, and this is why minimum errors were imposed. In two-dimensional data, the rotation velocity is obtained from a tilted-ring fit. The error indicates something about the spread

of the velocities in a ring. In this case, a smaller error indicates that the gas in the ring has smaller noncircular motions.

2.5 Results for Individual Galaxies

In this section, we present the DensePak fiber positions, observed velocity fields, and rotation curves in Figures 2.1-2.11. A description is given for each galaxy, and we compare the rotation curves to previous raw long-slit Hα rotation curves, as well as HI rotation curves when available. Properties of the galaxies for which rotation curves are derived are listed in Table 2.1; there were 17 observed galaxies for which meaningful velocity fields could not be constructed.[3] As a result of remarkably poor weather, a number of galaxies have lopsided DensePak coverage.

UGC 4325– This galaxy is large on the sky, and four DensePak pointings were made on the approaching side. The positions are shown on the Hα image from van Zee (2000). The fiber velocities were the average of the Hα and [S II]λ6717 lines. Hα is prevalent and was detected in almost every fiber. The position angle was fixed at the average of the position angles of previous long-slit observations (BB02; Swaters et al. 2003a). There is excellent agreement between the DensePak rotation curve and the long-slit Hα rotation curve of BB02. Very similar results have also been obtained with SparsePak (Swaters 2005, private communication). The HI data (Swaters 1999) lie above the optical data at the inner radii. This suggests that the HI data have been over-corrected for beam

[3]CamB, F750-4, KK98 251, UGC 891, UHC 1501/NGC 784, UGC 2455/NGC 1156, UGC 2864, UGC 4543, UGC 4787, UGC 5414/NGC 3104, UGC 7603/NGC 4455, UGC 8837/DDO 185, UGC 9211/DDO 189, UGC 11583, UGC 12344, UGC 12713, and UGC 12791.

Table 2.1. Properties of Observed Galaxies

Galaxy (1)	R.A. (J2000.0) (2)	Decl. (J2000.0) (3)	μ_0(R) (mag arcsec^{-2}) (4)	Distance (Mpc) (5)	i (deg) (6)	V_{hel} (km s^{-1}) (7)	R_{max} (kpc) (8)	V_{max} (km s^{-1}) (9)	P.A. (deg) (10)	References (11)
UGC 4325	08 19 20.5	+50 00 35	21.6	10.1	41	514	2.3	86	52	2
F563-V2	08 53 03.7	+18 26 09	21.2[a]	61	29	4316	6.7	104	328	1
F563-1	08 55 06.9	+19 44 58	22.6	45	25	3482	5.6	146	341	1
DDO 64[b]	09 50 22.4	+31 29 16	-	6.1	60	520	2.1	51	97	2
F568-3	10 27 20.3	+22 14 22	22.2[a]	77	40	5905	8.4	114	169	1
UGC 5750	10 35 45.1	+20 59 24	22.6	56	64	4160	8.5	61	167	2
NGC 4395[c]	12 25 48.9	+33 32 48	22.2	3.5	46	310	0.8	33	327	2
F583-4	15 52 12.7	+18 47 06	22.9[a]	49	55	3620	7.5	75	115	1
F583-1	15 57 27.5	+20 39 58	23.2[a]	32	63	2256	4.9	83	355	1
UGC 477	00 46 13.1	+19 29 24	-	35	82	2635	10	112	347	3
UGC 1281	01 49 32.0	+32 35 23	22.7[d]	5.5	85	145	1.9	38	218	3

Note. — Units of right ascension are hours, minutes, and seconds, units of declination are degrees, arcminutes, and arcseconds. Col.(1): Galaxy name. Col.(2): Right Ascension. Col.(3): Declination. Col.(4): Central surface brightness in *R*-band. Col.(5): Distance. Col.(6): Inclination. Col.(7): Heliocentric systemic velocity. Col.(8): Maximum radius of the DensePak rotation curve. Col.(9): Maximum velocity of the DensePak rotation curve. Col.(10): Position angle of major axis; see §2.5 for details. Col.(11): References for surface brightness, distance, and inclination.

[a] Converted from *B* band assuming $B - R = 0.9$.

[b] DDO 64 = UGC 5272.

[c] NGC 4395 = UGC 7524.

[d] Taken from BB02.

REFERENCES — (1) BB02; (2) BMR01; (3) Tully 1988.

smearing (BB02). The outer HI points are a bit lower than the optical data but are within 1σ. The decline in the rotation curve at the outer radii may be a real feature (Bosma 2004).

F563-V2– There was one pointing for this galaxy. The DensePak fibers are shown on the Hα image from McGaugh, Schombert, & Bothun (1995). The fiber velocities were the average of the Hα, [S II]λ6717, and [S II]λ6731 lines. There is little Hα emission, and only roughly half of the fibers have an Hα detection. The position angle was fixed to the value used in Swaters et al. (2003a). The DensePak rotation curve generally agrees with the HI rotation curve of BMH96.

F563-1– There was one pointing for this galaxy. The fiber positions are shown on an Hα image (W.J.G. de Blok 2005, unpublished data). The fiber velocities were the average of the Hα, [S II]λ6717, and [S II]λ6731 lines. The fibers were offset toward the receding side of the galaxy, and there was very little emission in the fibers on the approaching side. The position angle was fixed to the value in MRB01 and BB02. When compared to the long-slit Hα rotation curves of BMR01 and BB02, there is good agreement up to $15''$. Beyond that, however, the long-slit curves and the HI curve (BMH96) turn over and flatten out, while the DensePak curve continues to rise. Additional DensePak coverage would be useful in determining where the DensePak curve turns over.

DDO 64– There were three pointings for the center and approaching side of this galaxy. The DensePak fiber positions are shown on a Digitized Sky Survey [4] image. Fiber

[4]The Digitized Sky Surveys were produced at the Space Telescope Science Institute under NASA grant NAG W-2166. The images of these surveys are based on photographic data obtained using the Oschin Schmidt Telescope on Palomar Mountain and the UK Schmidt Telescope. The plates were processed into

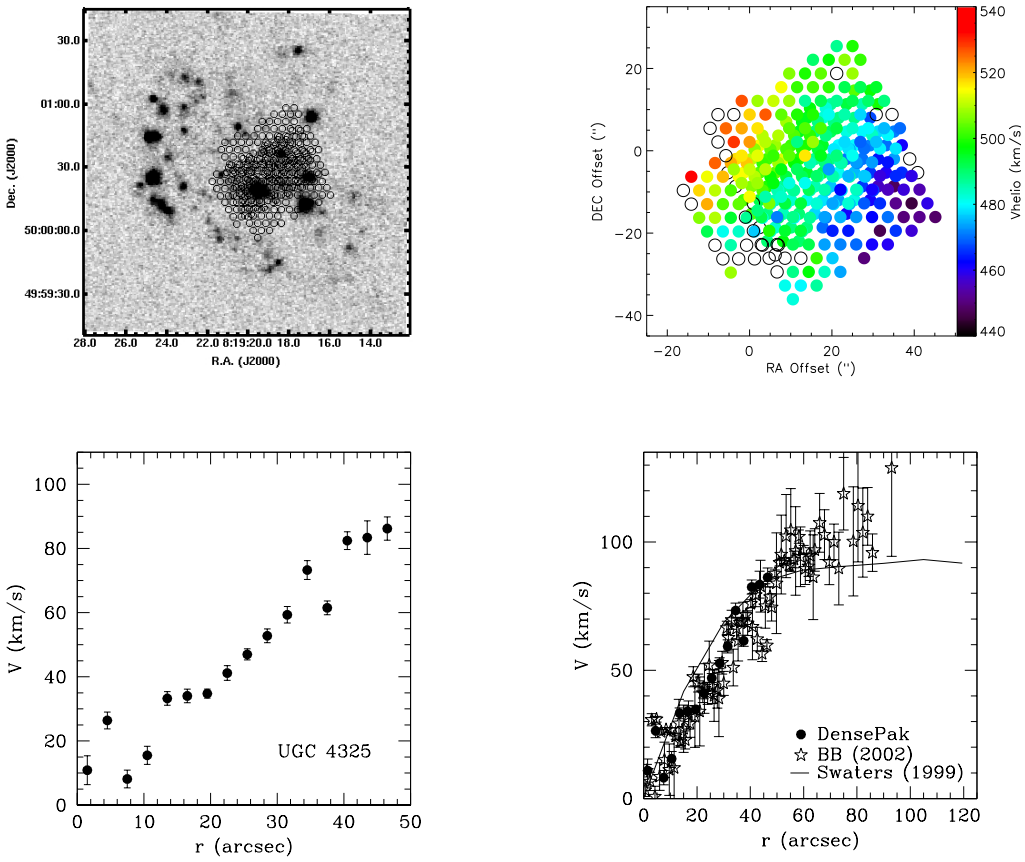

Figure 2.1: – Results for UGC 4325. *Top left:* Position of DensePak array on the Hα image of the galaxy. This is an example of where interstitial pointings have been made to fill in the gaps between the fibers. *Top right:* Observed DensePak velocity field. Empty fibers are those without detections. *Bottom left:* DensePak rotation curve. *Bottom right:* DensePak rotation curve plotted with the raw long-slit Hα rotation curve of de Blok & Bosma (2002) and the HI rotation curve of Swaters (1999). The HI data was excluded from the halo fits.

velocities were the average of the Hα and [S II]λ6717 lines. The amount of emission in this galaxy is very high, and nearly all fibers detected emission. The position angle was fixed to the BB02 value. The DensePak points rise and fall in a pattern similar to the long-slit data (BB02). The structure in the rotation curve appears to be real. That the inner two

the present compressed digital form with the permission of these institutions.

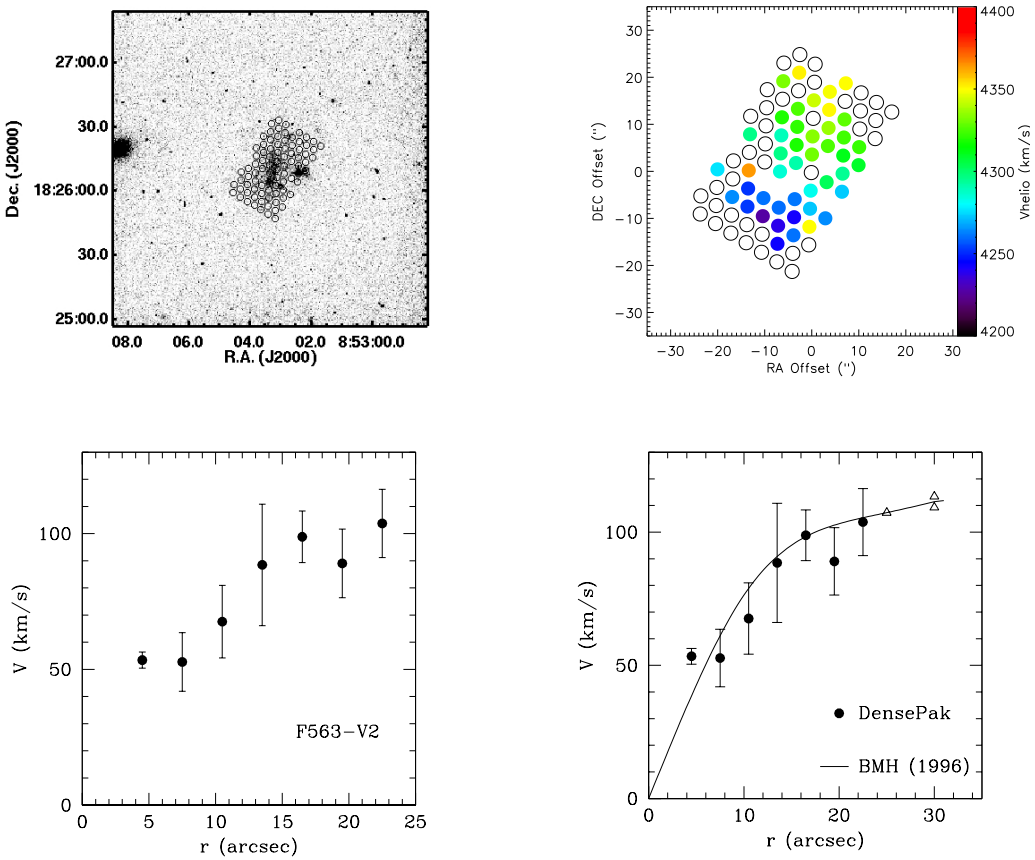

Figure 2.2: – Results for F563-V2. *Top left:* Position of DensePak array on an Hα image of the galaxy. *Top right:* Observed DensePak velocity field. Empty fibers are those without detections. *Bottom left:* DensePak rotation curve. *Bottom right:* DensePak rotation curve plotted with the HI rotation curve of de Blok, McGaugh, & van der Hulst (1996). Triangles represent the HI points used in the halo fits.

points fall below the long-slit data may suggest the presence of noncircular motions in the inner regions. The HI data (Stil 1999) lies slightly below, but within the errors of, the optical data. It should be noted, however, that over the radial range plotted in Figure 2.4 there are only two HI points.

F568-3– There was one pointing for this galaxy, and the fiber positions are shown on an Hα image (W.J.G. de Blok 2005, unpublished data). The fiber velocities were the

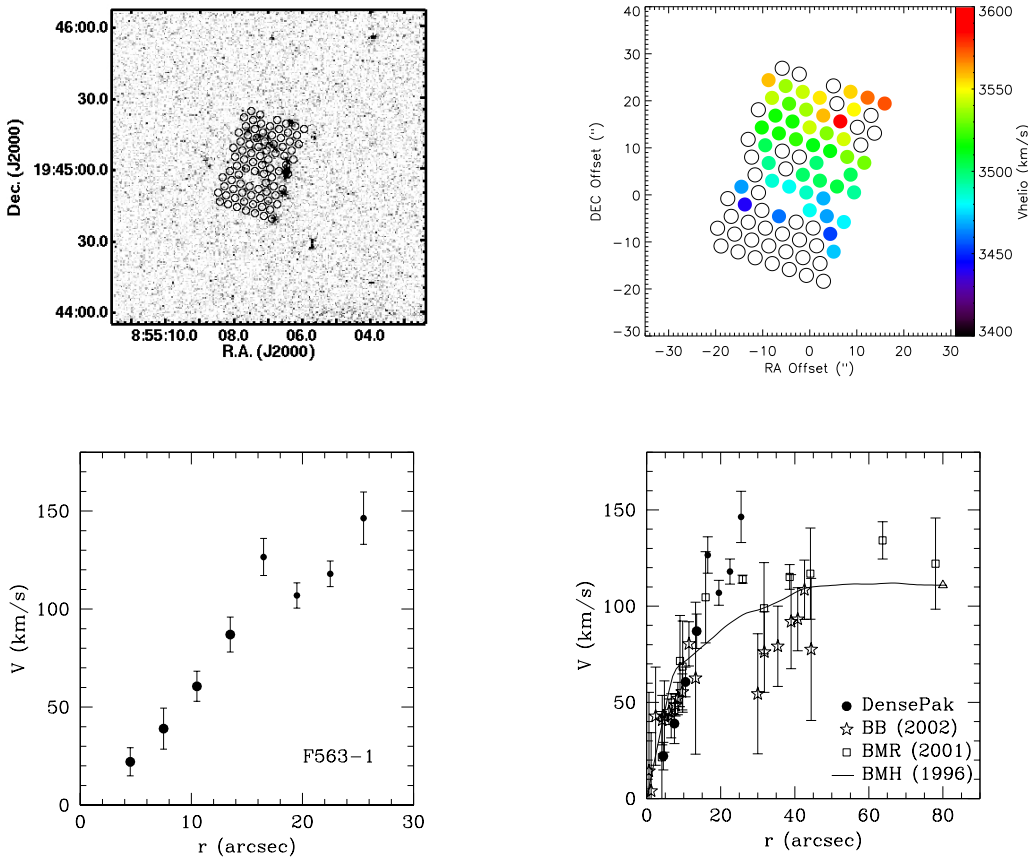

Figure 2.3: – Results for F563-1. *Top left:* Position of DensePak array on an Hα image of the galaxy. *Top right:* Observed DensePak velocity field. Empty fibers are those without detections. *Bottom left:* DensePak rotation curve. The last four points are omitted from the halo fits. *Bottom right:* DensePak rotation curve plotted with the raw long-slit Hα rotation curves of de Blok & Bosma (2002) and de Blok, McGaugh, & Rubin (2001) and the HI rotation curve of de Blok, McGaugh, & van der Hulst (1996). The triangle represents the HI point used in the halo fits.

average of the Hα and the [N II]λ6584 lines. Hα emission was detected in roughly 60% of the fibers. The position angle was fixed to the MRB01 and Swaters et al. (2003a) long-slit value. The DensePak rotation curve is consistent with the long-slit Hα curve of BMR01 and the HI curve of BMH96.

UGC 5750– There was one pointing for this galaxy. The fiber positions are shown

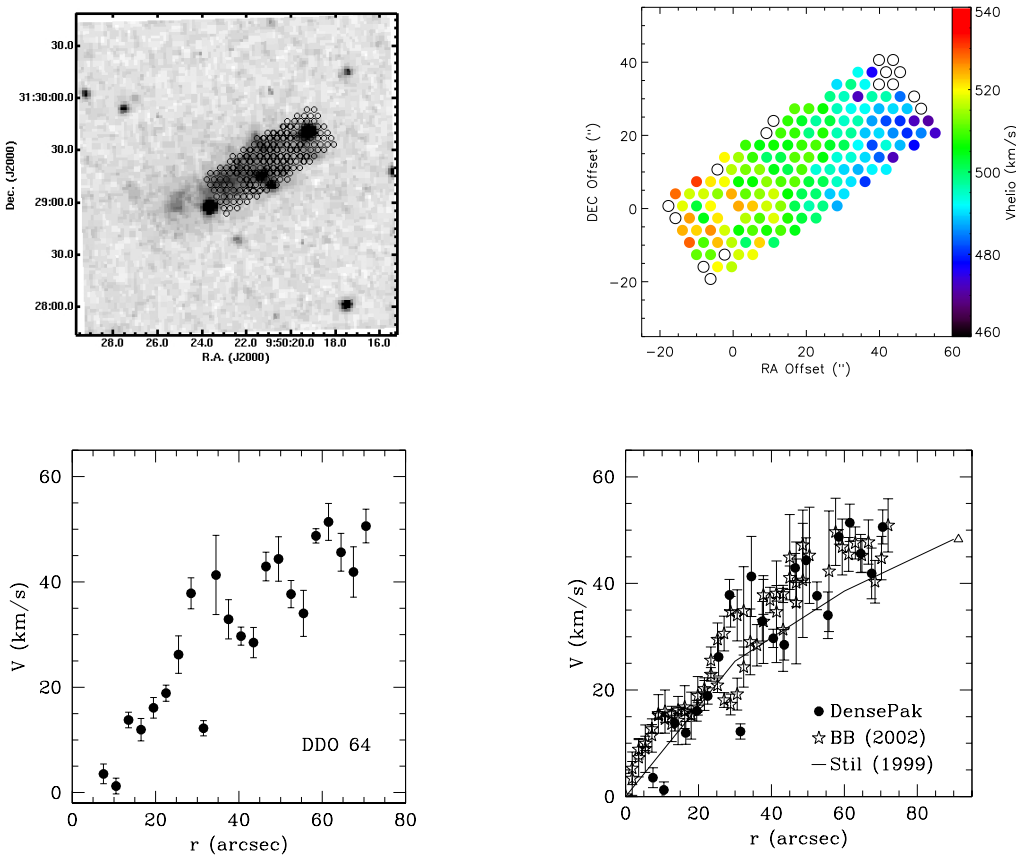

Figure 2.4: – Results for DDO 64. *Top left:* Position of DensePak array on a Digitized Sky Survey image of the galaxy. *Top right:* Observed DensePak velocity field. The empty fibers are those without detections. *Bottom left:* DensePak rotation curve. *Bottom right:* DensePak rotation curve plotted with the raw long-slit Hα rotation curve of de Blok & Bosma (2002) and the HI rotation curve of Stil (1999). The triangle represents the HI point used in the halo fits.

on an Hα image (W.J.G. de Blok 2005, unpublished data). The average of the Hα, [N II]λ6584, [S II]λ6717, and [S II]λ6731 lines was taken as the fiber velocity. Hα emission was sparse in this galaxy, and only roughly half of the fibers had a detection. The position angle was fixed to the value listed in MRB01 and BB02. There is good agreement with the long-slit Hα rotation curves of both BB02 and BMR01.

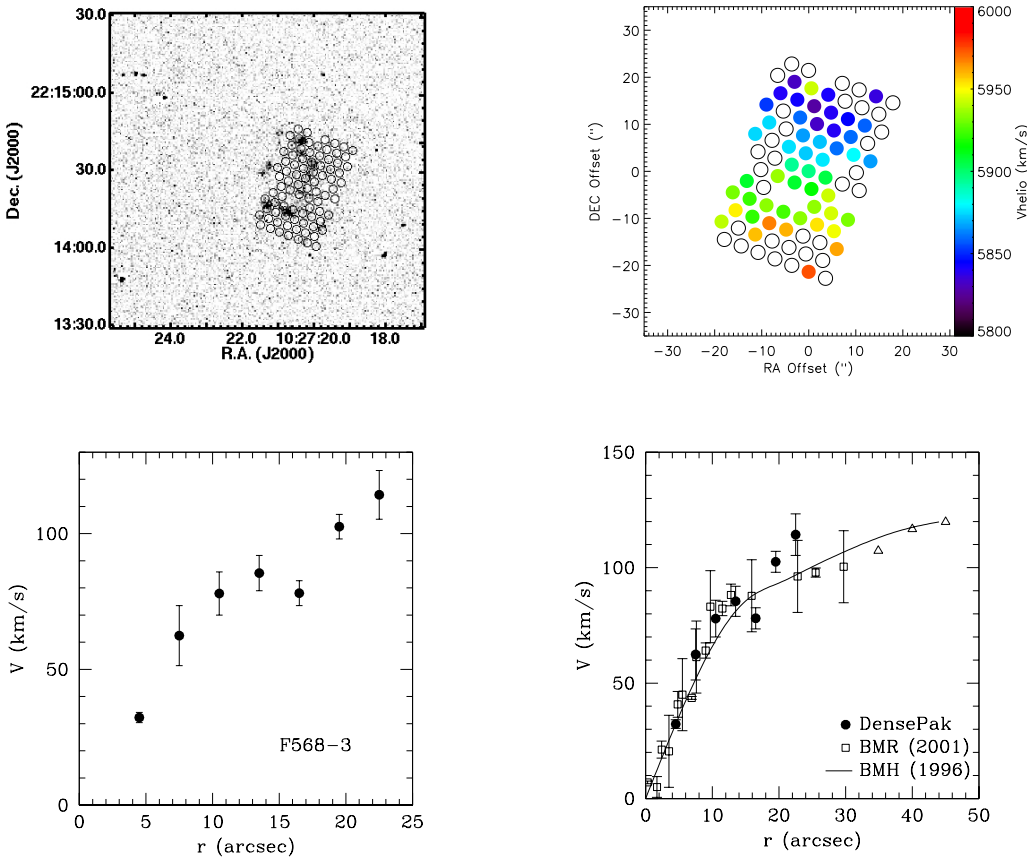

Figure 2.5: – Results for F568-3. *Top left:* Position of DensePak array on an Hα image of the galaxy. *Top right:* Observed DensePak velocity field. The empty fibers are those without detections. *Bottom left:* DensePak rotation curve. *Bottom right:* DensePak rotation curve plotted with the raw long-slit Hα rotation curve of de Blok, McGaugh, & Rubin (2001) and the HI rotation curve of de Blok, McGaugh, & van der Hulst (1996). Triangles represent the HI points used in the halo fits.

NGC 4395– There were five pointings for this galaxy, and the positions of the DensePak fibers are shown on an *R*-band image (W.J.G. de Blok 2005, unpublished data). The Hα line overlapped slightly with a sky line. This was not a serious problem for this galaxy, because the emission lines (particularly the Hα line) were very strong. The Hα line was measured in a fiber if the [N II]λ6584, [S II]λ6717, and [S II]λ6731 lines were visible and strong and if the Hα line was stronger than the neighboring sky lines.

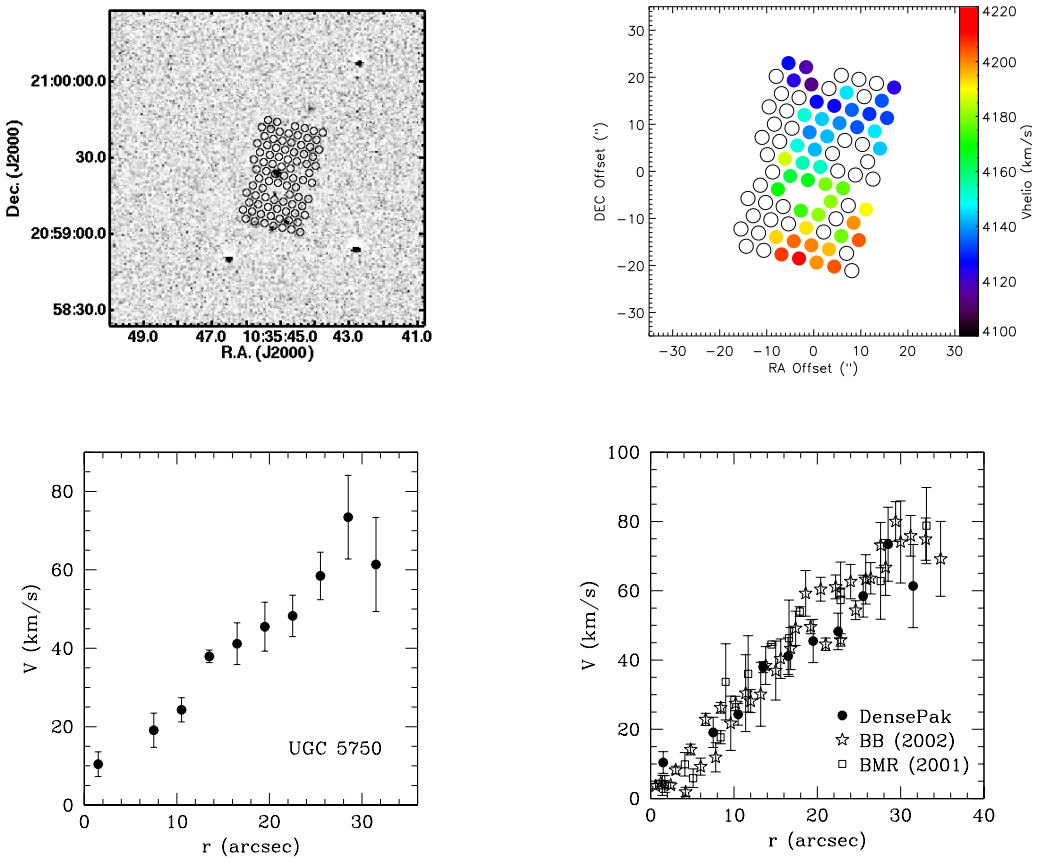

Figure 2.6: – Results for UGC 5750. *Top left:* Position of DensePak array on an Hα image of the galaxy. *Top right:* Observed DensePak velocity field. Empty fibers are those without detections. *Bottom left:* DensePak rotation curve. *Bottom right:* DensePak rotation curve plotted with the raw long-slit Hα rotation curves of de Blok & Bosma (2002) and de Blok, McGaugh, & Rubin (2001).

With these criteria, Hα was detected in nearly all the fibers. The fiber velocities were the average of the Hα and [S II]λ6717 lines. The position angle of BB02 was used as the DensePak position angle. The DensePak rotation curve is consistent with the long-slit Hα curve of BB02, as well as the HI curve (Swaters 1999) at the innermost radii. At the outer radii, the HI curve falls below the optical data at about the 2σ level.

F583-4– There were two pointings for this galaxy: a central pointing and an in-

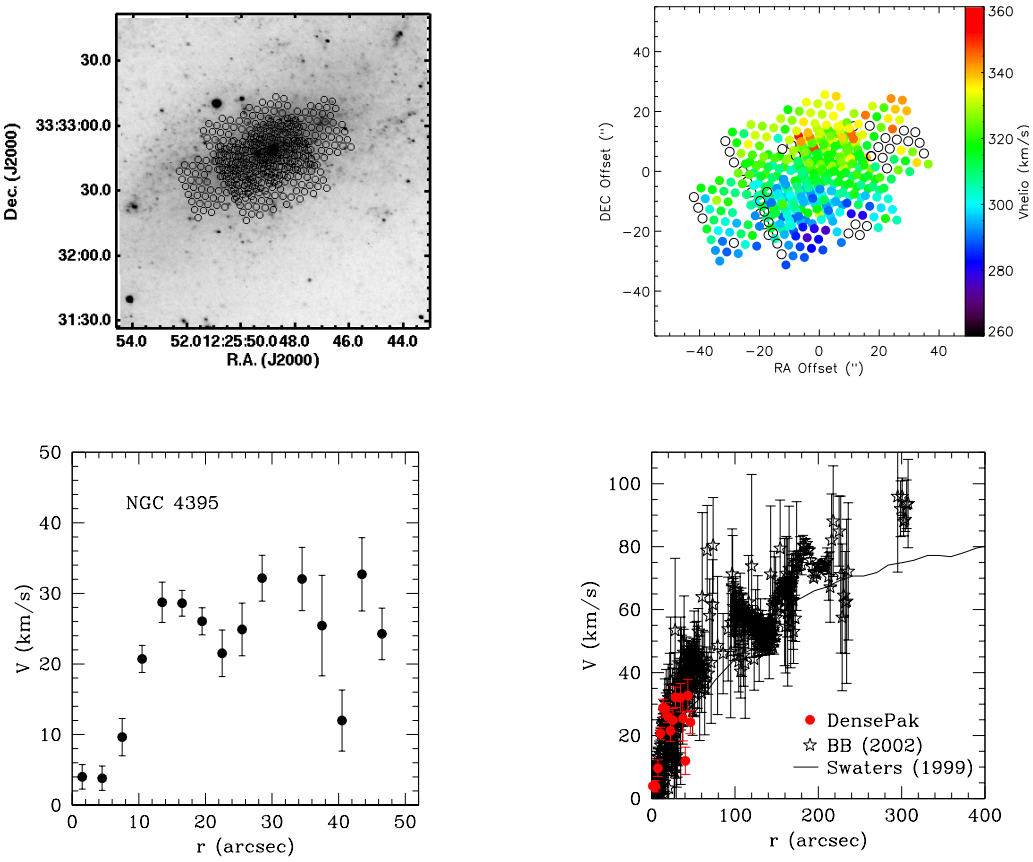

Figure 2.7: – Results for NGC 4395. *Top left:* Position of DensePak array on an *R*-band image of the galaxy. *Top right:* Observed DensePak velocity field. Empty fibers are those without detections. *Bottom left:* DensePak rotation curve. *(Lower right)* DensePak rotation curve plotted with the raw long-slit Hα rotation curve of de Blok & Bosma (2002) and the HI rotation curve of Swaters (1999). The HI points used in the halo fits extend beyond the radial range of this plot.

terstitial pointing; the fiber positions are shown on the *R*-band image from BMH96. The fiber velocities are the averages of the Hα, [S II]λ6717, and [S II]λ6731 lines, and the approaching side of the galaxy has slightly better coverage than the receding side. The position angle was fixed to the value in MRB01. The DensePak rotation curve is generally consistent with the long-slit Hα rotation curve of BMR01. Both optical rotation curves are offset to noticeably higher velocities than the HI rotation curve of BMH96. This is

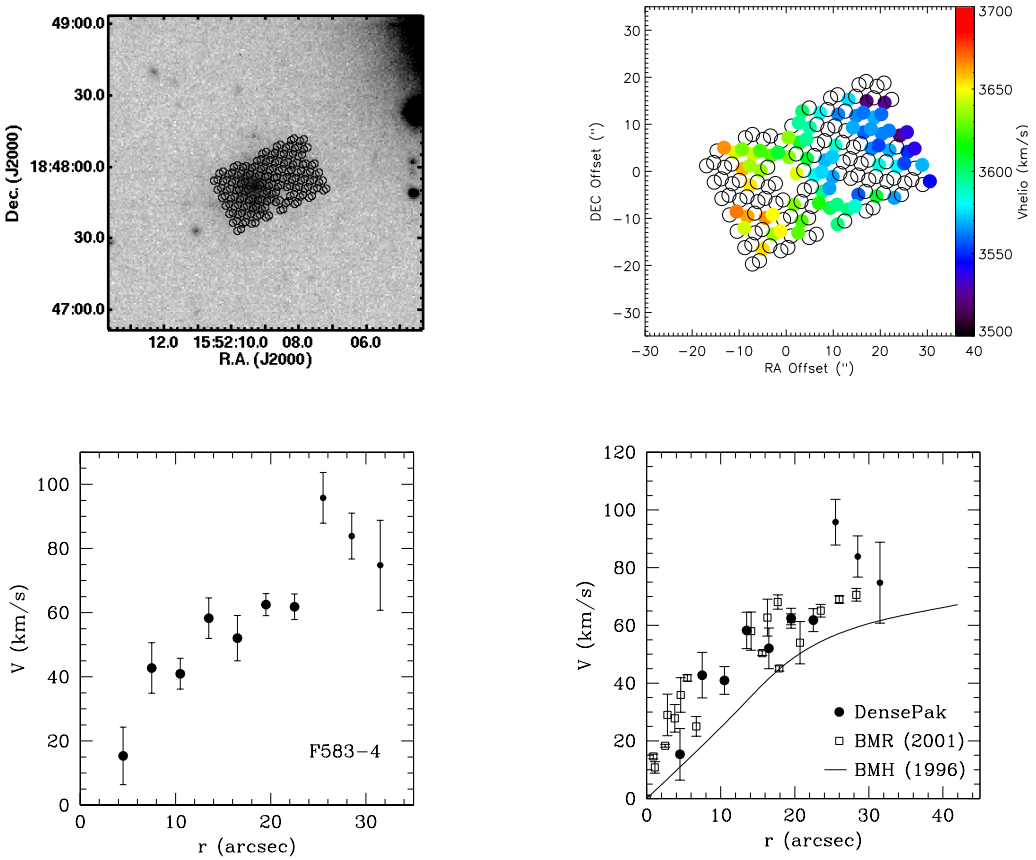

Figure 2.8: – Results for F583-4. *Top left:* Position of DensePak array on an *R*-band image of the galaxy. *Top right:* Observed DensePak velocity field. Empty fibers are those without detections. *Bottom left:* DensePak rotation curve. The last three points were excluded from the halo fits. *Bottom right:* DensePak rotation curve plotted with the raw long-slit Hα rotation curve of de Blok, McGaugh, & Rubin (2001) and the HI rotation curve of de Blok, McGaugh, & van der Hulst (1996). The HI data were not included in the halo fits.

one of the few galaxies where beam smearing in the HI data turned out to be important (BMR01).

F583-1– There is one pointing for this galaxy. The DensePak fibers are shown on the *R*-band image of the galaxy from BMH96. The fiber velocities are the averages of the Hα, [S II]λ6717, and [S II]λ6731 lines, and more of the approaching side of the galaxy

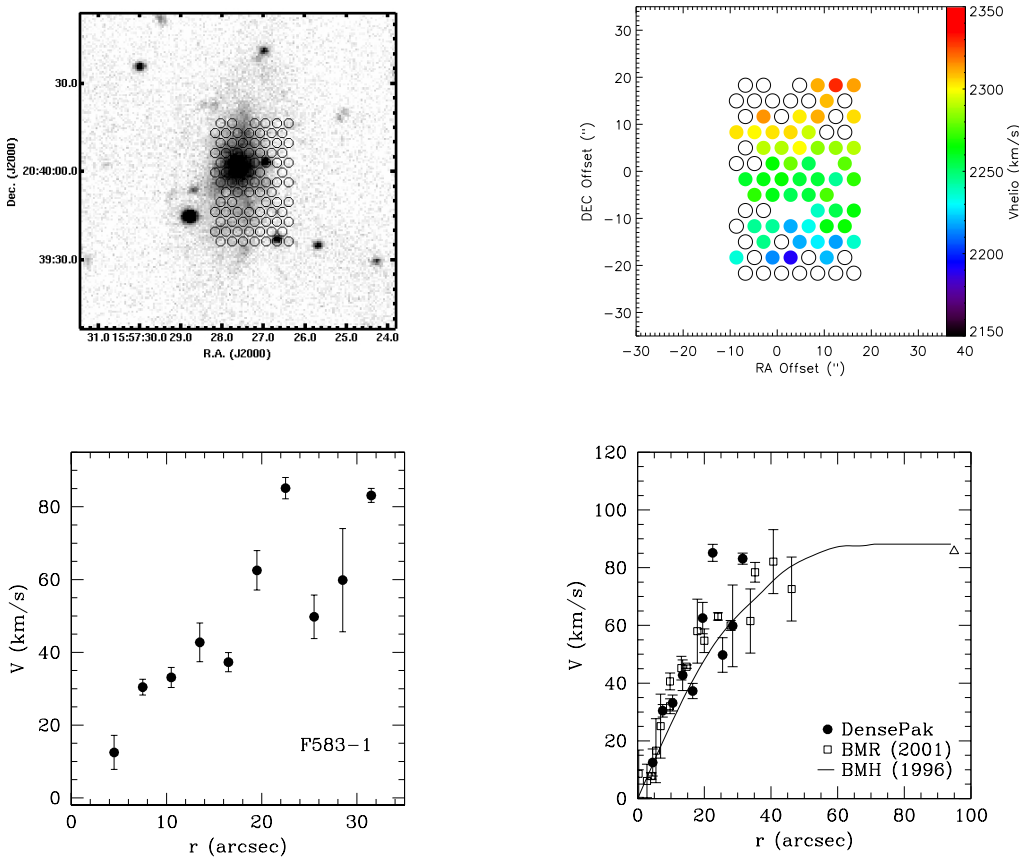

Figure 2.9: – Results for F583-1. *Top left:* Position of DensePak array on a *R*-band image of the galaxy. *Top right:* Observed DensePak velocity field. Empty fibers are those without detections. *Bottom left:* DensePak rotation curve. *Bottom right:* DensePak rotation curve plotted with the raw long-slit Hα rotation curve of de Blok, McGaugh, & Rubin (2001) and the HI rotation curve of de Blok, McGaugh, & van der Hulst (1996). The triangle represents the HI point used in the halo fits.

is seen than the receding side. The MRB01 position angle was taken as the DensePak position angle. The DensePak rotation curve is consistent with both the long-slit Hα rotation curve of BMR01 and the HI rotation curve of BMH96.

UGC 477– There were three interstitial pointings along the length of this galaxy, and spatial coverage of the galaxy was optimal. The DensePak fibers are shown on the *R*-band image obtained at the KPNO 2 m telescope. Fiber velocities were the average of

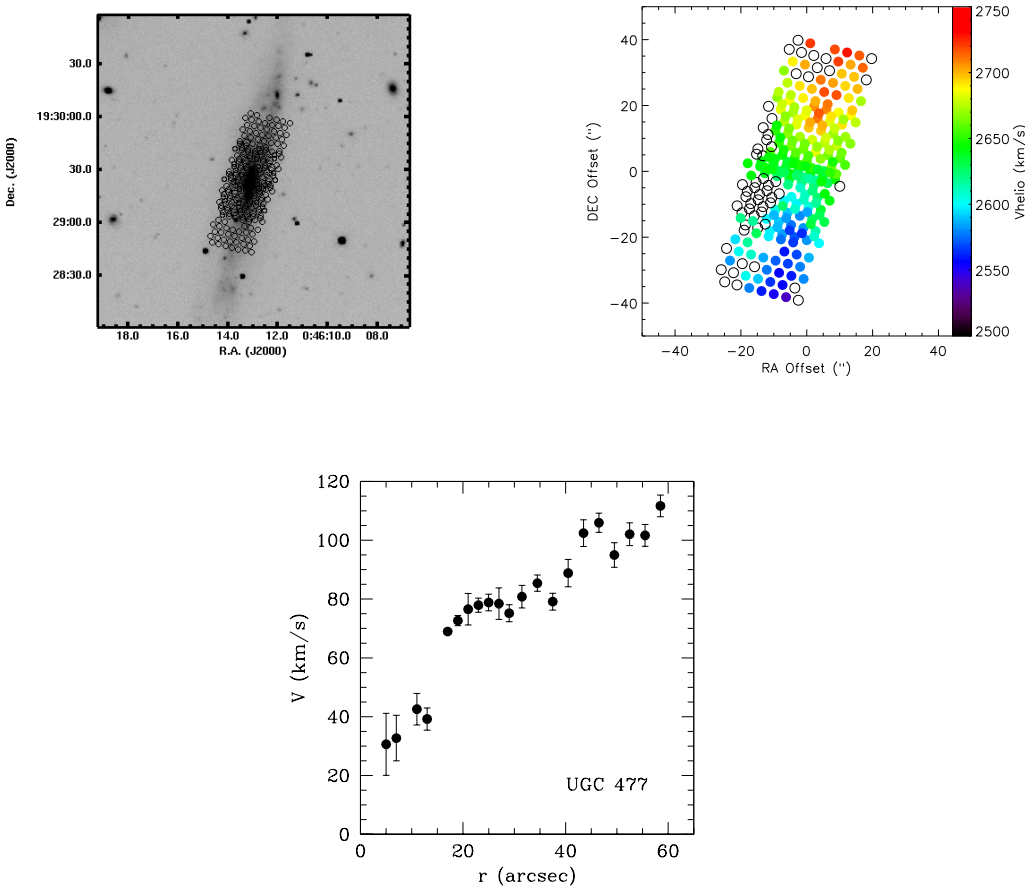

Figure 2.10: – Results for UGC 477. *Top left:* Position of DensePak array on a *R*-band image of the galaxy. *Top right:* Observed DensePak velocity field. Empty fibers are those without detections. *Bottom:* DensePak rotation curve.

the Hα, [N II]λ6584, [S II]λ6717, and [S II]λ6731 lines. The amount of emission was very high in this galaxy, and almost every fiber had a detection. The position angle was well constrained by the data.

UGC 1281– There were five interstitial pointings for this galaxy. The amount of emission was sparse, as fewer than 50% of the fibers had a detection. The DensePak fibers are shown on the *R*-band image obtained at the KPNO 2 m telescope. Fiber veloc-

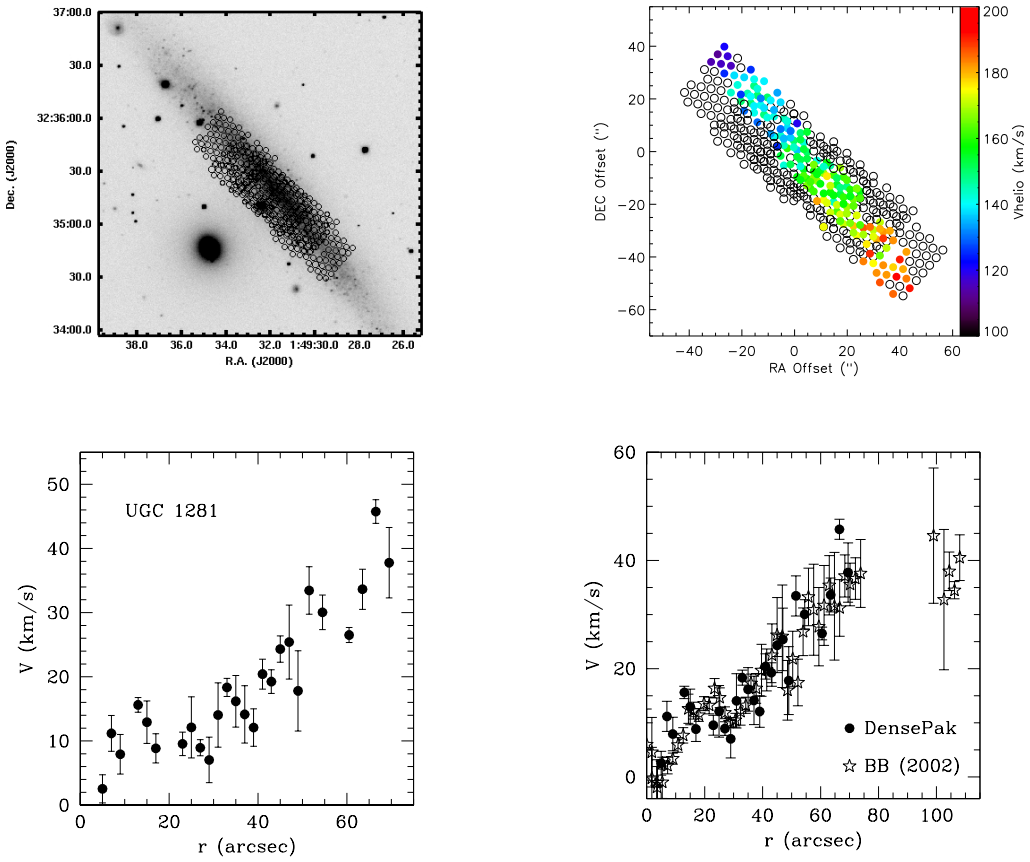

Figure 2.11: – Results for UGC 1281. *Top left:* Position of DensePak array on a *R*-band image of the galaxy. *Top right:* Observed DensePak velocity field. Empty fibers are those without detections. *Bottom left:* DensePak rotation curve. *Bottom right:* DensePak rotation curve plotted with the raw long-slit Hα rotation curve of de Blok & Bosma (2002).

ities were the average of the Hα, [S II]λ6717, and [S II]λ6731 lines. The position angle was well constrained by the data, and the DensePak rotation curve is consistent with the long-slit Hα rotation curve of BB02. UGC 1281 is a nearly edge-on galaxy. At high inclination, line-of-sight integration effects become important and may cause an intrinsically steeply rising rotation curve to appear slowly rising. The shape of the emission-line profiles can be used to constrain the shape of the rotation curve. If instrumental resolu-

tion is high enough and there is no line-of-sight obscuration, then symmetric line profiles indicate a solid-body rotation curve and skewed line profiles indicate a curved, NFW-like rotation curve (Kregel, van der Kruit, & Freeman 2004). The line profiles in the DensePak fibers are symmetric. UGC 1281 is unlikely to be so optically thick that the observations are hampered by obscuration (de Naray, McGaugh, & de Blok 2004). Our instrumental resolution, however, is probably not high enough to resolve any skewing that may be present. We present the minimum-disk case analysis for this galaxy in § 2.6.2 but exclude it from further modeling.

Obtaining high-quality velocity fields is not trivial. LSB galaxies are difficult to observe. The Hα emission is faint. In addition, the emission may not be spread out enough to be detected across the entire DensePak fiber array. Although we tried to select galaxies with promising Hα emission, the remaining 17 galaxies of our sample[5] were observed, but unfortunately the detections were not good enough to construct meaningful velocity fields.

For the 11 galaxies for which we have constructed velocity fields, there is good overall agreement between the new DensePak rotation curves and the previous data sets. In all cases, the data are broadly consistent with previous long-slit rotation curves. In only two cases, F563-1 and F583-4, do these independent data seem to differ, and then only over a very limited range in radius. In cases where HI data are available, five are in good overall agreement. In two cases, DDO 64 and F583-4, the HI data are somewhat lower than the optical data. In one case, UGC 4325, the HI data are too high. It is tempting to blame these cases on beam smearing or, in the case of UGC 4325, overcorrection for beam

[5]For a list of these galaxies, see footnote 3 in §2.5

smearing, although other factors, such as the intrinsic HI distribution, are also relevant. On the whole, we are encouraged by the extent to which various independent data sets agree, given the difficult observational challenge posed by LSB galaxies.

2.6 Preliminary Analysis and Discussion

In this section, we wish to give an impression of how well the data are described by various halo models. We limit this discussion to the minimum-disk case in which we ignore the contribution of the stars and gas and attribute all rotation to dark matter. This puts an upper limit on the slope and/or concentration of the halo density profile. More detailed analysis, including mass modeling, will be presented in a future paper.

2.6.1 Halo Models

Two of the most prominent competing dark matter halo density profiles are the pseudoisothermal halo and the NFW profile. We provide a brief description of each below.

2.6.1.1 Pseudoisothermal Halo

The density profile of the pseudoisothermal halo is

$$\rho_{iso}(R) = \rho_0[1 + (R/R_C)^2]^{-1}, \tag{2.4}$$

with ρ_0 being the central density of the halo and R_C representing the core radius of the halo. The rotation curve corresponding to this density profile is

$$V(R) = \sqrt{4\pi G\rho_0 R_C^2 \left[1 - \frac{R_C}{R}\arctan\left(\frac{R}{R_C}\right)\right]}. \tag{2.5}$$

This form has traditionally been used in rotation curve fitting because it works well. By construction it produces flat rotation curves at large radii. This halo form is empirically motivated, predating those stemming from simulations.

2.6.1.2 NFW Profile

Numerical simulations produce the NFW profile and its variants. It predicts the same functional behavior for CDM halos of galaxy clusters as for the CDM halo of a single galaxy. The NFW mass density distribution is described as

$$\rho_{NFW}(R) = \frac{\rho_i}{(R/R_s)(1+R/R_s)^2}, \tag{2.6}$$

in which ρ_i is related to the density of the universe at the time of halo collapse and R_s is the characteristic radius of the halo. The NFW rotation curve is given by

$$V(R) = V_{200}\sqrt{\frac{\ln(1+cx) - cx/(1+cx)}{x[\ln(1+c) - c/(1+c)]}}, \tag{2.7}$$

with $x = R/R_{200}$. The rotation curve is parameterized by a radius R_{200} and a concentration parameter $c = R_{200}/R_s$, both of which are directly related to R_s and ρ_i. Here R_{200} is the radius at which the density contrast exceeds 200, roughly the virial radius; V_{200} is the circular velocity at R_{200} (Navarro, Frenk, & White 1996). As previously mentioned in §2.2, there are other cuspy halo models with slopes steeper than the NFW profile (e.g., Moore et al. 1999b; Reed et al. 2003; Navarro et al. 2004; Diemand et al. 2005). The NFW profile thus serves as a lower limit to the slope of cuspy density profiles and, as such, gives the cuspy halo the best possible chance to fit the data. From an observational perspective, there is very little to distinguish the various flavors of cuspy halos.

2.6.2 Halo Fits to Combined Data

In this section, we combine the DensePak data with the previous smoothed long-slit Hα and HI rotation curves when available. For the 10 galaxies with long-slit and/or HI data, we supplement the DensePak data with the entire long-slit rotation curve and include only those HI points that extend beyond the radial range of both the DensePak and long-slit data. Using only the outer HI points, where the rotation curves have usually begun to flatten, lessens possible resolution effects. As discussed below, there are three galaxies, F563-1, F583-4, and UGC 4325, for which we exclude some of the DensePak and/or HI data.

We find the best-fit isothermal halo and NFW halo. This NFW halo fit is referred to as NFW_{free}. The NFW_{free} halo fits do not necessarily have parameters that are realistic or consistent with ΛCDM. There is a tendency for the fits to drive toward very low c and very high V_{200}. There is also a c-V_{200} degeneracy that allows halos of different c,V_{200} to look the same over a finite range of radius. It is common for the NFW_{free} halos to overshoot the data at small radii, then undershoot the data, and then overshoot the data again and provide a poor description of the data at large radii. To address this, we also make a fit which we refer to as $NFW_{constrained}$ (hereafter NFW_{constr}). This halo was required to match the velocities at the outer radii of each galaxy while constraining the concentration to agree with cosmology. We chose a value of V_{200} that forced the NFW velocities to match as many of the data points in the turnover region as closely as possible, with a minimum requirement of falling within the error bars. This is a reasonable constraint, because dark matter must explain the high velocities at large radii, where the contribution

of the baryons has fallen off. Equation (7) of de Blok, Bosma, & McGaugh (2003), which gives the concentration as a function of V_{200} (Navarro, Frenk, & White 1997), was then used to calculate the concentration. We adjusted this concentration to agree with the cosmology of Tegmark et al. (2004) by subtracting 0.011 dex (McGaugh, Barker, & de Blok 2003).

We did not include the last four DensePak points of F563-1 or the last three DensePak points of F583-4 in the halo fits. The F563-1 points were excluded because they are based on few fibers and because of the significant inconsistency with the long-slit and HI rotation curves, as discussed in § 2.5. The outer DensePak points of F583-4 spike to higher velocities than the long-slit data at the equivalent radii. Neither the isothermal nor the NFW halo model will be able to fit this feature in the DensePak rotation curve. These DensePak points also have little influence on the halo fits; there is essentially no change in the values of the isothermal or NFW halo parameters, but only much-improved χ^2, when the three DensePak points are removed. There are two and three HI points beyond the optical data for UGC 4325 and F583-4, respectively, that were also not used. Although the rise then sudden decline suggested by the combined optical and HI data for UGC 4325 may well be real, no simple, smooth model can fit it. Since we are interested in the inner halo structure as probed by the new data, we exclude the two HI points. For a thorough comparison of many more independent data for this galaxy see Bosma (2004). The situation is similar for the HI points of F583-4.

In Figure 2.12, we plot the halo fits over the data, and we list the parameters in Table 2.2. We plot $\log(V)$ against $\log(r)$ to emphasize the fits to the data at small radii. The NFW_{constr} halos have already been required to match the data at large radii, and

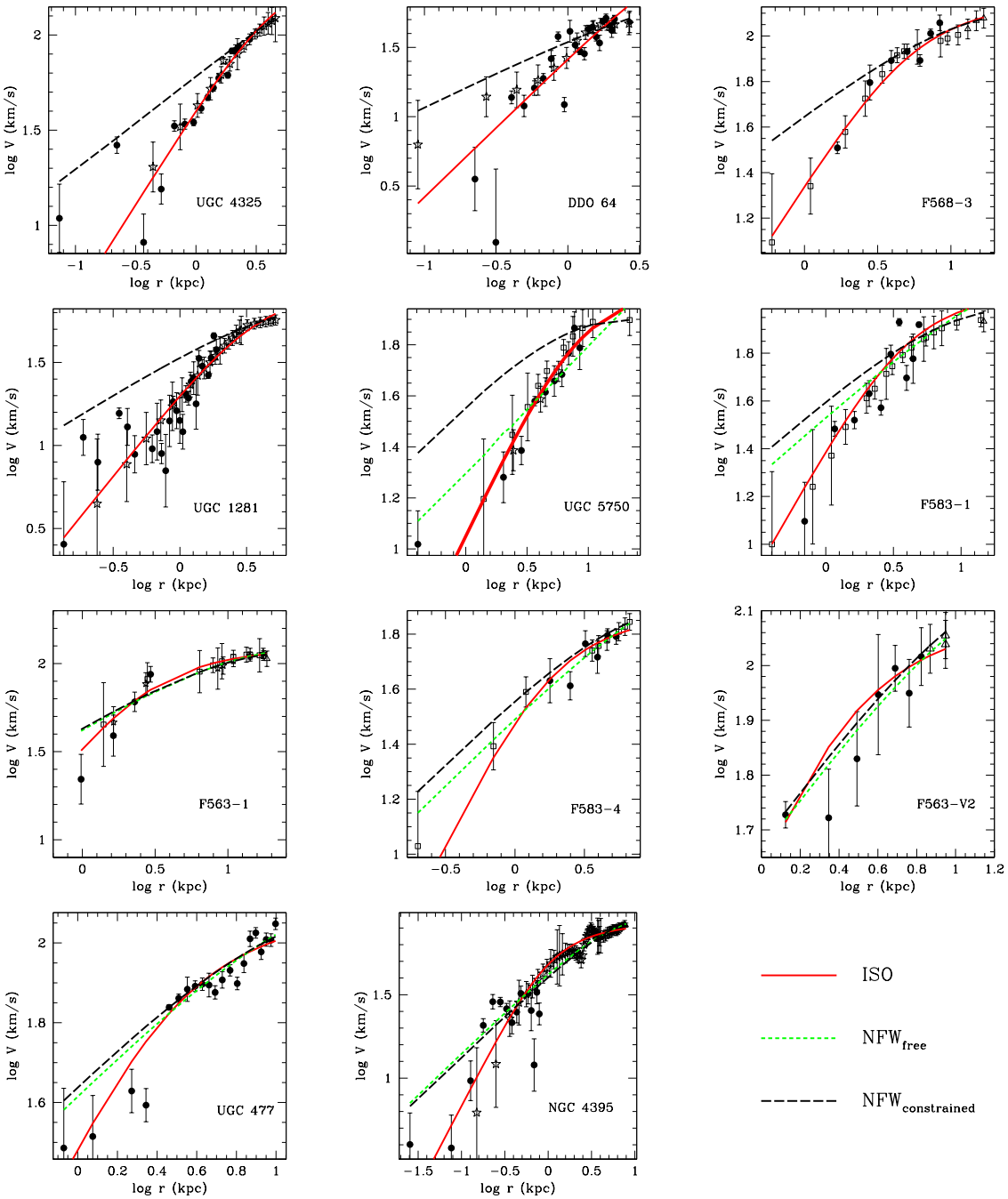

Figure 2.12: – Halo fits to the combined DensePak and smoothed long-slit and HI rotation curves. Symbols remain the same as in Figs. 2.1-2.11. The order of the galaxies has been changed from the order of Figs. 2.1-2.11 in order to show a progression in the halo fits. The fits change from isothermal to indistinguishable to NFW from top to bottom, left to right.

Table 2.2. Best-Fit Halo Parameters

	ISO			NFW_{free}			NFW_{constr}		
Galaxy	R_c (kpc)	ρ_0 ($10^{-3}M_\odot$ pc^{-3})	χ^2_r	c	V_{200} (km s^{-1})	χ^2_r	c	V_{200} (km s^{-1})	χ^2_r
UGC 4325	3.3±0.2	91±4	3.8	···	···	···	6.9	249	40
F563-V2	1.5±0.1	119±6	0.71	7.7±2.0	128±32	0.40	7.9	130	0.58
F563-1	2.1±0.1	67±2	0.43	7.8±1.3	106±10	0.88	8.4	101	0.95
DDO 64	4.4±0.9	38±3	5.5	···	···	···	9.2	62	20
F568-3	3.8±0.2	27±1	1.2	···	···	···	8.2	110	12
UGC 5750	5.7±0.4	7.1±0.3	0.83	0.5±0.1	320±43	1.7	9.1	67	25
NGC 4395	0.7±0.1	258±9	2.9	10.1±0.6	77±4	2.1	8.6	87	2.2
F583-4	1.3±0.1	67±2	0.67	5.5±2.2	92±32	0.41	9.1	67	1.1
F583-1	2.7±0.1	35±2	5.4	4.7±0.7	133±21	8.7	8.7	83	11
UGC 477	2.2±0.1	57±2	4.6	6.9±0.6	120±9	4.6	8.3	105	5.4
UGC 1281	2.6±0.1	23±1	3.8	···	···	···	9.3	58	25

Note. — Best-fit halo parameters for the combined DensePak, long-slit and HI rotation curves.

although the best-fit NFW_{free} halos do not necessarily match the velocities at large radii, the magnitude of the discrepancy is generally smaller than it is at small radii.

No NFW_{free} fit could be made to four of the galaxies: UGC 4325, DDO 64, F568-3, and UGC 1281. Three galaxies, UGC 5750, F583-4, and F583-1, have concentrations too low to be consistent with ΛCDM. Specifically, the concentrations are farther from the concentrations of the NFW_{constr} halos than the expected log scatter in c of 0.18 (Bullock et al. 2001). Only the concentrations from the NFW_{free} fits of the remaining four galaxies, NGC 4395, UGC 477, F563-V2, and F563-1, are consistent with ΛCDM.

One should bear in mind that these fits are taken in the limit of minimum disk. Baryons do matter somewhat in LSB galaxies. This will drive the concentrations even lower in proper mass models.

The four galaxies for which no NFW_{free} fits could be made are fit significantly better by isothermal halos than NFW_{constr} halos. The case of F568-3 is typical: the NFW_{constr} halos overpredict the velocity at all radii interior to where they were forced to match the

observed velocity. Of the galaxies with NFW_{free} fits, UGC 5750 is a good example of the over-under-over fitting trend of of the NFW halo. This fitting trend has been observed before (e.g., BMR01; Gentile et al. 2004) and is what is being referred to when it is said that the NFW rotation curve has the wrong shape. Of the galaxies with NFW_{free} fits, UGC 5750, F583-1, and F563-1 are best fit by isothermal halos in terms of χ_r^2. UGC 5750 is the strongest case, because the value of its best-fit concentration, 0.5, is far too low, according to current ideas from cosmological simulations. NGC 4395 has a reasonable NFW concentration and a χ_r^2 favoring the NFW halo. There are signs of a possible bar or oval structure at the center of this galaxy. Mass modeling beyond the minimum-disk case may help to determine the central structure of the galaxy and whether or not the NFW halo remains a good description of the data. F583-4 and F563-V2 also have χ_r^2 in favor of the NFW halo; however, the best-fit concentration for F583-4 is bordering on the low side of expected values, and F563-V2 has too few data points to really distinguish between halo types. It is worth noting that when the small uncertainty in the first DensePak point of F563-V2 is increased to 5 km s^{-1}, neither the isothermal nor NFW fit is significantly changed. Finally, UGC 477 is equally well fitted by both isothermal and NFW halos.

In total, seven galaxies are well described by the isothermal halo, one is consistent with NFW, and three are indistinguishable. For the majority of the galaxies, NFW halos could either not be fitted to the data or had concentrations too low to be consistent with ΛCDM. As shown by NGC 4395, velocities consistent with cuspy halos can be detected in the two-dimensional data.

2.6.3 Comparison to Literature

Ten of the 11 galaxies have published pseudoisothermal and NFW halo fits to the long-slit and/or HI data. In Figure 2.13, we plot the DensePak halo parameters for each galaxy (R_c and ρ_0 for isothermal, c and V_{200} for NFW) against the minimum-disk literature values. There is gross agreement between the DensePak and literature halo parameters, showing that the addition of the new two-dimensional optical data has not substantially altered the fits. The addition of the DensePak data does, however, bring down the errors on the halo parameters by roughly a factor of 2. The DensePak parameters are listed in Table 2.2; the numbers mentioned in the text below are from the cited references.

UGC 4325– The DensePak isothermal halo parameters agree well with the results of BB02 (R_c = 2.7$\pm$0.1; ρ_0 = 100.1$\pm$2.1), and the agreement between those two datasets is better than the agreement of either set with the parameters of Swaters et al. (2003a) (R_c = 0.94; ρ_0 = 263). No NFW_{free} fit could be made to the DensePak data, and the BB02 data preferred a concentration less than 0.1 (c = 0.1, V_{200} = 3331.6). Many of the BB02 galaxies have NFW fits with unphysical (very small or negative) values of the concentration. In these cases, the concentration was set to 0.1. The NFW fits by both Swaters et al. (2003a) and van den Bosch & Swaters (2001) required very high concentration values (c = 14.8, V_{200} = 83; c = 30.9, V_{200} = 53.5, respectively). The Swaters et al. (2003a) NFW fit shows the over-under-over fitting trend and is not a good representation of the data. For this galaxy, all of the listed concentrations are far beyond the reasonable range of expected values. The DensePak, BB02, and Swaters et al. (2003a) results all favor the isothermal halo as the best fit.

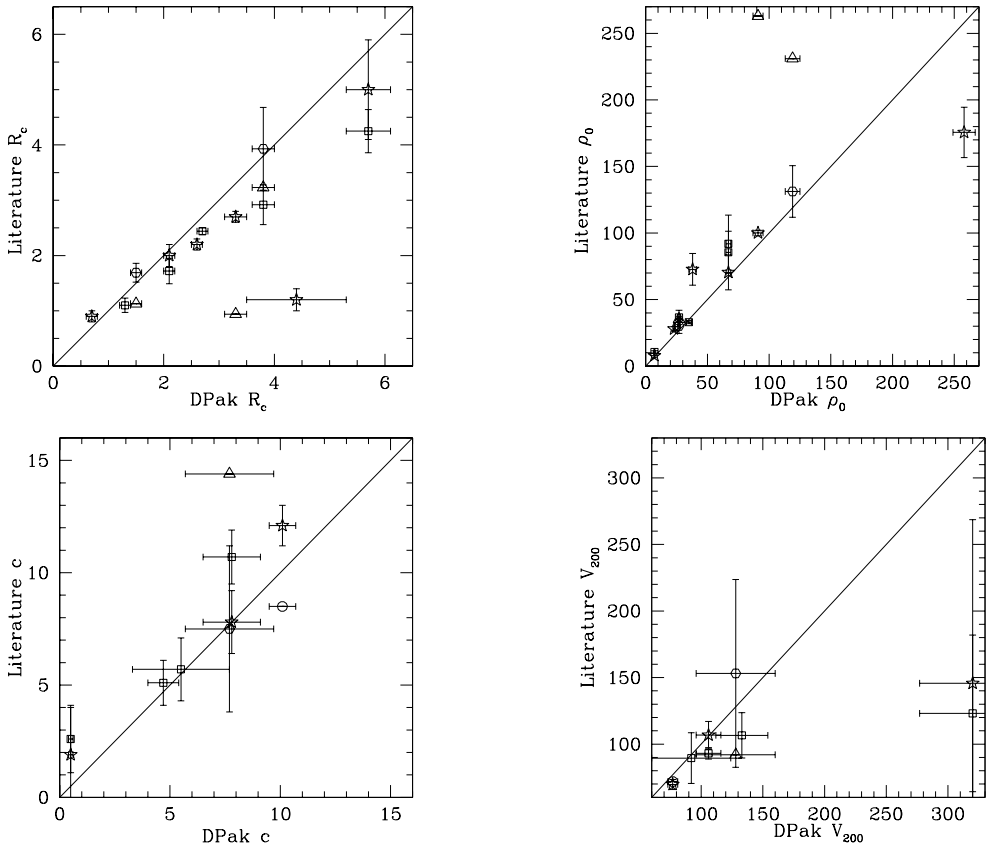

Figure 2.13: – Comparison of DensePak halo parameters to previously published values. Values of R_c and ρ_0 are displayed for the isothermal halo, and c and V_{200} are shown for the NFW halo. Stars represent the data from BB02, squares the data from BMR01, triangles the data from Swaters et al. (2003a), circles the data from van den Bosch & Swaters (2001), and hexagons the BMR01 analysis of the Swaters, Madore, & Trewhella (2000) data. The addition of the DensePak does not significantly alter the previous halo fits but does reduce the errors on the halo parameters.

F563-V2– For both the isothermal and NFW halo parameters, there is excellent agreement between the DensePak values and the results of the BMR01 analysis of the Swaters, Madore, & Trewhella (2000) data (R_c = 1.69$\pm$0.17, ρ_0 = 131.2$\pm$19.4). The error on each parameter has also been reduced by the DensePak data. The agreement is not as good with the isothermal parameters of Swaters et al. (2003a) (R_c = 1.13; ρ_0 = 231). Their NFW concentration (c = 14.4) is again much higher than the DensePak value, and

V_{200} much lower (V_{200} = 92). As previously discussed (see §5.2), there are few points in the DensePak data, making a clear distinction between halo fits difficult. Certainly, there is nothing to contradict the conclusions of both previous studies that the data to prefer the isothermal halo.

F563-1– The DensePak results agree extremely well with both the isothermal (R_c = 2.0±0.2, ρ_0 = 70.4±13.1) and NFW (c = 7.8±1.4, V_{200} = 106.8±10.3) fits of BB02. The new data shrink the formal uncertainties on the isothermal halo parameters by a considerable amount. The level of agreement with the BMR01 results (R_c = 1.72±0.23, ρ_0 = 91.9±21.6; c = 10.7±1.2, V_{200} = 93.1±4.3) is only slightly less. The isothermal halo is preferred by all three studies.

DDO 64– There is a difference between the isothermal halo parameters determined by the DensePak data and the results of BB02 (R_c = 1.2±0.2, ρ_0 = 72.7±11.9), but both studies prefer the isothermal halo to the NFW halo. The NFW results, however, are similar: no NFW_{free} fit could be made to the DensePak data, and the BB02 data favored a concentration less than 0.1 (c = 0.1, V_{200} = 1182.3). While the two isothermal fits are distinguishable, they are not too different. This galaxy seems to have real structure that is reflected in the rotation curve. The independent long-slit and DensePak data both show nonmonotonic features ("bumps and wiggles") that cannot be fit by any simple, smooth halo models of the type considered here. There is more information in the data than a simple model can represent.

F568-3– The isothermal halo parameters of the BMR01 analysis of the Swaters, Madore, & Trewhella (2000) data (R_c = 3.93±0.75, ρ_0 = 30.2±5.6) are in very good agreement with the DensePak results. Again, the DensePak parameters have lower errors.

There is also moderate agreement between the DensePak parameters and the isothermal halo parameters of BMR01 (R_c = 2.92±0.36, ρ_0 = 36.6±5.4) and Swaters et al. (2003a) (R_c = 3.23, ρ_0 = 35.3). No NFW_{free} fit could be made to the DensePak data, and all three other datasets require halos with low concentrations (BMR01 analysis of Swaters, Madore, & Trewhella (2000): c = 1.2, V_{200} = 591.1; BMR01: c = 3.2±3.7, V_{200} = 214.6±233.9; Swaters et al. (2003a): c = 1.0, V_{200} = 637). In all datasets, the isothermal halo is a better fit.

UGC 5750– There is decent agreement with the DensePak isothermal halo parameters and the results of both BB02 (R_c = 5.0±0.9, ρ_0 = 7.9±1.6) and BMR01 (R_c = 4.25±0.39, ρ_0 = 10.6±1.0). The errors are lower on the DensePak-derived parameters. All three data sets require a very low NFW concentration (BB02: c = 1.9±2.1, V_{200} = 145.7±122.9; BMR01: c = 2.6±1.5, V_{200} = 123.1±58.8). The NFW halo is not a good description of the data. Although the formal fit parameters differ for the NFW halo, the degeneracy between halo parameters is such that there is little to distinguish the resulting halo rotation curve.

NGC 4395– There is moderate agreement between the DensePak isothermal halo parameters and the values of the parameters found by BB02 (R_c = 0.9±0.1, ρ_0 = 175.6 ±18.9). The NFW_{free} concentration determined by the DensePak data is between the values listed in BB02 (c = 12.1±0.9, V_{200} = 69.7±3.8) and van den Bosch & Swaters (2001) (c = 8.5, V_{200} = 71.9). As with UGC 5750, although the formal NFW fit parameters differ, the degeneracy between halo parameters is such that there is little to distinguish the resulting halo rotation curve. BB02 find the isothermal halo to be a slightly better fit to the data than the NFW halo, whereas the DensePak data have a slight preference for

the NFW halo. The NFW halo certainly cannot be excluded, because it has a reasonable concentration in all three fits. The misalignment of the minor axis in the DensePak velocity field (see also Garrido et al. 2002; Noordermeer, Sparke, & Levine 2001) and effects from star formation (BB02) need to be considered. The presence of a bar may create strong enough noncircular motions that the true potential is underestimated. Correcting for this would cause the halo profile to become more NFW-like. However, bars are disk dynamical features and imply that the disk has mass (which has so far been ignored in the minimum-disk case) and would cause the halo profile to become more corelike.

F583-4– The agreement between the DensePak halo parameters and the halo parameters of BMR01 is slightly better for the NFW halo (c = 5.7$\pm$1.4, V_{200} = 89.5$\pm$19.0) than the isothermal halo (R_c = 1.10$\pm$0.13, ρ_0 = 85.5$\pm$15.8). Both data sets find the NFW halo to be a slightly better fit to the data.

F583-1– There is good agreement of the isothermal (R_c = 2.44$\pm$0.06, ρ_0 = 33.0 $\pm$1.1) and NFW (c = 5.1 $\pm$1.0, V_{200} = 106.6$\pm$17.0) halo parameters of BMR01 with the DensePak parameters. Both data sets find the isothermal halo to be the better description of the data.

UGC 1281– There is moderate agreement between the isothermal halo parameters of the DensePak data and the results of BB02 (R_c = 2.2$\pm$0.1, ρ_0 = 28.0$\pm$1.7). No NFW_{free} halo could be fitted to the DensePak data. The BB02 data required a very low concentration (c = 0.1, V_{200} = 785).

2.6.4 A Word about Noncircular Motions

The presence of noncircular motions may cause the circular velocity to be underestimated or, sometimes, overestimated (Swaters et al. 2003a). This effect has been suggested as a reason why cored halos appear to be preferred to those with cusps (e.g., Swaters et al. 2003a; van den Bosch & Swaters 2001). The presence of noncircular motions and the magnitude of the effect on the system can be qualitatively ascertained by looking at the velocity field. For instance, the alignment of the major and minor axes will begin to deviate from perpendicular (a mild example being NGC 4395). Or the isovelocity contours will become noticeably more kinked, wiggly, or twisted as noncircular motions increase. There are indications of noncircular motions in some of our sample of galaxies, but how significant are they?

One way of measuring this is to look at the velocity dispersion about the mean difference of the individual fiber velocities from the circular velocity. The velocity dispersions measured in this fashion for each galaxy are listed in Table 2.3. The velocity dispersions are all in the range of 6 - 10 km s^{-1}. These values are totally consistent with the typical dispersions for the gas component of galaxies and suggest that we are not seeing signs of extreme noncircular motions. If added in quadrature to the rotation velocity, dispersions of this magnitude affect only the innermost points, where the rotation velocity and velocity dispersion are comparable. We tried this exercise assuming an isotropic dispersion ($v_{circ}^2 = v_{rot}^2 + 3\sigma^2$) for the UGC 5750 DensePak data. We chose UGC 5750 because, of the galaxies with NFW fits, it is the least consistent with the NFW halo and because it has the largest differences between the halo fits at low radii. With the exception

Table 2.3. Galaxy Velocity Dispersions

Galaxy	Velocity Dispersion (km s^{-1})
UGC 4325	7.8
F563-V2	8.2
F563-1	8.1
DDO 64	6.2
F568-3	8.7
UGC 5750	8.7
NGC 4395	9.7
F583-4	9.5
F583-1	7.3
UGC 477	8.1
UGC 1281	6.9

Note. — Velocity dispersion in the DensePak data for each galaxy. Values are between 6 and 10 km s^{-1} and are consistent with the typical dispersions for the gas components of galaxies.

of only the first data point, all corrected velocities remain within the errors of the uncorrected velocities. The first data point increases by $\sim$ 8 km s^{-1}, but this does not improve the NFW_{free} fit: the concentration remains virtually unchanged (c = 0.4$\pm$0.1). A more in-depth analysis of noncircular motions will be discussed in a future paper, but this simple analysis already suggests that the magnitude of realistic noncircular motions is not likely to be sufficient to recover the high-concentration cuspy halos expected from ΛCDM structure formation simulations.

2.7 Conclusions and Future Work

We have presented the two-dimensional velocity fields and rotation curves of a sample of LSB galaxies that have been observed with DensePak. The majority of these new data have been shown to be consistent with the rotation curves of previous long-slit Hα and HI observations. In a preliminary analysis, we have combined these data and have fit the minimum-disk case for three halo models: the best-fit isothermal halo, the NFW_{free} halo with no constraints on the parameters, and the NFW_{constr} halo which was constructed to agree with ΛCDM cosmology. We found seven galaxies to prefer the isothermal halo, one to prefer the NFW halo, and three to show no clear preference. When NFW_{free} fits could be made, the concentrations were often too low, compared to the expected values for ΛCDM.

We have compared our DensePak halo fits to the results of previous studies. The DensePak halo parameters change little but do have improved uncertainties. Future work will include a detailed assessment of noncircular motions, slit placement, and mass modeling to determine the distribution of dark matter in more realistic cases than the minimum-disk scenario.

2.8 Acknowledgments

We would like to thank the referee for helpful comments. The work of R.K.d.N. and S.S.M. was supported by NSF grant AST 05-05956. This research has made use of the NASA/IPAC Extragalactic Database (NED) which is operated by the Jet Propulsion Laboratory, California Institute of Technology, under contract with the National Aero-

nautics and Space Administration. Our velocity field plots were made using a modified version of the program found at

`http://www.astro.wisc.edu/~mab/research/densepak/DP/dpidl.html`

Chapter 3

Halpha Velocity Fields of Nine Low Surface Brightness Galaxies

3.1 Overview

In this chapter we present high-resolution optical velocity fields from DensePak integral field spectroscopy for a sample of nine low surface brightness galaxies. Six of these galaxies are part of a new sample previously unobserved with DensePak. Additional DensePak observations have been obtained for three galaxies published in Kuzio de Naray et al. (2006). We present the derived rotation curves along with the NFW and pseudoisothermal halo fits to the dark matter halos. We find the six new galaxies to be better described by the isothermal halo than the NFW halo, although the quality of the fits is constrained by the limited radial coverage of the DensePak data. While we also find that the values of the halo parameters do not significantly change, the halo fits of the three previously observed galaxies are better constrained by the additional DensePak coverage.

3.2 Sample and Observations

We observed a sample of 14 low surface brightness galaxies previously unobserved with DensePak. These targets were selected primarily from the Nearby Galaxies Cata-

logue (Tully 1988). Selection criteria for these galaxies included positions satisfying $18^h \lesssim \alpha \lesssim 08^h$ and $10^\circ \lesssim \delta \lesssim 50^\circ$, inclinations between 30° and 85°, heliocentric velocities $\lesssim$ 3000 km s^{-1}, and an estimated V_{flat} (approximated by $V_{flat} \sim 0.5 W_{20} sin^{-1} i$) between roughly 50 km s^{-1} and 100 km s^{-1}. Additionally, we selected those galaxies which appear to have diffuse Hα emission and lack indicators of significant noncircular motions (e.g., strong bars or gross asymmetries). We also targeted galaxies with previous long-slit rotation curves or Hα imaging.

Because of inclement weather and telescope scheduling, we did not have Hα imaging or long-slit rotation curves for most of the galaxies in the sample prior to making the DensePak observations. Without these data, there is no way of knowing how much Hα emission will be detected by the integral field unit (IFU) until the IFU observations are actually made. Thus, our observed sample of galaxies is signal-limited; the IFU fibers detected sufficient Hα emission to create a useable velocity field in just under 50% of our target galaxies.

The galaxies were observed during the nights of 2006 August 28-30 and 2006 September 25-27. Also, during the nights of 2006 March 28-29 and 2006 April 6-8, we re-observed UGC 4325, DDO 64, and F583-1. Observations were made using the DensePak IFU on the 3.5 m WIYN telescope at the Kitt Peak National Observatory (KPNO). The instrumental setup and observing procedure for all observing runs are described in Chapter 2.3.

3.3 Data Reduction

The data were reduced following the procedure outlined in Chapter 2.4 and the reader is referred to that chapter for details. Similarly, the rotation curves were derived as discussed in Chapter 2.4 using the tilted-ring fitting program ROTCUR (Begeman 1989).

The velocity field centers were fixed to the optical centers of the galaxies, and the inclination was fixed to published values (Tully 1988; de Blok & McGaugh 1996; McGaugh, Rubin, & de Blok 2001; James et al. 2004). The systemic velocities were determined by ROTCUR. The position angle of the major axis was well constrained by ROTCUR for all of the galaxies in the new sample except for UGC 128. In the case of UGC 128, the position angle was set to the position angle of the HI velocity field of van der Hulst et al. (1993). The position angles of UGC 4325, DDO 64, and F583-1 remained fixed at the values used in Kuzio de Naray et al. (2006). The error bars on the rotation curve points derived from ROTCUR were increased to include the velocity error from centroiding accuracy, corrected for inclination.

3.4 Results for Individual Galaxies

In this section, we present the DensePak fiber positions, observed velocity fields, and rotation curves in Figures 3.1-3.3. A description of each galaxy is given and the properties of the galaxies for which a rotation curve was derived are listed in Table 3.1.

Table 3.1. Properties of Observed Galaxies

Galaxy (1)	R.A. (J2000.0) (2)	Decl. (J2000.0) (3)	μ_0(B) (mag arcsec^{-2}) (4)	Distance (Mpc) (5)	i (deg) (6)	V_{hel} (km s^{-1}) (7)	R_{max} (kpc) (8)	V_{max} (km s^{-1}) (9)	P.A. (deg) (10)	σ (km s^{-1}) (11)	References (12)
NGC 7137[a]	21 48 13.0	+22 09 34	20.1[b]	22.5	38	1669	3.2	62	44	7.1	1,10,12
UGC 11820	21 49 28.4	+14 13 52	23.7	13.3	50	1088	2.9	93	309	8.9	14,7,9
UGC 128	00 13 50.9	+35 59 39	24.2	60	57	4509	13.5	133	62	15.5	8,3,3
UGC 191	00 20 05.2	+10 52 48	22.7	17.6	39	1139	2.4	97	156	7.7	14,13,12
UGC 1551	02 03 37.5	+24 04 32	22.5	20.2	63	2663	3.8	83	114	9.7	5,11,12
NGC 959[c]	02 32 23.9	+35 29 41	20.5[d]	7.8	51	590	1.6	77	64	8.7	6,7,7
UGC 4325	08 19 20.5	+50 00 35	22.5[e]	10.1	41	514	2.9	110	52	9.0	2,2,2
DDO 64	09 50 22.4	+31 29 16	···	6.1	60	517	1.9	60	97	7.9	2,2,2
F583-1	15 57 27.5	+20 39 58	24.1	32	63	2256	5.8	72	355	8.7	4,4,4

Note. — Units of right ascension are hours, minutes, and seconds, units of declination are degrees, arcminutes, and arcseconds. Col.(1): Galaxy name. Col.(2): Right Ascension. Col.(3): Declination. Col.(4): Central surface brightness in *B*-band. Col.(5): Distance. Col.(6): Inclination. Col.(7): Heliocentric systemic velocity. Col.(8): Maximum radius of the DensePak rotation curve. Col.(9): Maximum velocity of the DensePak rotation curve. Col.(10): Position angle of major axis; see §3.3 for details. Col.(11): Velocity dispersion of the DensePak data. Col.(12): References for surface brightness, distance, and inclination.

[a] NGC 7137 = UGC 11815.

[b] *V*-band surface brightness.

[c] NGC 959 = UGC 2002.

[d] *I*-band surface brightness.

[e] Converted from *R* band assuming $B - R = 0.9$.

REFERENCES − (1) Baggett et al. 1998. (2) de Blok & Bosma 2002. (3) de Blok & McGaugh 1996. (4) de Blok, McGaugh, & Rubin 2001. (5) de Jong 1996. (6) Heraudeau & Simien 1996. (7) James et al. 2004. (8) McGaugh 2005. (9) McGaugh, Rubin, & de Blok 2001. (10) Rosenberg & Schneider 2003. (11) Swaters & Balcells 2002. (12) Tully 1988. (13) van Zee & Haynes 2006. (14) van Zee et al. 1997.

3.4.1 Results for New Sample of Galaxies

Of the 14 galaxies observed, there were eight galaxies for which meaningful velocity fields could not be constructed.[1] The Hα emission in these galaxies was too faint to be detected and/or not spread out enough across the fiber array. Velocity fields and rotation curves were derived for the remaining six galaxies in the sample, and each is described below.

NGC 7137– There were three DensePak pointings for this galaxy. The pointings are shown on the Hα image (Figure 3.1) of the galaxy obtained at the KPNO 2 m telescope. Spiral arms are clearly visible in this galaxy. The fiber velocities were the average of the Hα, [N II]λ6584, [S II]λ6717, and [S II]λ6731 lines. Hα emission was abundant and the majority of fibers detected emission. The inclination was fixed to the value in Tully (1988). The rotation curve rises steeply out to roughly 10″ then dips slightly before rising again.

UGC 11820– This galaxy is both large and diffuse on the sky. There is a central concentration of Hα emission, which is perhaps a bar, that runs roughly NE-SW and also two large, diffuse arms that extend from the end of the bar. There were three DensePak pointings along the central feature. The pointings are shown on the Hα image (Figure 3.1) of the galaxy obtained at the KPNO 2 m telescope. The fiber velocities were the average of the Hα, [S II]λ6717, and [S II]λ6731 lines. The Hα emission was sparse and only roughly half of the fibers detected emission. The inclination was fixed to the value listed in McGaugh, Rubin, & de Blok (2001).

[1] F469-2, UGC 2034, UGC 2053, UGC 11944, UGC 12048/NGC 7292, UGC 12082, UGC 12212, and UGC 12632.

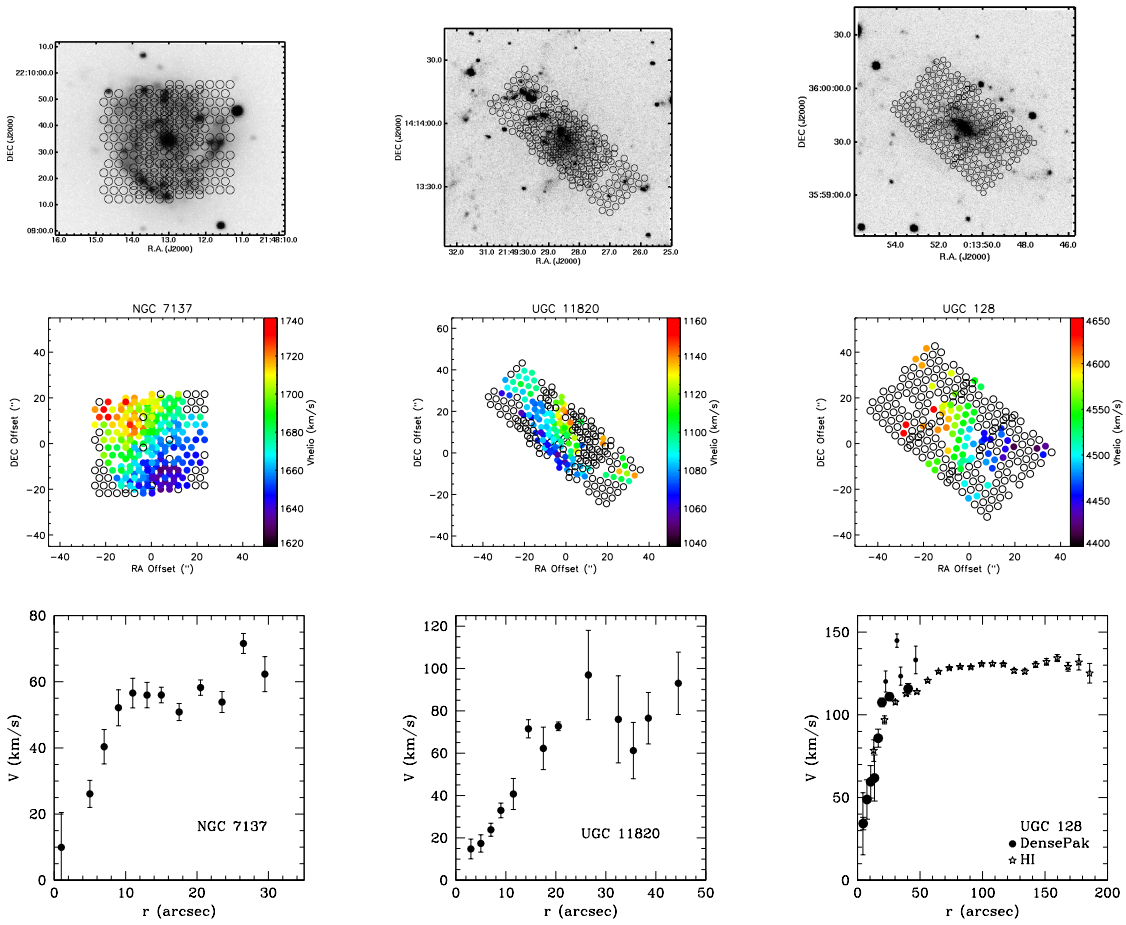

Figure 3.1: – Results for NGC 7137, UGC 11820, & UGC 128. *Top row:* Position of DensePak array on the Hα images of the galaxies. *Middle row:* Observed DensePak velocity field. Empty fibers are those without detections. *Bottom row:* DensePak rotation curves. The DensePak rotation curve of UGC 128 is plotted with the HI rotation curve of Verheijen & de Blok (1999) (stars).

UGC 128– There were three DensePak pointings across this galaxy. The pointings are shown on the Hα image (Figure 3.1) of the galaxy obtained at the KPNO 2 m telescope. The fiber velocities were the average of the Hα, [N II]λ6584, and [S II]λ6717 lines. The Hα emission in this galaxy was sparse, but the emission that was present was scattered across the three DensePak pointings such that both the approaching and reced-

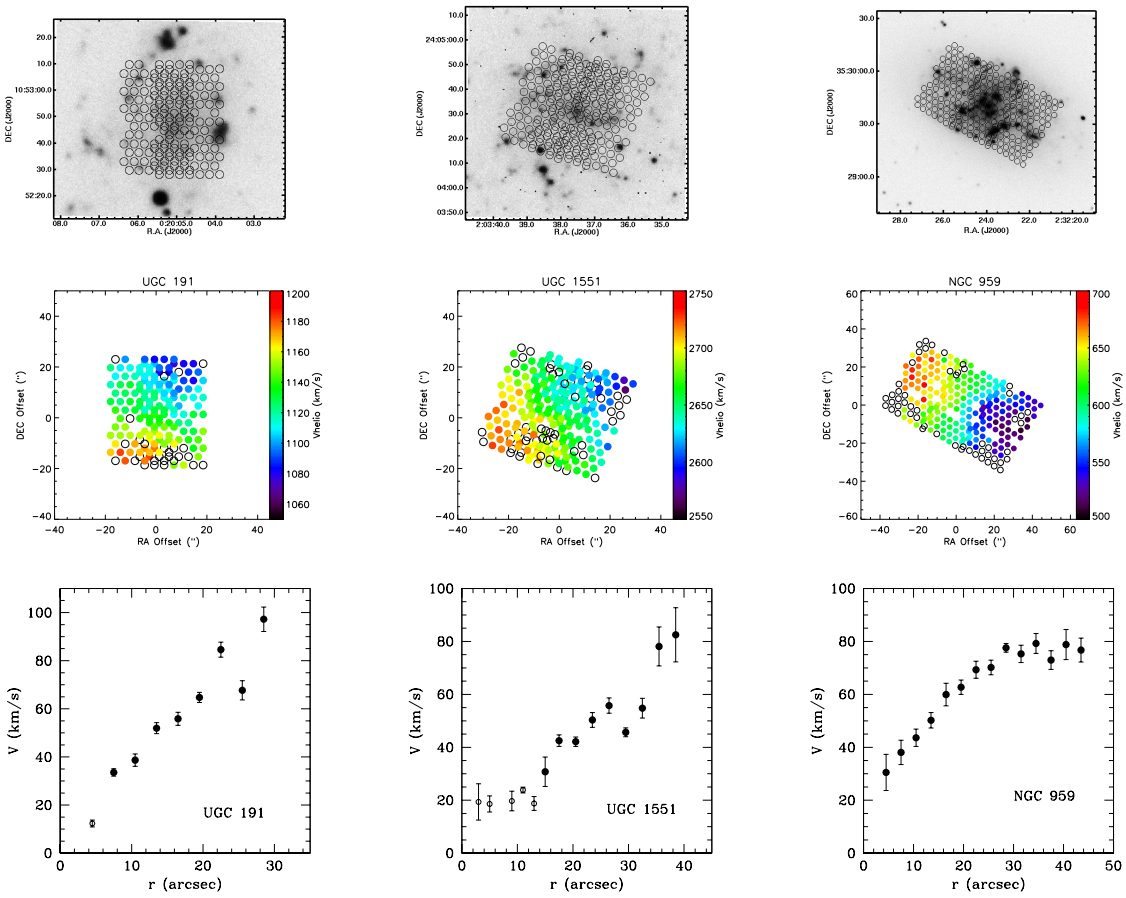

Figure 3.2: – Results for UGC 191, UGC 1551, & NGC 959. *Top row:* Position of DensePak array on the Hα images of the galaxies. *Middle row:* Observed DensePak velocity field. Empty fibers are those without detections. *Bottom row:* DensePak rotation curves. The open points in the UGC 191 and UGC 1551 rotation curves were excluded from the halo fits.

ing sides of the velocity field were mapped. The position angle was fixed to the position angle of the HI velocity field of van der Hulst et al. (1993) and the inclination was fixed to the value listed in de Blok & McGaugh (1996). The DensePak rotation curve is plotted with the HI rotation curve of Verheijen & de Blok (1999). The DensePak rotation curve is slightly steeper than the HI curve and does not go out far enough to show a clear turn-over.

UGC 191– There were two DensePak pointings for this galaxy and they are shown

on the Hα image (Figure 3.2) obtained at the KPNO 2 m telescope. The fiber velocities were the average of the Hα, [S II]λ6717, and [S II]λ6731 lines. There is ample Hα emission in the galaxy and almost every fiber had a detection. The inclination was fixed to the value in Tully (1988). The rotation curve rises linearly and has no clear turn-over.

UGC 1551– There were three DensePak pointings for this galaxy. The pointings are shown on the Hα image (Figure 3.2) of the galaxy obtained at the KPNO 2 m telescope. The fiber velocities were the average of the Hα, [N II]λ6584, [S II]λ6717, and [S II]λ6731 lines. Hα emission was detected in nearly all of the fibers. The inclination was fixed to the value in Tully (1988). There is a twist in the velocity field that is suggestive of the presence of a bar. Noncircular motions are probably important inside of 15″ where the rotation curve is mostly flat. Beyond 15″, there is a linear rise in the rotation curve.

NGC 959– There were three DensePak pointings across the length of this galaxy. The pointings are shown on the Hα image (Figure 3.2) of the galaxy obtained at the KPNO 2 m telescope. The fiber velocities were the average of the Hα, [N II]λ6584, [S II]λ6717, and [S II]λ6731 lines. Hα emission was abundant and the majority of fibers detected emission. The inclination was fixed to the value listed in James et al. (2004). The rotation curve is well-behaved with a steady rise and a turnover to $V_{flat} \sim 80$ km s^{-1}.

3.4.2 Results for Previously Observed Galaxies

Additional DensePak observations were made of three galaxies published in Kuzio de Naray et al. (2006). In this section, we describe the positions of the new DensePak

pointings, present the augmented velocity fields, and discuss the resulting changes in the rotation curves.

UGC 4325– There were four new DensePak pointings roughly through the galaxy center from SE to NW. All eight pointings are shown on the Hα image (Figure 3.3) of the galaxy obtained at the KPNO 2 m telescope. The fiber velocities were the average of the Hα and [S II]λ6717 lines. The position angle of the major axis remained fixed at the average of the position angles of previous long-slit observations (de Blok & Bosma 2002; Swaters et al. 2003a). With the addition of the new DensePak pointings, the DensePak rotation curve extends to $\sim 60''$ and remains in excellent agreement with the long-slit Hα rotation curve of de Blok & Bosma (2002).

DDO 64– There were two new DensePak pointings along the SE end of DDO 64. All five pointings are shown on the Hα image (Figure 3.3) of the galaxy obtained at the KPNO 2 m telescope. The fiber velocities were the average of the Hα and [S II]λ6717 lines. The position angle remained fixed at the value determined in de Blok & Bosma (2002). With the addition of the new DensePak pointings and an Hα image, the positions of the DensePak fibers on the galaxy have been updated and the center of the velocity field has moved east and slightly south. The new DensePak rotation curve is now consistent with the long-slit Hα rotation curve of de Blok & Bosma (2002) in the inner $20''$. Beyond $20''$, the DensePak rotation curve shows a more linear rise with less scatter than its previous version.

F583-1– There were two new DensePak pointings, one to the north and one to the east, on this galaxy. All three pointings are shown on the *R*-band image (Figure 3.3) of the galaxy from de Blok, McGaugh, & van der Hulst (1996). The fiber velocities were the

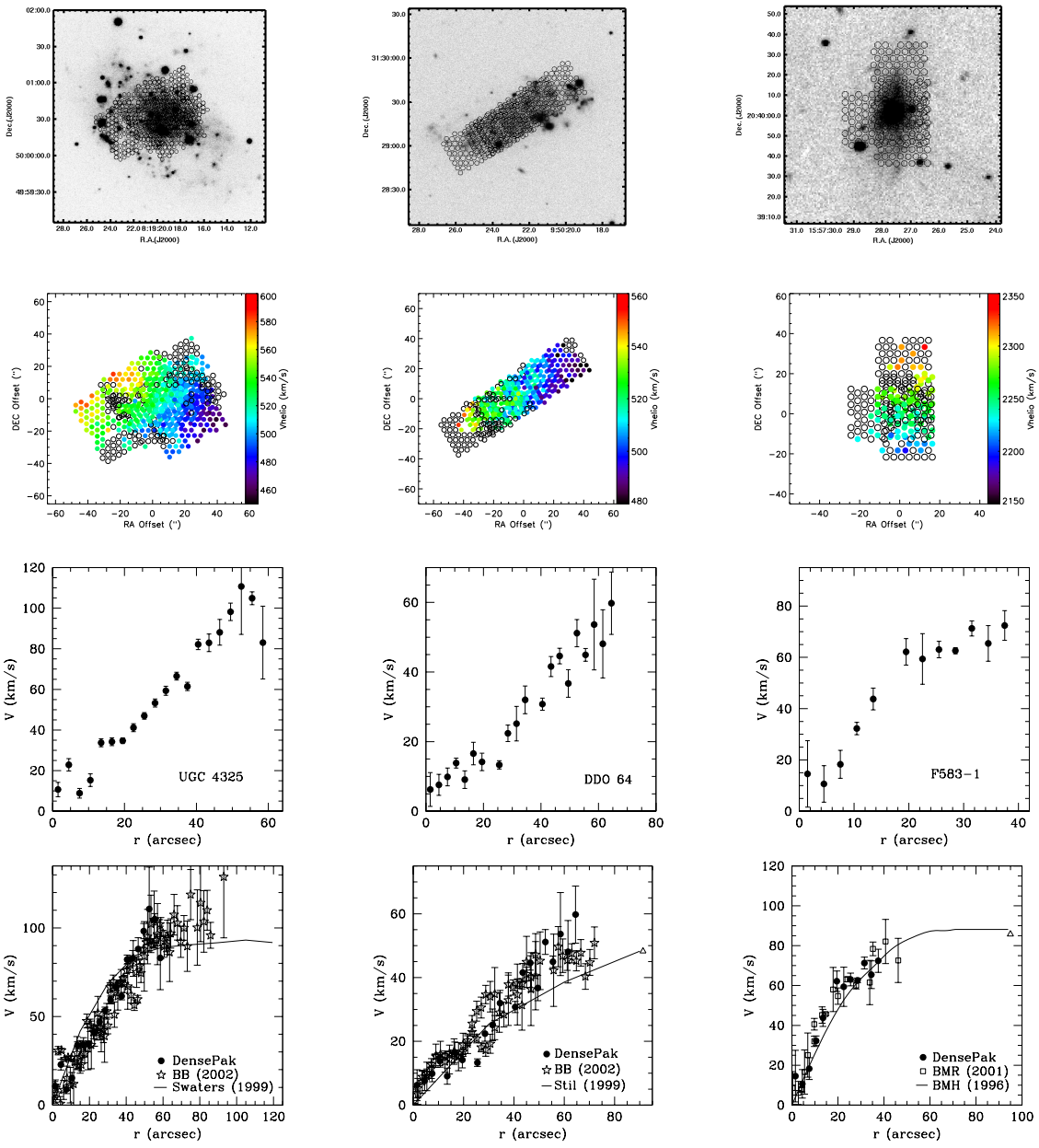

Figure 3.3: – Additional observations of UGC 4325, DDO 64, and F583-1. *Top row:* Position of DensePak array on the Hα images of UGC 4325 and DDO 64 and the *R*-band image of F583-1. *Second row:* Observed DensePak velocity field with new pointings. Empty fibers are those without detections. *Third row:* Updated DensePak rotation curves. *Bottom row:* Updated DensePak rotation curves plotted with long-slit Hα and HI rotation curves. Symbols remain the same as in Figures 2.1, 2.4, and 2.9.

average of the Hα, [S II]λ6717, and [S II]λ6731 lines. The receding side of the galaxy and more of the minor axis are now covered with the additional pointings. The position angle remained fixed at the value listed in McGaugh, Rubin, & de Blok (2001). The new DensePak rotation curve shows less scatter than the curve derived from a single DensePak pointing, and it displays a higher level of consistency with the long-slit Hα rotation curve of de Blok, McGaugh, & Rubin (2001).

3.5 Halo Fits

In this section, we present the pseudoisotherml and NFW halo fits to the DensePak rotation curves in the minimum-disk case. For those galaxies with photometry, halo fits for four assumptions of the stellar mass-to-light ratio will be presented in Chapter 4. The pseudoisothermal and NFW halo models are described in Chapter 2.6.1.1 and Chapter 2.6.1.2, respectively. In Figure 3.4, we plot the halo fits over the data, and list the parameters in Table 3.2.

3.5.1 Halo Fits to New Sample of Galaxies

We fit the minimum-disk case halo models to the entire DensePak rotation curve, and in the case of UGC 128, we combine the DensePak rotation curve with the HI rotation curve of Verheijen & de Blok (1999), using only those HI points beyond the radial range of the DensePak data. Uncertainties from possible resolution effects are avoided by using only the outer HI points.

We find the best-fit isothermal and NFW halos. We did not include the innermost

Table 3.2. Best-Fit Halo Parameters

	ISO			NFW		
Galaxy	R_c (kpc)	ρ_0 (10^{-3}M$_\odot$ pc^{-3})	χ^2_r	c	V_{200} (km s^{-1})	χ^2_r
NGC 7137	0.6±0.1	274±17	3.1	15±3	56±10	3.4
UGC 11820	1.1±0.1	274±21	2.9	...	...	...
UGC 128	2.3±0.1	66±0.6	8.5	8.9±0.2	111±0.7	9.3
UGC 191	1.7±0.1	138±10	5.8	...	...	...
UGC 1551	1.3±0.2	57±5	5.5	...	...	...
NGC 959	0.4±0.1	1117±29	1.2	23±4	76±15	1.7
UGC 4325	4.1±0.3	88±3	3.2	...	...	...
				6.9	*249*	*39*
DDO 64	3.3±0.5	43±3	3.2	...	...	...
				9.2	*62*	*12*
F583-1	2.5±0.1	30±2	0.5	4.5±0.8	120±20	1.7
				8.7	*83*	*6.5*

Note. — Best-fit halo parameters for the DensePak rotation curves. The second line in the NFW columns for UGC 4325, DDO 64, and F583-1 are the halo parameters for the NFW$_{constr}$ fits.

point of the UGC 191 rotation curve or the first five points of the UGC 1551 rotation curve in the halo fits. We exclude the innermost point of the UGC 191 rotation curve due to its unrealistically small formal error bar and the steep jump in velocity between it and the next rotation curve point. Excluding this point from the halo fit does not significantly alter the values of the halo parameters, but does improve the value of the reduced χ^2. The first five points of the UGC 1551 rotation curve were excluded because of the uncertainty of the magnitude of noncircular motions indicated by the bar-like signature in the velocity field.

NGC 7137– The isothermal halo is a slightly better fit to NGC 7137 than the NFW halo, but the difference is not particularly significant. There are "bumps and wiggles" in the rotation curve that simple, smooth halo models cannot fit. The value of the concentration, c = 15, for the NFW fit is on the high side of values expected in a ΛCDM cosmology.

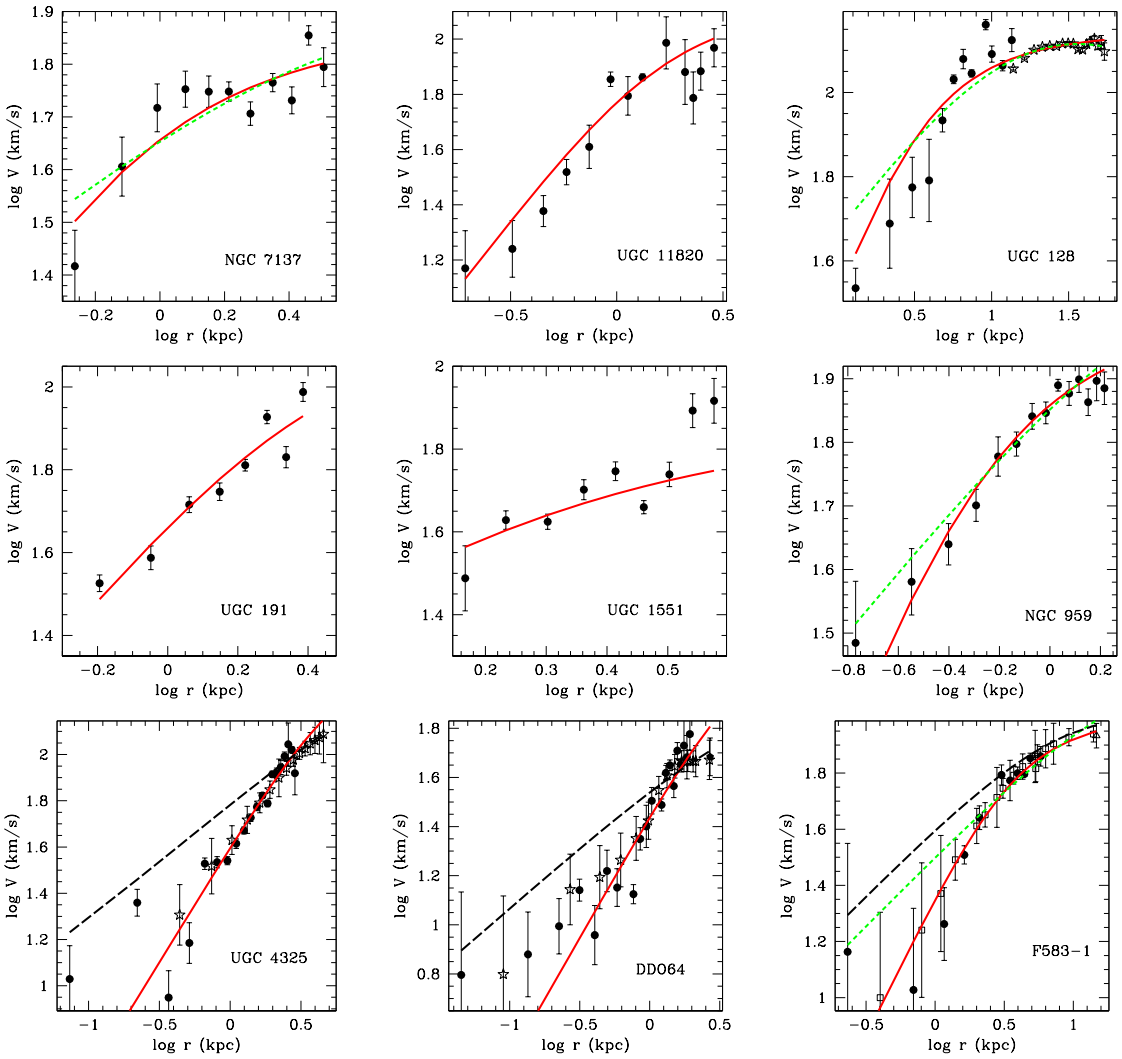

Figure 3.4: – Halo fits to the DensePak rotation curves. The red solid line is the best-fit isothermal halo, the green short-dashed line is the best-fit unconstrained NFW halo, and the black long-dashed line is the best-fit NFW$_{constr}$ halo. NFW$_{constr}$ fits were only made to UGC 4325, DDO 64, and F583-1.

UGC 11820– UGC 11820 is fit relatively well by the isothermal halo; no NFW halo could be fit to the rotation curve.

UGC 128– UGC 128 is more consistent with the isothermal halo than the NFW halo, though the value of χ_r^2 is high for both fits. The best-fitting concentration, c = 8.9,

is reasonable for a galaxy of this size in a ΛCDM cosmology. The best-fitting isothermal halo parameters for the combined DensePak+HI rotation curve are R_c = 2.3±0.1 and ρ_0 = 66±0.6. de Blok & McGaugh (1996) also fit an isothermal halo to the van der Hulst et al. (1993) HI rotation curve and find R_c = 4.0 and ρ_0 = 21.7. The differences in the halo parameters reflect the inclusion of the slightly steeper DensePak rotation curve.

UGC 191– No NFW fit could be made to the DensePak rotation curve of UGC 191. The data were fit with an isothermal halo, albeit with a large χ^2_r. The UGC 191 DensePak rotation curve is linearly rising and shows no turn-over over in the radial range covered by the DensePak data. Data points at larger radii are needed to better constrain the halo fits.

UGC 1551– An NFW fit could also not be made to the DensePak rotation curve of UGC 1551. An isothermal fit was made, but was not well-constrained. Noncircular motions are important in this galaxy, and like UGC 191, data at larger radii are necessary for constraining the halo models. UGC 1551 has a velocity dispersion of 9.7 km s^{-1}, the highest value for the galaxies in the sample after UGC 128 (see column 11 of Table 3.1). The velocity dispersion of UGC 128 may be artificially high because of the small number of fibers detecting emission. UGC 128 is also "big" by the standards of this sample (V_{flat} $\sim$ 130 km s^{-1}). While 9.7 km s^{-1} is the highest velocity dispersion detected, it is not extreme; with the exception of UGC 128, the velocity dispersions of UGC 1551 and the other galaxies all fall within the typical range of dispersions for the gas component of galaxies (e.g. Pisano, Wilcots, & Elmegreen 1998; de Blok, McGaugh, & van der Hulst 1996).

NGC 959– NGC 959 is well described by the isothermal halo and is a slightly

better fit than the NFW halo. The value of the concentration, c = 23, of the best fit NFW halo is on the high side of expected values for galaxies in a ΛCDM cosmology. Though not as pronounced as in some other galaxies (e.g., UGC 5750, Figure 2.12), the NFW fit to NGC 959 shows the over-under-over fitting trend often seen in NFW halo fits. The NFW halo over-predicts the velocities at small radii, then under-predicts the velocities at intermediate radii, and then again over-predicts the velocities at large radii.

Overall, the isothermal halo was able to fit all of the new DensePak rotation curves, and an NFW fit could be made to only three. Only one of the three NFW fits had a concentration consistent with the range expected for galaxies in a ΛCDM cosmology; the other two are on the high end of expected values. The quality of the isothermal fits is limited by the radial range of the DensePak data. Only NGC 959 has a DensePak rotation curve which clearly turns over and flattens, and it is this galaxy that has the isothermal and NFW fits with the lowest χ_r^2. That $\chi_r^2 \gg 1$ for almost all of the galaxies suggests that either the error bars have been underestimated, or that neither halo model, by itself, provides an adequate description of the data. For reasons discussed in Chapter 2.4, we have not imposed a minimum error on the rotation curve points. The velocity error from centroiding accuracy has been added to the error bars, however. Mass models including the stellar component are presented in the next chapter for those galaxies with photometry.

3.5.2 Halo Fits to Previously Observed Galaxies

In addition to the new data, we also find the best-fit minimum-disk case isothermal and NFW halos to the new DensePak rotation curves of UGC 4325, DDO 64, and

F583-1 combined with previous long-slit Hα and/or HI rotation curves, as discussed in Chapter 2.6.2. For these three galaxies, we also fit an NFW halo called NFW$_{constrained}$, as described in Chapter 2.6.2. Briefly, the constrained halo was required to match the velocities at the outer radii of each galaxy while constraining the concentration to agree with cosmology. We do not make an NFW$_{constr}$ fit to the six new galaxies, as the radial range of the data does not extend beyond the rising part of the rotation curve.

UGC 4325– The isothermal fit to UGC 4325 improves slightly with the addition of the four new DensePak pointings. An unconstrained NFW halo still could not be fitted to the data, and the poor quality of the NFW$_{constr}$ fit remains virtually unimproved. This galaxy remains best-described by the isothermal halo.

DDO 64– The two new DensePak pointings on DDO 64 help to improve the quality of both the isothermal and NFW$_{constr}$ fits. The values of the isothermal halo parameters remain within the errors of the original values, but the value of χ_r^2 decreases. While no unconstrained NFW halo fit could be made, the quality of the NFW$_{constr}$ halo significantly improves. This does not mean, however, that the NFW halo is a good fit to the data. The NFW$_{constr}$ halo continues to overshoot the data at radii interior to where it was forced to match the data. While it passes through the large errorbars on the inner rotation curve points, significant noncircular motions would need to be important all the way out to $\sim$1 kpc in order to boost the observed velocities up to the expected NFW velocities.

F583-1– The isothermal and NFW fits are significantly better constrained by the addition of the two new DensePak pointings. F583-1 remains best described by the isothermal halo. The values of the halo parameters remain within the errors of the previous values, but the value of χ_r^2 falls from 5.4 to 0.5. The new values of the isothermal

halo parameters are almost indistinguishable from the values determined by de Blok, McGaugh, & Rubin (2001): $R_c = 2.44 \pm 0.06$, $\rho_0 = 33.0 \pm 1.1$. The values of the parameters of the unconstrained NFW fit are also mostly unchanged, and χ_r^2 decreases to 1.7 from 8.7. The value of the concentration, $c = 4.5$, is still too low to be consistent with ΛCDM. The value of χ_r^2 also drops for the NFW$_{constr}$ fit, but the NFW velocities continue to over-predict the observed velocities interior to where they were forced to match the data.

3.6 Summary

We have presented the two-dimensional velocity fields and derived rotation curves for six galaxies previously unobserved with DensePak. We also have presented updated velocity fields and rotation curves of three galaxies with additional DensePak observations. Overall, we find the isothermal halo to be a better description of these nine galaxies than the NFW halo. When NFW fits could be made, the concentrations were often beyond the range of values expected for ΛCDM. We also find that the quality of both the isothermal and NFW halo fits is greatly improved when the radial range of the data extends into the flat part of the rotation curve.

Chapter 4

Mass Models

4.1 Overview

In this chapter we present isothermal and NFW halo fits for four assumptions of the stellar mass-to-light ratio, Υ_*, for a sample of low surface brightness galaxies observed with DensePak. While the details about what is assumed for the stars do not really matter, the fact that stars do not have zero mass cannot be ignored. With proper accounting of the baryons, we find the NFW halo to become increasingly inconsistent with the observations. We find a substantial cusp mass excess at the centers of the galaxies, with at least two times more mass expected in the cuspy CDM halo than is allowed by the data. We also find that $\sim$20 km s^{-1} noncircular motions are needed to reconcile the differences between the NFW halo and the observations for most of the galaxies when $\Upsilon_* = 0$.

4.2 Introduction

Low surface brightness (LSB) galaxies are dark matter-dominated down to small radii. Because of this, the velocity contribution from the baryons can often be disregarded when fitting dark matter halo models to the galaxy rotation curves. This type of fit which ignores the contribution of the stars and gas is usually called the minimum-disk case. While the dark matter is the dominant mass component of LSB galaxies at

all radii, baryons are still important. To accurately determine the distribution of the dark matter, it is necessary to properly account for the stars and gas in the galaxies and their contribution to the observed rotation. The velocity component coming from the stars is determined from the surface photometry scaled by the stellar mass-to-light ratio, Υ_*. This is a straightforward computation of the gravitational potential of the observed stars. However, the true value of Υ_* is difficult to determine, and as discussed below, can be assigned a value following a number of techniques. Similarly, the velocity component from the gas is determined using HI surface density profiles. The conversion from observed 21 cm luminosity to atomic gas mass is well understood from the physics of the spin-flip transition. A scaling factor, the inverse of the hydrogen mass fraction, is usually included to account for the helium and metals also present in the galaxies.

In Chapters 2 and 3, we have ignored the baryons in the halo fits to LSB galaxies observed with DensePak. For those galaxies with *R*-band photometry and HI surface density profiles we now include the contribution from the baryons and present the dark matter halo fits for three additional determinations of Υ_*.

4.3 Dynamical Components

There are three separate components in galaxy mass models that contribute to the observed velocities: the stars, the gas, and the dark matter. The stars, gas, and dark matter are added together in quadrature to obtain the total velocity, $V_{total}^2 = \Upsilon_* v_*^2 + V_{gas}^2 + V_{DM}^2$. In this section, we describe each of these dynamical components.

4.3.1 Stars

Galaxy photometry in combination with a stellar mass-to-light ratio, Υ_*, is used to determine the stellar contribution to the observed galaxy rotation. It is difficult to determine the true value of Υ_* of a galaxy because it depends on many factors ranging from the initial mass function to the extinction. To address this uncertainty, we consider four different scenarios for the value of Υ_*. We assume that Υ_* is constant with radius.

Zero disk– In this limiting case we ignore the contribution of the stars (Υ_*= 0) and gas and attribute all rotation to dark matter. This case is typically called 'minimum disk' in the literature; we have chosen to refer to this case as zero disk because it aptly describes the omission of the baryons. The zero disk case puts an upper limit on the slope and/or concentration of the halo density profile. The results for the zero disk case were presented in Chapters 2 and 3 (and were referred to as minimum-disk) and are reproduced here for completeness. Two galaxies from Chapter 2, UGC 1281 and UGC 477, are excluded from mass models beyond zero disk because of their high inclinations and possible associated line-of-sight integration effects. Photometry is unavailable for the galaxies in Chapter 3; mass models beyond zero disk will not be presented.

Minimal disk– Though commonly employed, the zero disk case is unphysical. We next consider a more realistic minimal contribution of the stars and the gas. The Υ_* is determined from population synthesis models (see below) and then scaled by 0.5 (see McGaugh 2005) to simulate a lightweight IMF.

Popsynth– Here Υ_* is determined using the population synthesis models of Bell et al. (2003). For a scaled Salpeter IMF, (*B*–*R*) and ($B-V$) colors are related to Υ_*. This is

Table 4.1. Galaxy Parameters

Galaxy	h (kpc)	(B–R)	Υ_* (Pop)	References
UGC 4325	1.6	0.85	1.14	1,3
F563-V2	2.1	0.51[a]	0.88	2,4
F563-1	2.8	0.96	1.36	2,5
DDO 64	1.2	0.9[b]	1.24	1
F568-3	4.0	0.94	1.32	2,5
UGC 5750	5.6	0.9[b]	1.24	2,2
NGC 4395	2.3	... [c]	1.40	1
F583-4	2.7	0.8	1.06	2,6
F583-1	1.6	0.9	1.24	2,6

Note. — Col.(2): Scale length (kpc). Col.(4): Υ_* for the popsynth case as determined from the colors. Col.(5): References for h and (B–R), respectively: (1) de Blok & Bosma (2002) (2) de Blok, McGaugh, & Rubin (2001) (3) van den Bosch & Swaters (2001) (4) de Blok & McGaugh (1997) (5) de Blok, van der Hulst, & Bothun (1995) (6) de Blok, McGaugh, & van der Hulst (1996).
[a] ($B-V$) color.
[b] Multicolor photometry unavailable; assuming (B–R)=0.9 for dwarf galaxies.
[c] Multicolor photomety unavailable; assuming Υ_*=1.4.

our best estimate of the baryonic mass from the perspective of stellar populations. The popsynth model also includes the gas contribution. Colors and corresponding Υ_* are listed in Table 4.1.

Maximum disk– We also consider the case where the Υ_* is scaled up as far as the data will allow. In high surface brightness galaxies, this approach usually fits the inner rotation curve well. In LSB galaxies, the shape of the stellar rotation curve is often not well-matched to the observed rotation curve. We have chosen a Υ_* that allows the stellar rotation curve to match the inner rotation curve points as well as possible, sometimes overshooting the innermost point in order to hit the next few. These Υ_* are usually higher than those determined from the popsynth models, and in some cases (e.g., F583-4) are substantially higher.

To model the stellar disk we have used the R-band photometry presented in de Blok,

van der Hulst, & Bothun (1995), Stil (1999), Swaters (1999), and Swaters et al. (2002). The GIPSY task ROTMOD was used to determine the rotation of the disk assuming a vertical sech^2 distribution with a scale height z_0=h/6 (van der Kruit & Searle 1981). The stellar rotation curve computed from the photometry was resampled at the same radii as the combined DensePak+long-slit+HI rotation curves.

Each estimator of Υ_* has its advantages and disadvantages. The zero disk Υ_* is often adopted and is useful because it provides an upper limit on the dark matter. Unfortunately, it is an unphysical assumption. Population synthesis models best represent what we know about stars, however, sometimes the data will allow a larger Υ_*. And although Υ_{*MAX} often seems too large with respect to Υ_{*POP}, disk features like bars and spiral arms require a large disk mass (McGaugh & de Blok 1998; Fuchs 2003) and support high Υ_{*MAX}.

4.3.2 Gas

The gas present in galaxies also contributes to the observed galaxy rotation. HI is the dominant gas component, but to include helium and metals, the HI data are scaled by a factor of 1.4. Substantial amounts of molecular gas are not obviously present in LSB galaxies (de Blok & van der Hulst 1998; Schombert et al. 1990). The total mass of H_2 is almost certainly much less than that of HI (Mihos, Spaans, & McGaugh 1999). Moreover, in brighter galaxies H_2 is known to trace the stars (Regan et al. 2001), so at most represents a slight tweak to Υ_*. The contribution of the gas to the observed velocity is considered in the minimal, popsynth, and maximum disk cases.

The HI surface density profiles presented in de Blok, McGaugh, & van der Hulst

(1996), van der Hulst et al. (1993), and Swaters (1999) were used to model the gas disk. The GIPSY task ROTMOD was used to determine the rotation of the disk assuming a thin disk. The gas rotation curve was resampled at the same radii as the combined DensePak+long-slit+HI rotation curves.

4.3.3 Dark Matter Halo

In LSB galaxies there is ususally a considerable amount of observed rotation unaccounted for after subtracting off the velocity of the stellar and gas disks, even in the maximum disk case. The remaining rotation is usually attributed to dark matter. While there have been a number of dark matter models proposed in the literature, we fit two of the most prominent competing profiles: the pseudoisothermal halo and the NFW profile (Navarro, Frenk, & White 1996, 1997).

As presented in Chapter 2, the pseudoisothermal halo describes a dark matter halo that has a core of roughly constant density. By construction, it produces flat rotation curves at large radii. In the zero disk case, the isothermal halo has been shown to provide a "good" description of the galaxy data presented in Chapters 2 and 3.

Numerical simulations show that the density of CDM halos rises steeply toward the halo center. The exact value of the inner slope of the CDM halo varies slightly depending on the simulation (e.g., Moore et al. 1999b; Reed et al. 2003; Navarro et al. 2004; Diemand et al. 2005). From an observational perspective, there is very little to distinguish the various flavors of cuspy CDM halos, and we choose to fit the data with the NFW halo described in Chapter 2.

4.4 Results for Individual Galaxies

In this section, we present the isothermal and NFW halo fits for the four scenarios of Υ_*. The halo parameters are listed in Tables 4.2 and 4.3. Figures 4.1-4.9 plot the halo fits over the data.

As Υ_* increases and the baryons become responsible for more of the observed velocity, less room is available for dark matter and the NFW halo becomes increasingly difficult to fit to the data. The best-fit concentrations drop to very small, and sometimes negative, values. In these cases, we forced an NFW fit with c = 1.0. The halo parameters of forced fits are italicised in the tables.

UGC 4325– UGC 4325 is clearly best described by an isothermal halo; an NFW halo could not be fit to the data for any Υ_* scenario. With Υ_{*MAX} = 4.5, the stellar rotation curve is able to describe the data well out to a radius of $\sim$ 1.3 kpc, as compared to $\lesssim$ 0.4 kpc for Υ_{*POP} = 1.14. Because the baryons are able to explain so much of the data in the maximum disk case, there is little room left for a dark matter isothermal halo. When this happens, the cored halo becomes very nearly hollow with ρ_0 decreasing to a very small value and R_c increasing to a large number. For the maximum disk case of UGC 4325, we forced an isothermal halo fit by fixing V_h to approximately the observed velocities of the outer rotation curve and then varying R_c such that V_{TOT} follows the data. In this fit, the resulting R_c is a lower limit and ρ_0 is an upper limit.

F563-V2– As discussed in Chapter 2 for the zero disk case, F563-V2 has too few data points to really distinguish between halo types. This remains true for the other Υ_* scenarios as well. The value of Υ_* can be turned up to 4.0 in the maximum disk case,

Table 4.2. Isothermal Halo Parameters

Galaxy	ZERO DISK				MINIMAL DISK			
	R_c	ρ_0	χ^2_r	Υ_*	R_c	ρ_0	χ^2_r	Υ_*
UGC 4325	4.1±0.3	88±3	3.2	0.0	4.6±1.5	77±5	3.1	0.57
F563-V2	1.5±0.1	119±6	0.71	0.0	1.4±0.2	114±20	0.68	0.44
F563-1	2.1±0.1	67±2	0.43	0.0	2.0±0.2	61±10	0.48	0.68
DDO 64	3.3±0.5	43±3	3.2	0.0	4.1±3.8	37±6	3.3	0.62
F568-3	3.8±0.2	27±1	1.2	0.0	4.0±0.5	22±3	1.5	0.66
UGC 5750	5.7±0.4	7.1±0.3	0.83	0.0	6.5±1.1	5.2±0.6	0.84	0.62
NGC 4395	0.7±0.1	258±9	2.9	0.0	0.57±0.05	318±42	2.7	0.70
F583-4	1.3±0.1	67±2	0.67	0.0	1.2±0.2	66±16	0.62	0.53
F583-1	2.5±0.1	30±2	0.50	0.0	2.4±0.2	30±3	0.59	0.62

Galaxy	POPSYNTH				MAXIMUM DISK			
	R_c	ρ_0	χ^2_r	Υ_*	R_c	ρ_0	χ^2_r	Υ_*
UGC 4325[a]	6.2±3.3	66±5	3.2	1.14	*2.5*	*45*	*11*	4.5
F563-V2	1.4±0.2	102±20	0.75	0.88	4.7±5.9	7.1±8.8	1.4	4.0
F563-1[b]	2.1±0.2	54±10	0.50	1.36	4.2±1.2	13±6	0.83	6.5
	...	...	...	...	12.5±9.0	2.7±1.6	1.3	10.0
DDO 64[a]	5.9±11.1	32±5	3.5	1.24	*1.5*	*24*	*2.2*	5.0
F568-3	4.7±0.8	16±3	1.8	1.32	6.1±1.8	10±3	2.5	2.3
UGC 5750	7.5±1.6	4.1±0.5	0.95	1.24	9.8±3.2	2.6±0.5	1.3	2.2
NGC 4395[a]	0.50±0.04	355±50	2.8	1.40	*19*	*0.32*	*4.1*	9.0
F583-4[a]	1.2±0.2	63±16	0.62	1.06	*8*	*1.4*	*1.2*	10.0
F583-1[b]	2.5±0.2	27±3	0.60	1.24	3.6±0.5	14±2	0.83	5.0
	...	...	...	...	6.9±1.7	5.2±0.9	2.0	10.0

Note. — R_c is in kpc; ρ_0 is in 10^{-3} $M_\odot$ pc^{-3}.
[a] The baryons can account for most of the velocity in the maximum disk fit. See text for details of fit.
[b] As discussed in the text, F563-1 and F583-1 have two possible values of Υ_{*Max}.

leaving essentially no room for an NFW halo; a fit was forced with c = 1.0. NFW halos could be fit to the zero, minimal, and popsynth cases, however, and the values of the best-fitting concentrations, c = 7.7, 8.4, and 7.8, respectively, are comparable to values expected from simulations. Because of the c-V_{200} degeneracy that allows halos of different (c, V_{200}) to look the same over a finite range of radius (de Blok, McGaugh, & Rubin 2001), these three NFW fits are essentially indistinguishable. This is an example of where the zero disk assumption is reasonable for LSB galaxies.

F563-1 – The isothermal halo fits the F563-1 data better than the NFW halo, though the values of the best-fitting concentrations are consistent with values expected in ΛCDM.

Table 4.3. NFW Halo Parameters

Galaxy	ZERO DISK c	V_{200}	χ^2_r	Υ_*	MINIMAL DISK c	V_{200}	χ^2_r	Υ_*
UGC 4325	*6.9*	*249*	*40*	0.0	*1.0*	*1002*	*12*	0.57
F563-V2	7.7±2.0	128±32	0.40	0.0	8.4±1.5	105±17	0.46	0.44
F563-1	7.8±1.3	106±10	0.88	0.0	7.6±1.3	100±9	0.89	0.68
DDO 64	*9.2*	*62*	*20*	0.0	*1.0*	*376*	*6.5*	0.62
F568-3	*8.2*	*110*	*12*	0.0	*1.0*	*465*	*3.9*	0.66
UGC 5750	0.5±0.1	320±43	1.7	0.0	*1.0*	*167*	*1.7*	0.62
NGC 4395	10.1±0.6	77±4	2.1	0.0	11.5±1.0	63±4	2.1	0.70
F583-4	5.5±2.2	92±32	0.41	0.0	5.7±1.4	83±18	0.41	0.53
F583-1	4.5±0.8	120±20	1.7	0.0	5.1±1.2	102±21	1.8	0.62

Galaxy	POPSYNTH c	V_{200}	χ^2_r	Υ_*	MAXIMUM DISK c	V_{200}	χ^2_r	Υ_*
UGC 4325	*1.0*	*897*	*12*	1.14	*1.0*	*283*	*12*	4.5
F563-V2	7.8±1.7	104±20	0.52	0.88	*1.0*	*203*	*1.1*	4.0
F563-1[a]	7.0±1.3	102±11	0.90	1.36	*1.0*	*283*	*1.0*	6.5
	···	···	···	···	*1.0*	*210*	*1.5*	10.0
DDO 64	*1.0*	*332*	*6.4*	1.24	*1.0*	*146*	*2.6*	5.0
F568-3	*1.0*	*404*	*4.3*	1.32	*1.0*	*317*	*5.2*	2.3
UGC 5750	*1.0*	*141*	*1.9*	1.24	*1.0*	*101*	*2.4*	2.2
NGC 4395	12.5±1.1	61±4	2.2	1.40	···	···	···	9.0
F583-4	5.8±1.5	86±19	0.40	1.06	···	···	···	10.0
F583-1[a]	4.9±1.2	110±26	1.9	1.24	*1.0*	*298*	*2.1*	5.0
	···	···	···	···	*1.0*	*173*	*3.3*	10.0

Note. — V_{200} is in km s^{-1}. Italicized halo parameters are forced fits. See text for details.
[a] As discussed in the text, F563-1 and F583-1 have two possible values of Υ_{*Max}.

The baryons can account for the majority of the observed rotation in the maximum disk case and a forced NFW fit was made with the concentration fixed at 1.0. Stellar population models set Υ_{*POP} = 1.36 for F563-1. With this value of the Υ_*, the stellar rotation curve just grazes the innermost observed rotation curve point. The Υ_{*MAX} can be substantially turned up such that the stellar rotation curve matches the data more closely. If Υ_{*MAX} = 6.5, V_* overshoots the innermost rotation curve point, but matches the cluster of points at $\sim$ 1.5 kpc and even crosses the lower errorbars on points between 5 kpc and 10 kpc. The shape of the observed rotation curve is well-matched when Υ_{*MAX} = 10.0; V_* goes through the upper errorbars on points $\lesssim$ 2 kpc and agrees well with the data between 5 kpc and 10 kpc. Fitting the inner observed rotation curve points or the overall rotation

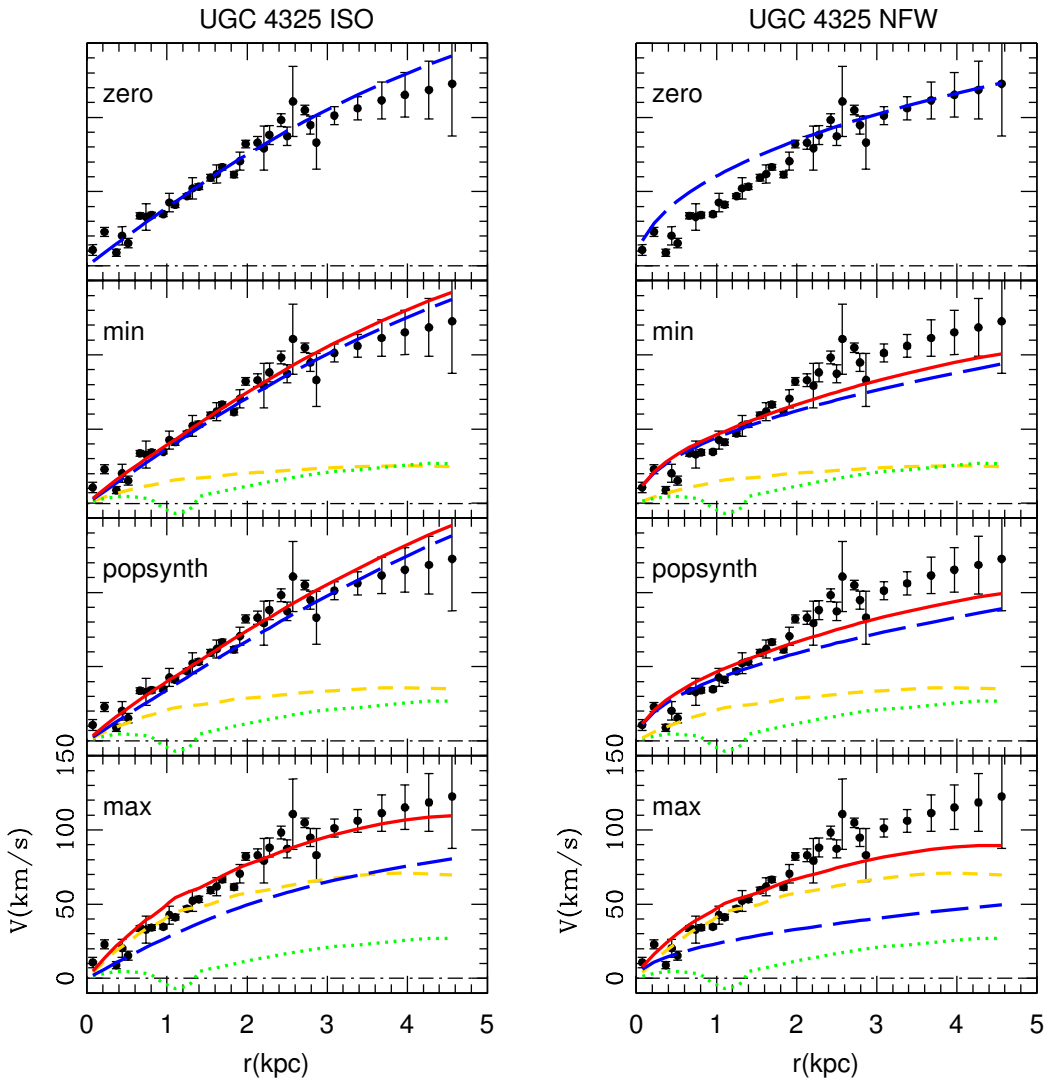

Figure 4.1: – Isothermal and NFW halo fits for UGC 4325. The green dotted line is the rotation curve of the gas disk, the gold short-dashed line is the rotation curve of the stellar disk, the blue long-dashed line is the rotation curve of the dark matter halo, and the red solid line is the total model curve.

curve shape are both equally valid approaches to defining Υ_{*MAX}, so we use both values in our halo fits.

F563-1 is a good example of how the choice of Υ_* affects the mass models, and

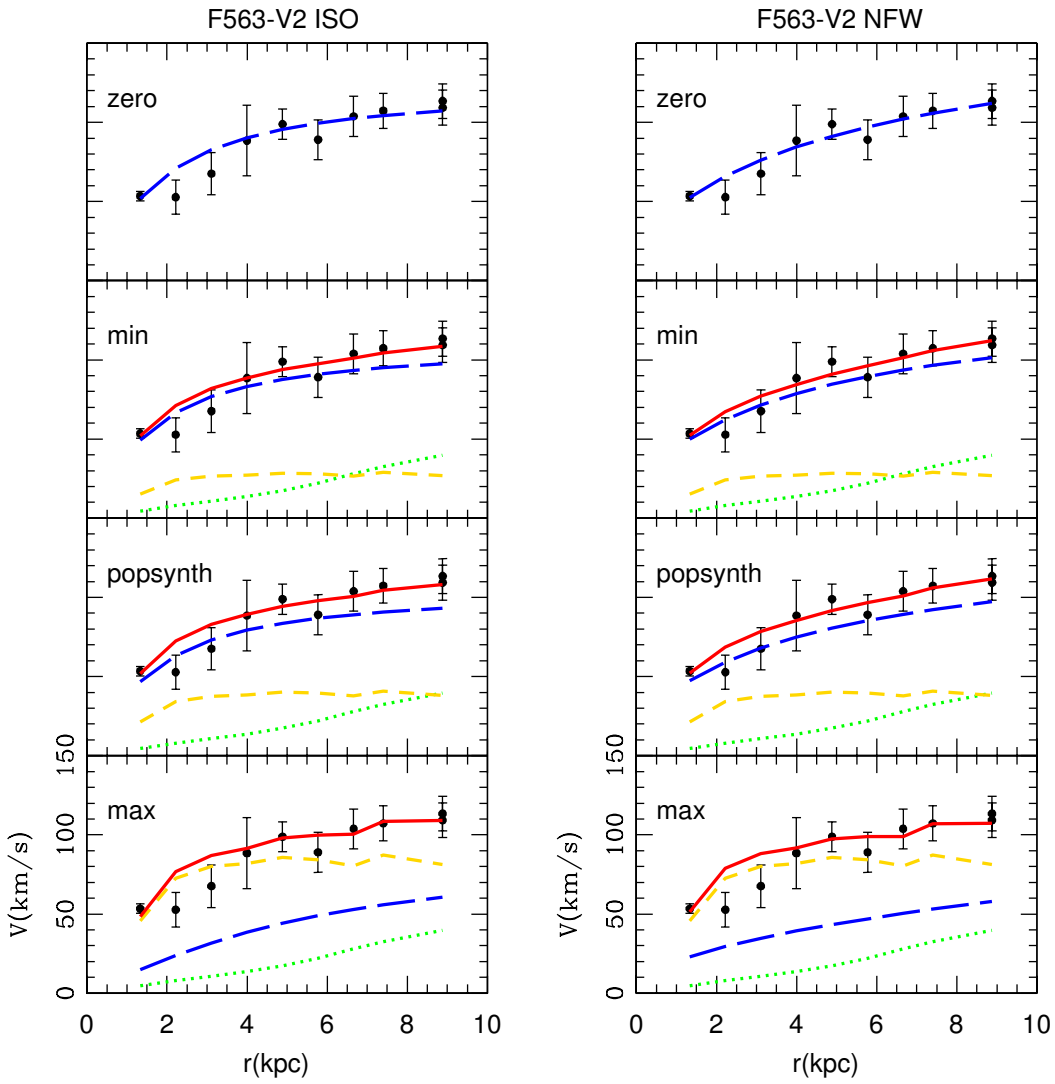

Figure 4.2: – Isothermal and NFW halo fits for F563-V2. Line types are described in Figure 4.1.

the degeneracy between the luminous and dark components. While Υ_{*POP} is our best estimate for the stars, the data will clearly allow a higher Υ_*. To constrain the degeneracy between the stars and dark matter in cases like this, we need more information. The stellar velocity dispersion perpendicular to the disk, for instance, would help to put limits on the disk mass.

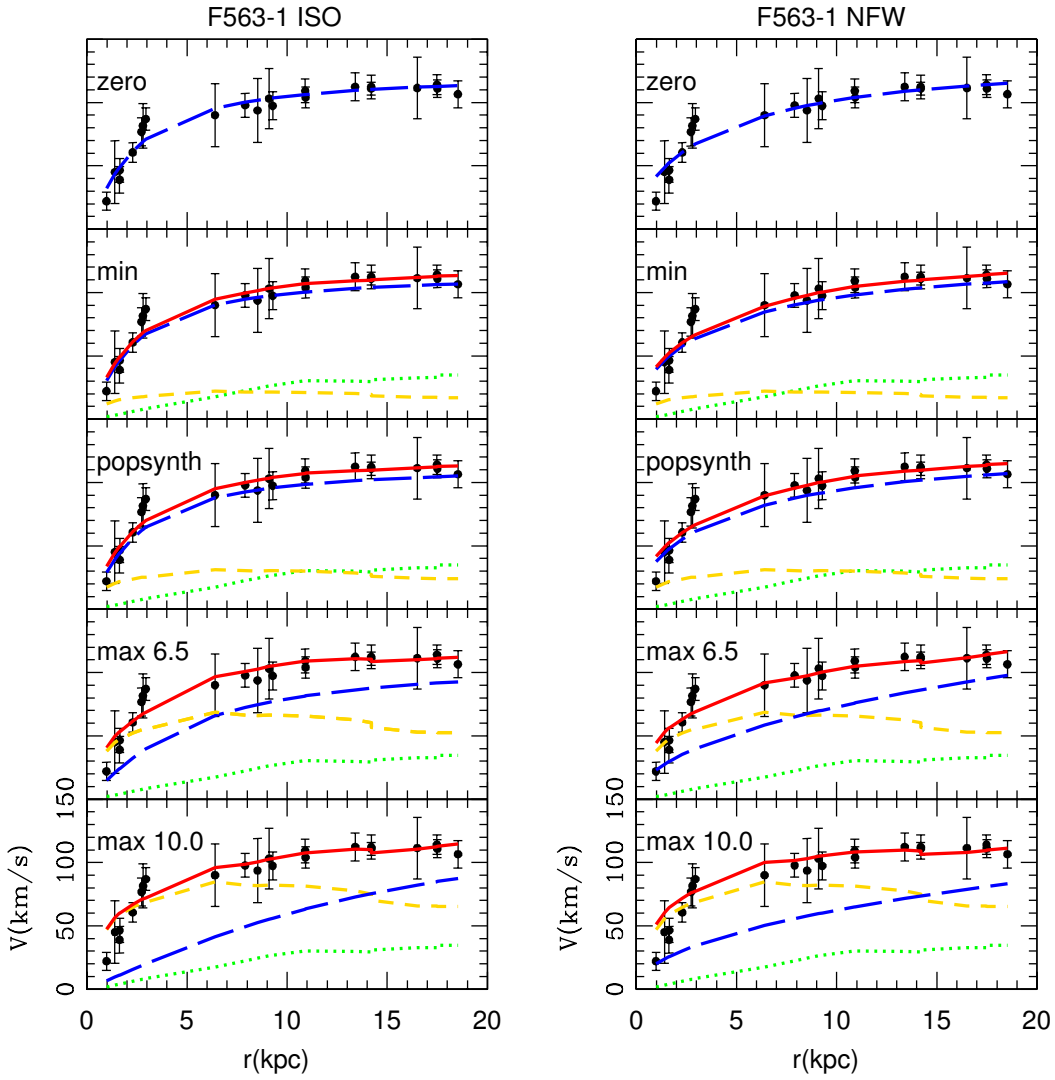

Figure 4.3: – Isothermal and NFW halo fits for F563-1. Line types are described in Figure 4.1.

DDO 64– As HI surface density profiles were unavailable for this galaxy, the baryons in the mass models are represented by the stars only. Multicolor photometry was also unavailable, so a (B–R) = 0.9 color was assumed for this dwarf galaxy. DDO 64 is better described by the isothermal halo than the NFW halo; forced c = 1 NFW fits are made for each value of Υ_*. The stellar rotation curve falls below the observed rotation

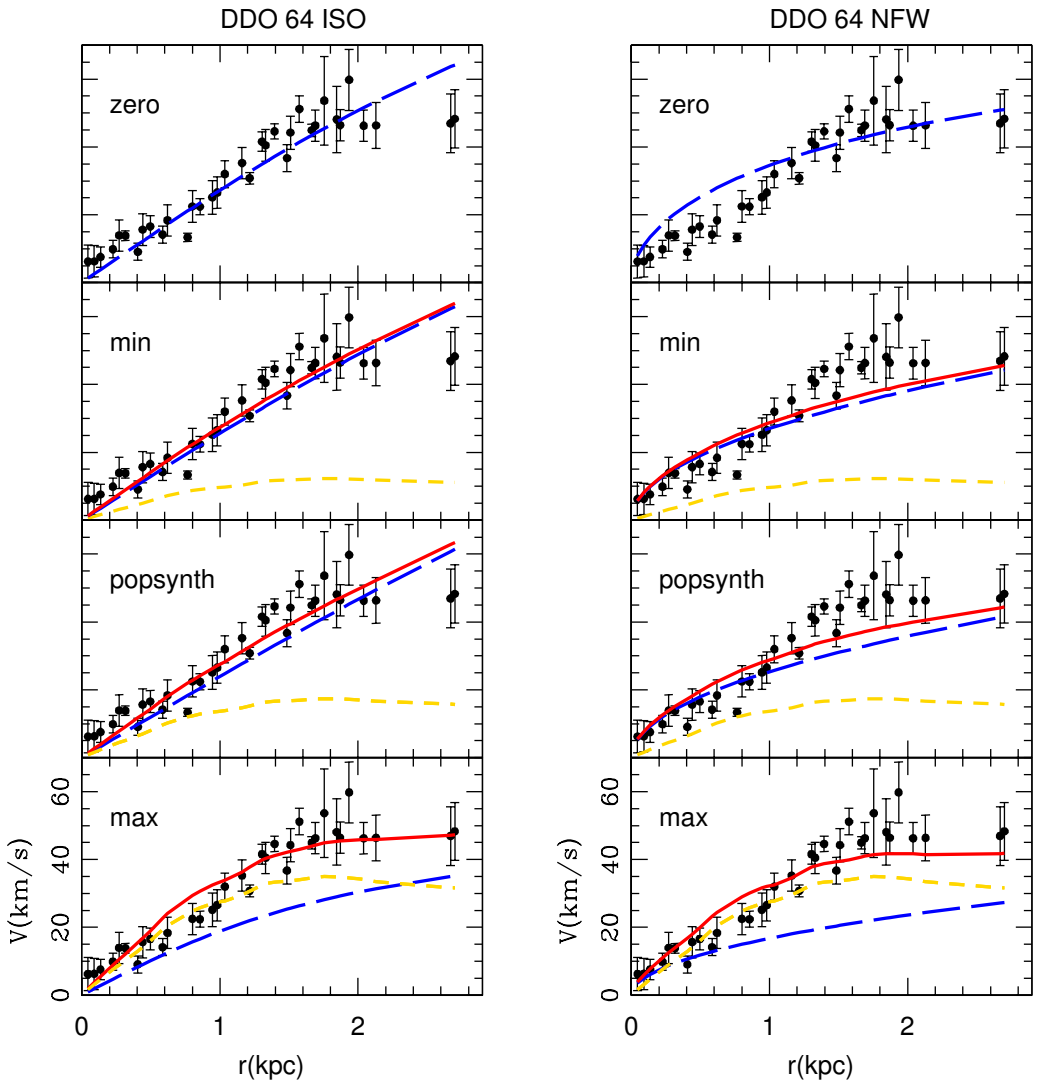

Figure 4.4: – Isothermal and NFW halo fits for DDO 64. Line types are described in Figure 4.1.

curve with the exception of two low points in the popsynth case, Υ_{*POP} = 1.24. In the maximum disk case with Υ_{*MAX} = 5.0, however, V_* is able to follow the data very well out to just past 1 kpc, and is even consistent with a data point at $\sim$ 1.5 kpc. With Υ_{*MAX} = 5.0, the stars are able to account for most of the observed rotation, and the displayed isothermal halo fit is the upper limit on ρ_0 and the lower limit on R_c.

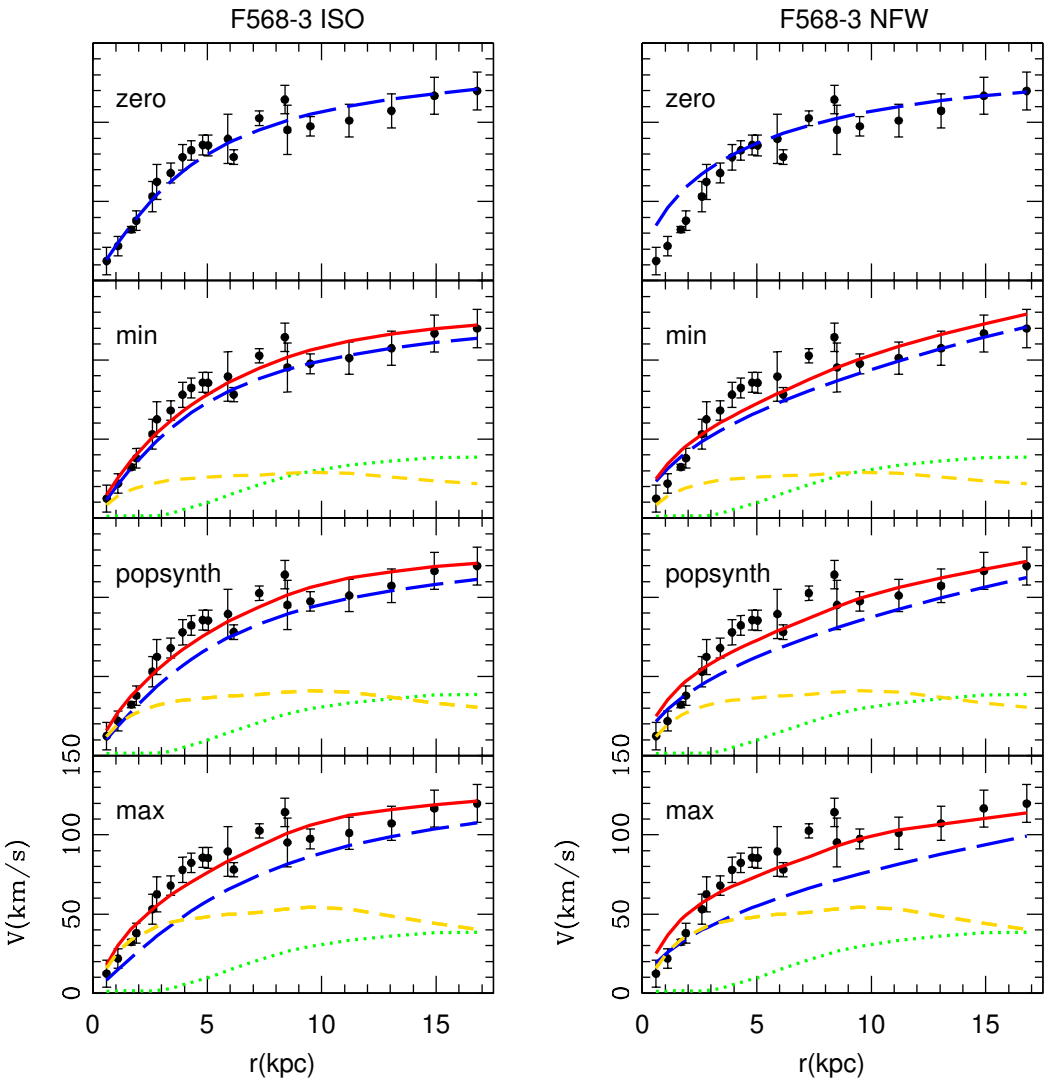

Figure 4.5: – Isothermal and NFW halo fits for F568-3. Line types are described in Figure 4.1.

F568-3– F568-3 is fit well by isothermal halos; only forced NFW fits could be made to the data. The shape of the stellar rotation curve is not well-matched to the observed rotation curve and is only able to describe the inner 2 kpc of data, even in the maximum disk case.

UGC 5750– Because multicolor photometry was unavailable, a (*B*–*R*) = 0.9 color

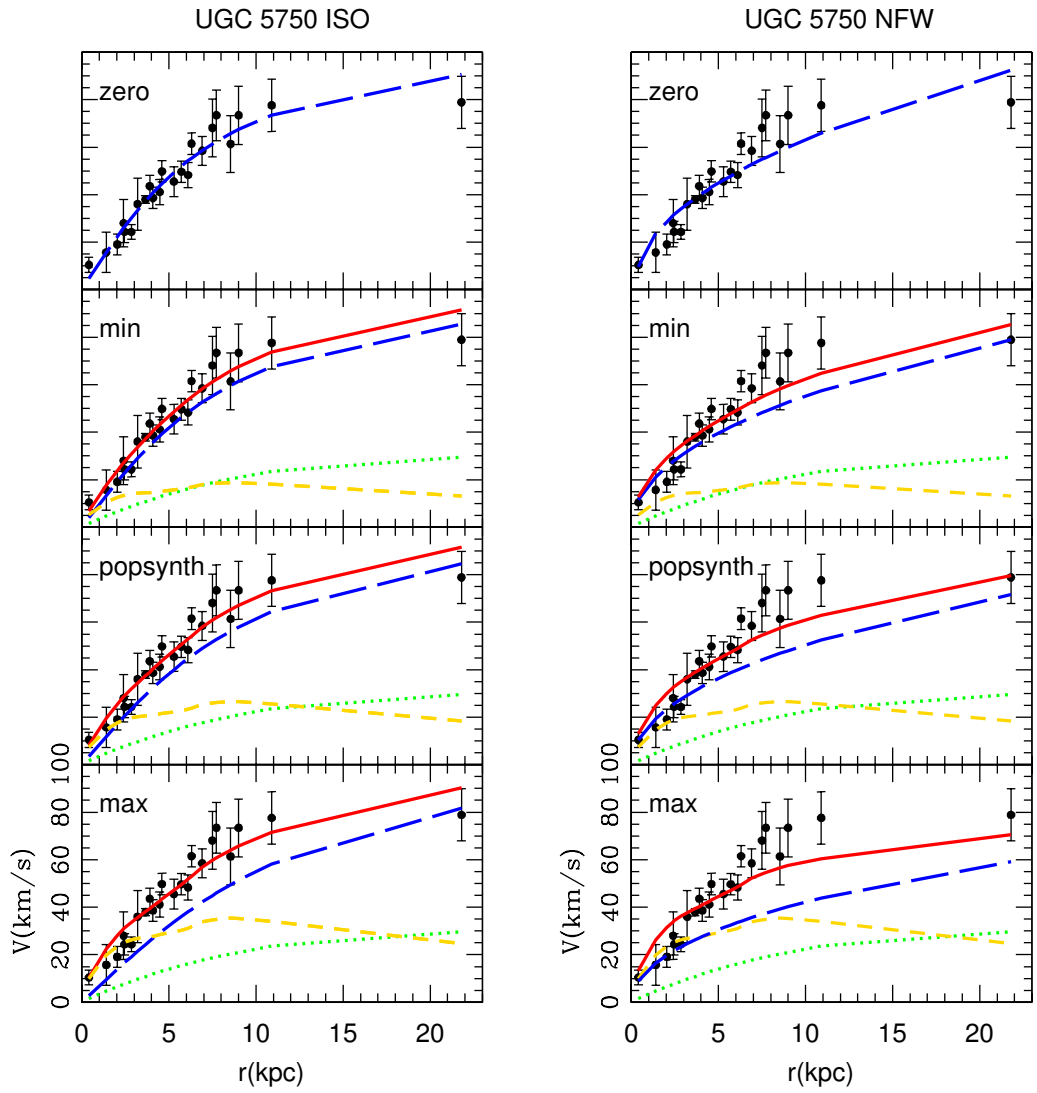

Figure 4.6: – Isothermal and NFW halo fits for UGC 5750. Line types are described in Figure 4.1.

was assumed for this galaxy. Excellent isothermal fits were made for UGC 5750; the NFW halo provides very poor fits. Like F568-3, there is not a substantial difference between Υ_{*POP} and Υ_{*MAX}.

NGC 4395– Multicolor photometry was unavailable for this galaxy and Υ_{*POP} = 1.4 was assumed for the popsynth model. The NFW halo is a slightly better fit to NGC

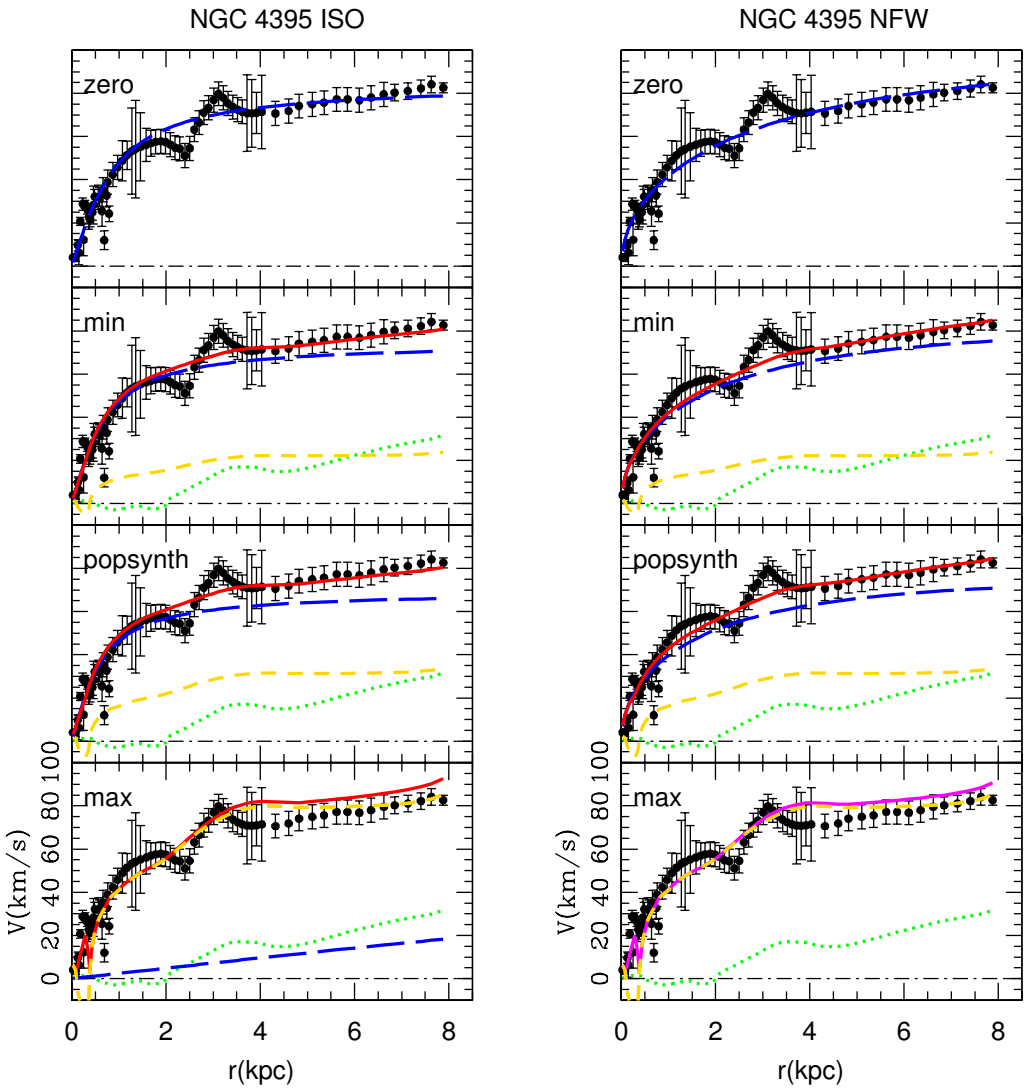

Figure 4.7: – Isothermal and NFW halo fits for NGC 4395. Line types are described in Figure 4.1. The magenta line is the total baryonic rotation curve. See text for details.

4395 than the isothermal halo, and the best-fitting concentrations are consistent with expectations from ΛCDM. There is a substantial difference between Υ_{*POP} and Υ_{*MAX}. For Υ_{*POP} = 1.4, V_* is well below the observed rotation curve; however, for Υ_{*MAX} = 9.0, V_* is able to trace the data out to 8 kpc, the entire length of the rotation curve. Because

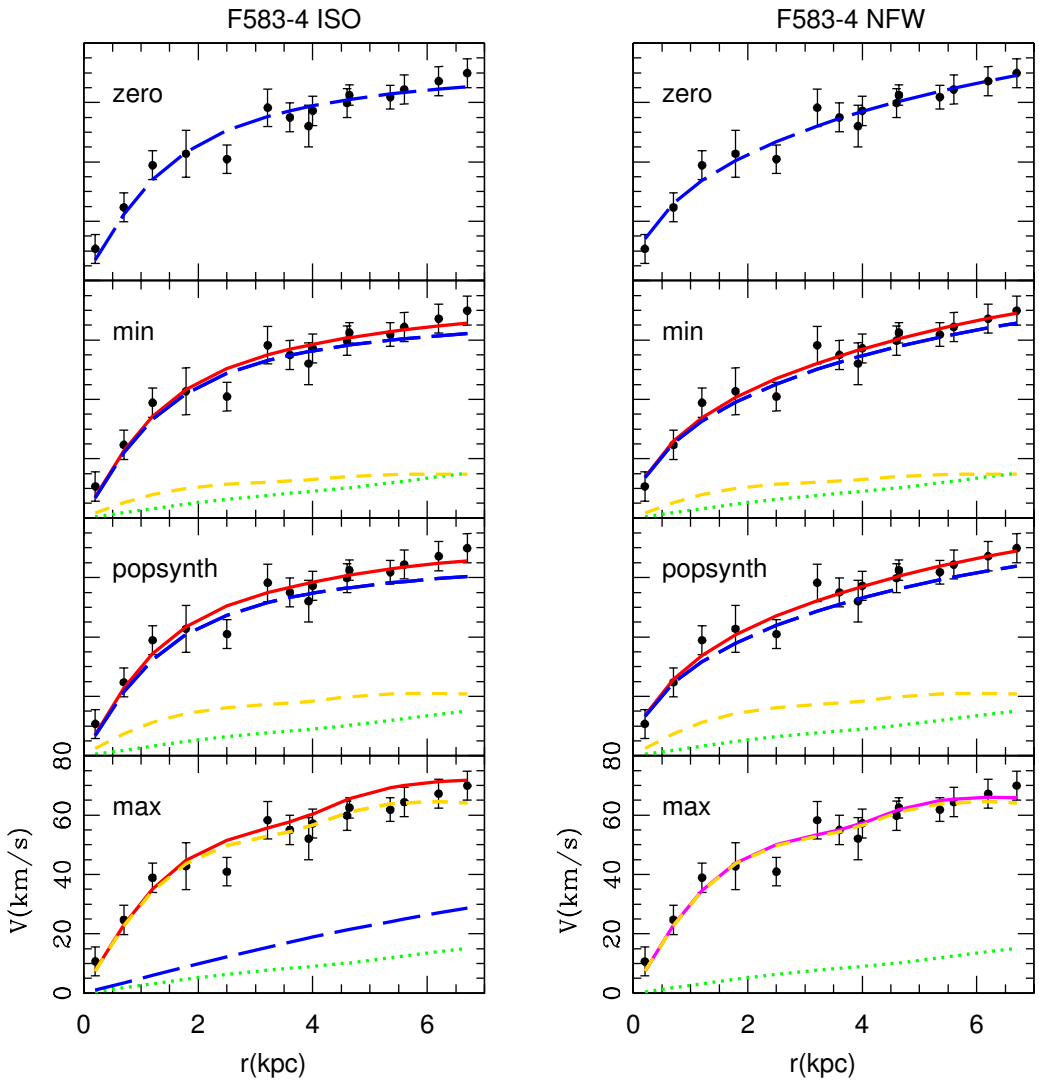

Figure 4.8: – Isothermal and NFW halo fits for F583-4. Line types are described in Figure 4.1. The magenta line is the total baryonic rotation curve. See text for details.

the baryons can explain the observed rotation so well in the maximum disk case, the data want an isothermal halo with an almost hollow core. We force a fit with an upper limit on ρ_0 and a lower limit on R_c. The baryons do such a good job of explaining the observed rotation in the maximum disk case that there is not even room for an NFW halo with c = 1.0. In the NFW maximum disk plot in Figure 4.7, the magenta line represents the total

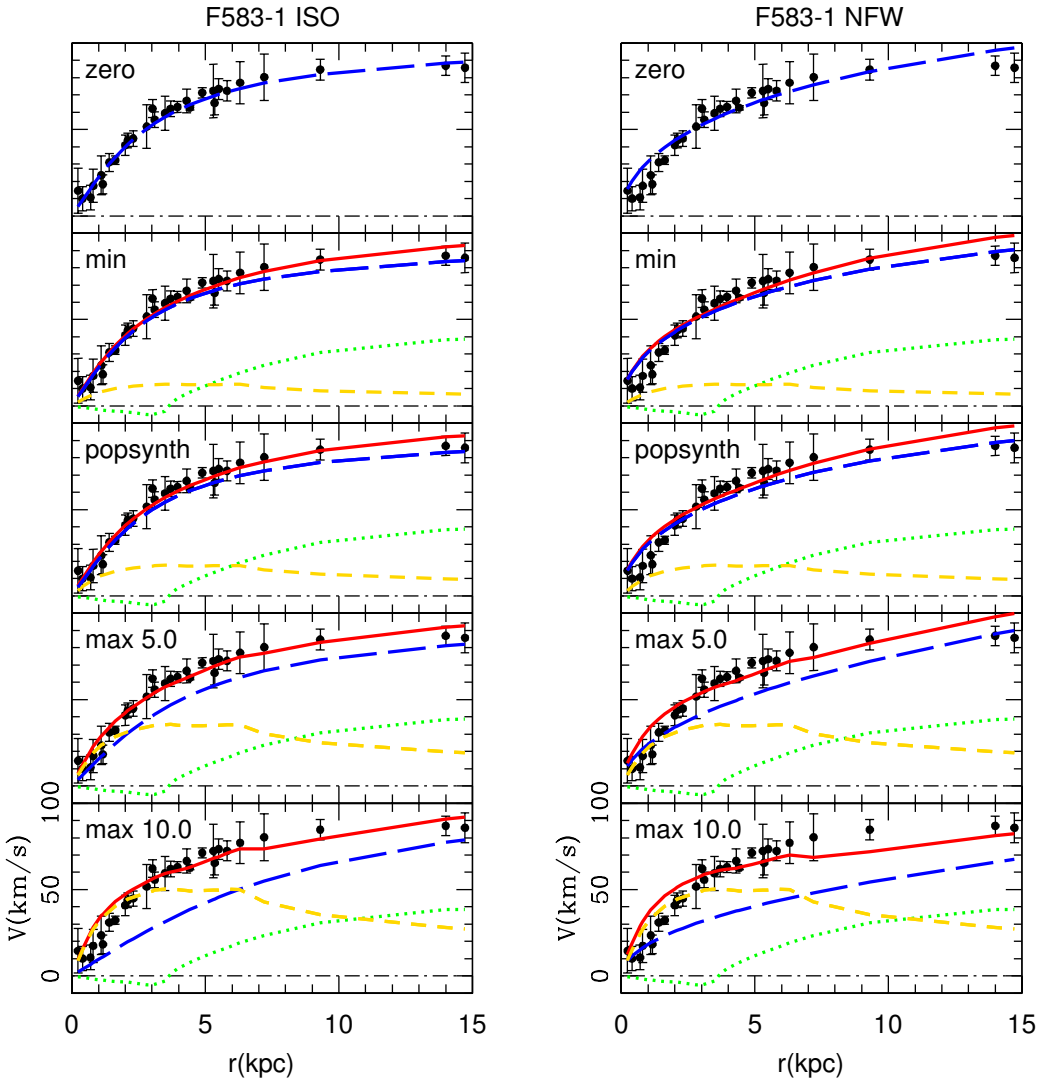

Figure 4.9: – Isothermal and NFW halo fits for F583-1. Line types are described in Figure 4.1.

baryonic rotation curve, $V^2_{disk} = V^2_* + V^2_{gas}$.

F583-4– The isothermal halo is a good description of the data. The NFW halo fits are comparable, although the values of the concentrations are on the low side of expected values from simulations. The stellar rotation curve is far below the data at all radii for the popsynth $\Upsilon_{*POP} = 1.06$. The entire observed rotation curve can be well described by

the stellar rotation curve when Υ_{*MAX} is turned up to 10.0. In this case, there is very little room left for a dark matter halo, and only a limiting isothermal halo fit is made. Like NGC 4395, there is not enough velocity left for an NFW halo with c = 1.0, and the magenta line in the maximum disk NFW plot in Figure 4.8 represents the total baryonic rotation curve.

F583-1– F583-1 is better fit by the isothermal halo than the NFW halo. Additionally, the best-fitting NFW concentrations are on the low side of expected values from ΛCDM. Like F563-1, we consider two values of Υ_{*MAX}. With Υ_{*MAX} = 5.0, V_* goes through the data within $\sim$ 1.5 kpc. V_* goes through the upper errorbars on the inner rotation curve, through the data at $\sim$ 2 kpc, and then through the lower errorbars on the data out to $\sim$ 3.5 kpc when Υ_{*MAX} = 10.0.

4.5 Discussion

While one would like to know the true Υ_* for each galaxy, our data do not indicate that a particular estimator of Υ_* is any better than another. We find that the parameters of both the isothermal and NFW halo fits do not change much as Υ_* changes. This confirms that the details about what is assumed for the stars in LSB galaxies do not really matter. Unfortunately, it also means that without additional information, we cannot constrain Υ_* in galaxies like F563-1 and F583-1 where a wide range of Υ_* are applicable.

Though the exact assumption about the stars may be unimportant, the stars cannot be entirely ignored. In reality, stars do not have zero mass. In fact, as the velocity contribution from the stars becomes more important (i.e., as Υ_* goes up), there is increasingly

less room for dark matter at the centers of the galaxies. In particular, it becomes more difficult to fit the centrally concentrated NFW halo, so much so, that maximum disk and the NFW halo are mutually exclusive.

4.5.1 Cusp Mass Excess

In Chapter 2.6.2 we defined a constrained NFW halo, NFW_{constr}, which was constructed to have a cosmologically-consistent concentration by forcing the halo to match the velocities at the outer radii of each galaxy. We can now find NFW_{constr} halos for the dark matter rotation curves for each determination of Υ_*. The rotation curves of the NFW_{constr} halos over-predict the observed velocities interior to where they are forced to agree. We can evaluate the difference between this expected CDM rotation curve and the observed dark matter rotation curve in terms of velocity difference, or alternatively, as a cusp mass excess. We can ask what the difference is between the expected cuspy NFW halo mass and the dark matter mass that is allowed by the data. In the left panel of Figure 4.10, we show the observed dark matter rotation curves of F568-3 for the zero, minimal, popsynth, and maximum disk models. We also show the constrained NFW halo for each dark matter rotation curve. In the right panel of Figure 4.10, we plot the same data in terms of mass using $M = V^2R/G$. To prevent a cluttered plot, we show only the results for the popsynth model. The solid line is the enclosed mass as a function of radius for the NFW_{constr} halo. The dashed line is the enclosed mass of the observed dark matter. We have not smoothed the data, so V_{DM} is a bit jittery between $\sim$ 6-8 kpc; *M(r)*, however, is displayed using a smoother version of the data. The NFW_{constr} halo has been forced to

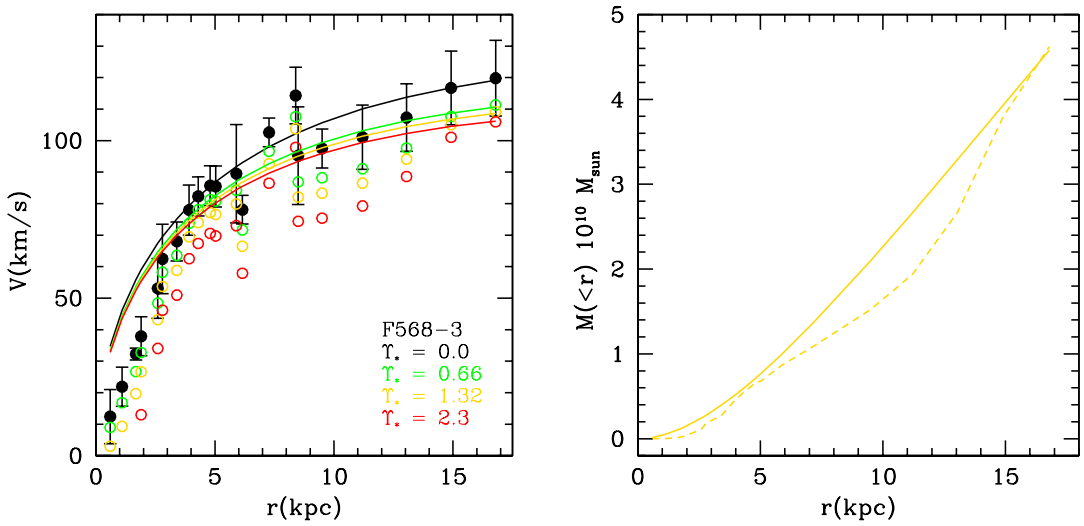

Figure 4.10: – *Left:* Comparison of the dark matter rotation curve for different values of Υ_* with the expected NFW rotation curves for F568-3. *Right:* Total dark matter mass as a function of radius for Υ_{*POP}. The solid line is the dark matter mass predicted by CDM; the dashed line is the dark matter mass allowed by the data. The two curves have been forced to meet at large radii; interior to this, CDM predicts more mass at all radii than is actually observed.

match the data at large radii; interior to this, however, there is less mass observed at all radii than is expected.

In Figure 4.11 we plot the ratio of the observed dark matter mass to the constrained cusp mass as a function of radius for each galaxy. This ratio approaches 1 at large radii where the data have been forced to agree. Near the centers of the galaxies there is a substantial cusp mass excess; there is at least two times more mass expected in the cuspy halo than is allowed by the data. At all radii, the cusp mass excess becomes larger as the baryons become increasingly more important.

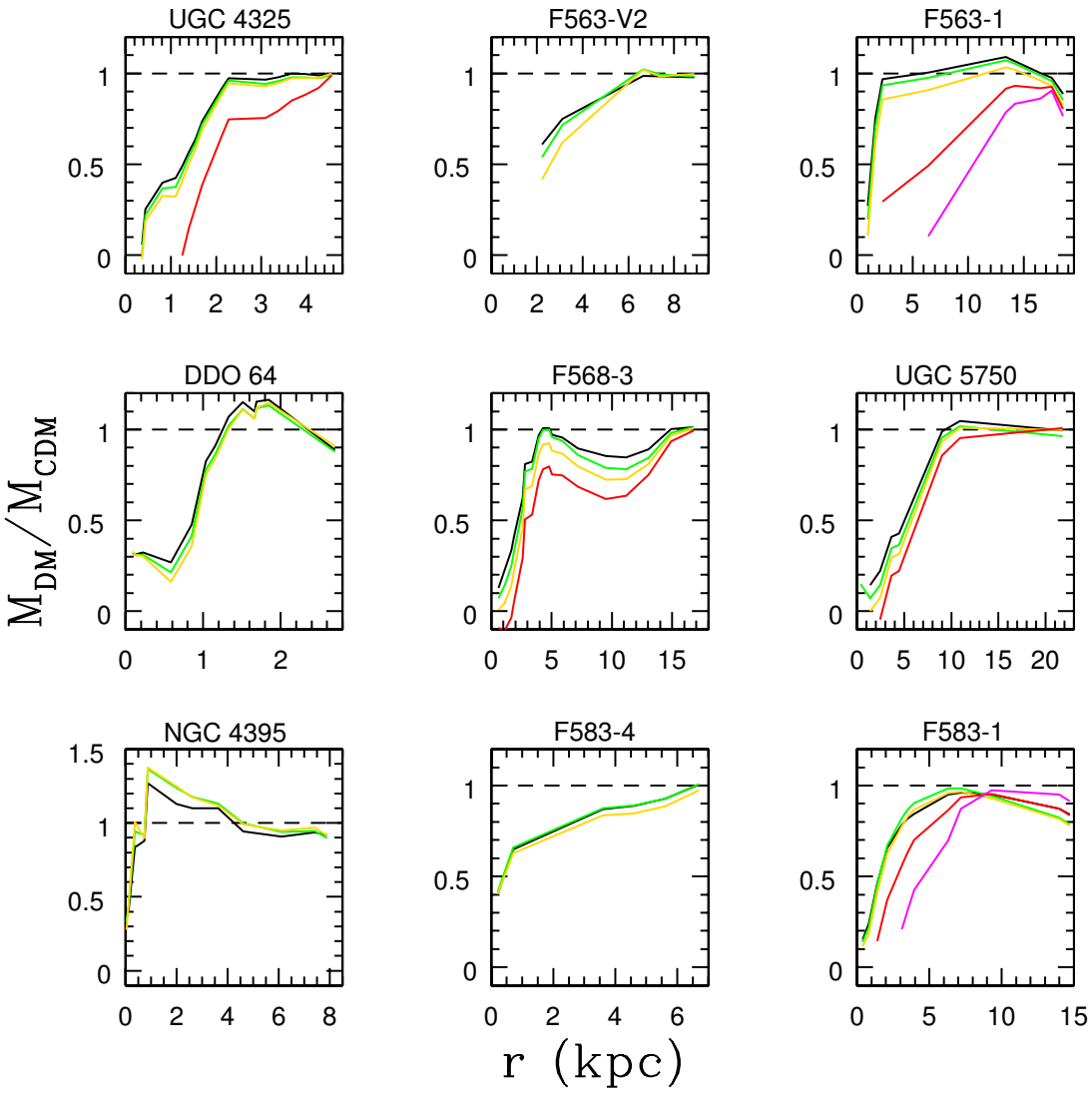

Figure 4.11: – Ratio of the observed dark matter mass to the constrained cusp mass as a function of radius. The black, green, gold, and red (magenta) lines are the zero, minimal, popsynth, and maximum disk cases, respectively. Near the centers of the galaxies there is a substantial cusp mass excess with at least two times more mass expected in the cuspy halo than is allowed by the data.

4.5.2 Reconciling the Cusp Mass Excess with Noncircular Motions

In our analysis so far, we have assumed that the observed velocity is the circular velocity ($V_{circ} = V_{obsv}$). If noncircular motions are present, the true circular velocity may

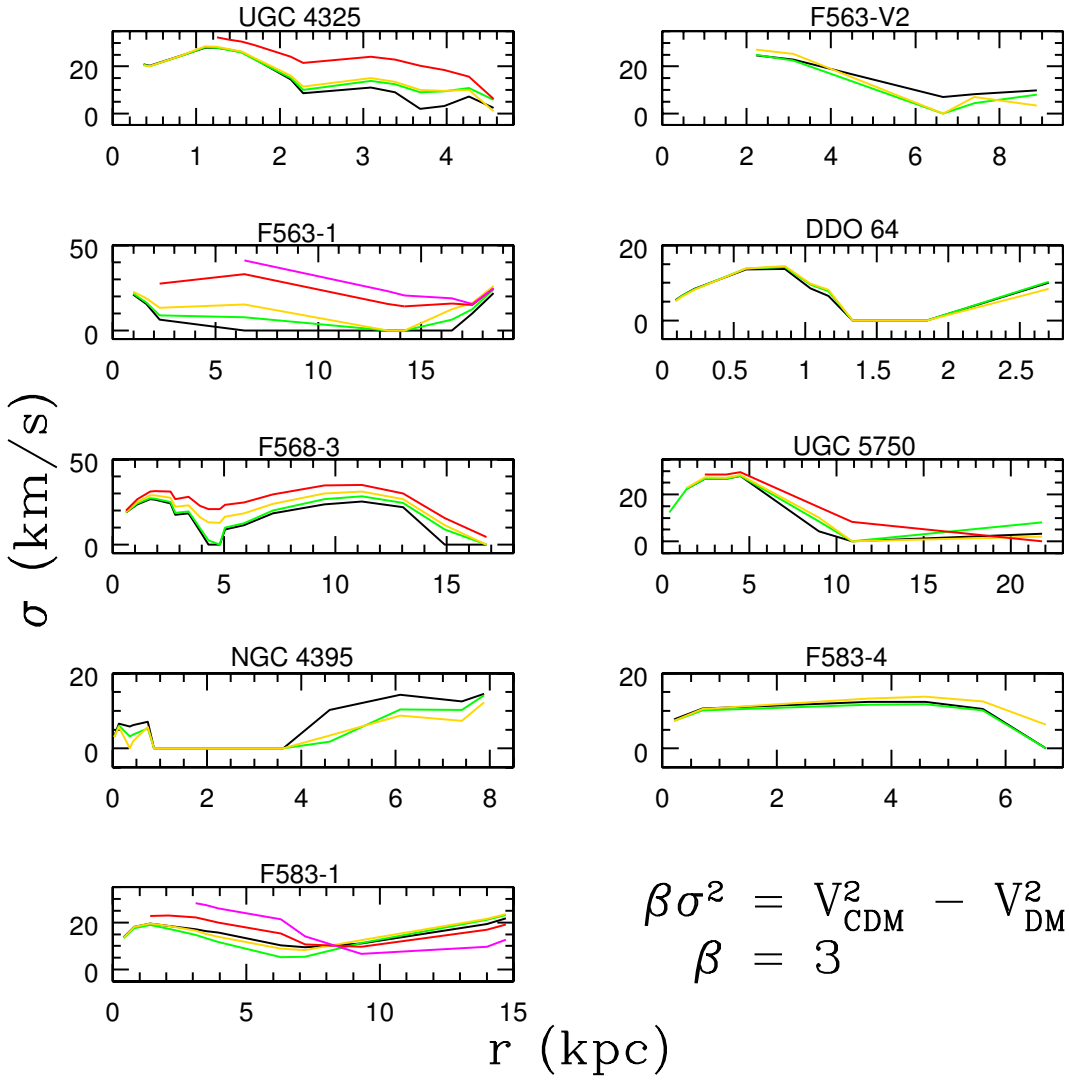

Figure 4.12: – The required noncircular motions, assuming an isotropic dispersion, to reconcile the difference between the NFW_{constr} velocity and the observed dark matter velocity.

be underestimated. This is the argument commonly given to explain the discrepancy between the NFW halo and the observations at small radii (e.g. Swaters et al. 2003a; van den Bosch & Swaters 2001). To determine the true circular velocity, the noncircular motions are added in quadrature to the observed velocities, $V^2_{circ} = V^2_{rot} + \beta\sigma^2$, usually

assuming an isotropic dispersion (β = 3).

We can invert Figure 4.11 and determine how large the noncircular motions must be in order to bring the observed dark matter velocity into agreement with the NFW_{constr} velocity. In Figure 4.12 we plot the required $\sigma(r)$, assuming an isotropic dispersion, for each galaxy. In general, most of the galaxies need about 20 km s^{-1} noncircular motions at inner radii for the data to be consistent with the expectations of CDM. This is roughly twice as large as the velocity dispersion in the DensePak data (see Table 2.3). It is also important to recognize the effect of stars not having zero mass. Instead of just having to convince ourselves that $\sim$20 km s^{-1} noncircular motions should be added to the data, we actually must be willing to consider noncircular motions an additional 5-10 km s^{-1} higher when $\Upsilon_* \neq 0$. In the next Chapter we model the NFW halo and noncircular motions, and Figure 4.12 provides us with testable predictions.

4.6 Summary

For a sample of LSB galaxies observed with DensePak, we have presented isothermal and NFW halo fits for four assumptions of the stellar mass-to-light ratio, Υ_*. We have tested the zero, minimal, popsynth, and maximum disk cases. We have found that as baryons become more important, the NFW halo becomes increasingly more difficult to fit to the data. The NFW halo and maximum disk are mutually exclusive. There is a substantial cusp mass excess near the centers of the galaxies with at least two times more mass expected in the cuspy CDM halo than is allowed by the data. Most galaxies in the sample require $\sim$20 km s^{-1} noncircular motions to reconcile the differences between ob-

servations and the NFW halo. Proper accounting of the baryons increases the discrepancy between the NFW halo and the data, and requires even larger noncircular motions to fix the problem.

Chapter 5

Modeling the NFW Potential

5.1 Overview

In this chapter we model the two-dimensional NFW potential to determine if, and under what conditions, the NFW halo appears consistent with observed galaxy data. We present mock DensePak velocity fields and rotation curves of axisymmetric and non-axisymmetric potentials. We find the characteristic NFW pinch of the isovelocity contours to be clearly visible in the mock DensePak observations of axisymmetric NFW potentials and that the NFW rotation curve is recoverable with a tilted-ring fitting program. We also find that the cusp mass excess in the observed galaxy data can be reduced with a non-axisymmetric NFW potential having a fixed axis ratio, however, the NFW pinch remains visible in the velocity field. More problematic is that a specific viewing angle is required: the observer's line-of-sight must be along the minor axis of the potential. In general, if halos are randomly oriented, one would expect to find enhancements to the rotation curve as well as the observed depression. Additionally, we explore a non-axisymmetric NFW potential with a radially varying axis ratio. We find that while a variable axis ratio tends to wash out the NFW pinch, it introduces a twist to the velocity field.

5.2 Motivation

The NFW halo has been difficult to reconcile with our observed galaxy data in a number of ways. We have found that the NFW fits to our DensePak rotation curves often have low concentrations. The NFW rotation curves commonly exhibit an over-under-over fitting trend. NFW halos with cosmologically consistent parameters (NFW_{constr}) have rotation curves that are higher than the observed DensePak rotation curves at small radii, and these halos also show a cusp mass excess at the centers of the galaxies. Additionally, the velocity field of an NFW halo shows a very distinctive pinching of the isovelocity contours (de Blok, Bosma, & McGaugh 2003) that is not seen in the DensePak velocity fields of the observed sample of galaxies (see Figure 5.1).

Our DensePak results are consistent with many previous long-slit and HI studies of LSB galaxies (e.g., BMR01; BB02; Swaters et al. 2003a) as well as similar DensePak studies by Simon et al. (2005). That different observational techniques (with different data reduction/analysis procedures and sources of error) lead to similar conclusions suggests that perhaps the discrepancy between NFW and the observations does not arise at the telescope or during the data analysis, but rather is due to an incorrect assumption about the specific form of the NFW halo potential. Our focus in this chapter is on modeling the NFW halo to determine if, and under what conditions, it appears consistent with the observed data. Starting with an axisymmetric NFW potential, how must it be modified (e.g., introduction of an asymmetry) in order to appear consistent with both the observed two-dimensional velocity field and the derived rotation curve? We construct an NFW halo and then "observe" it in the same way as we have observed our sample of galaxies with

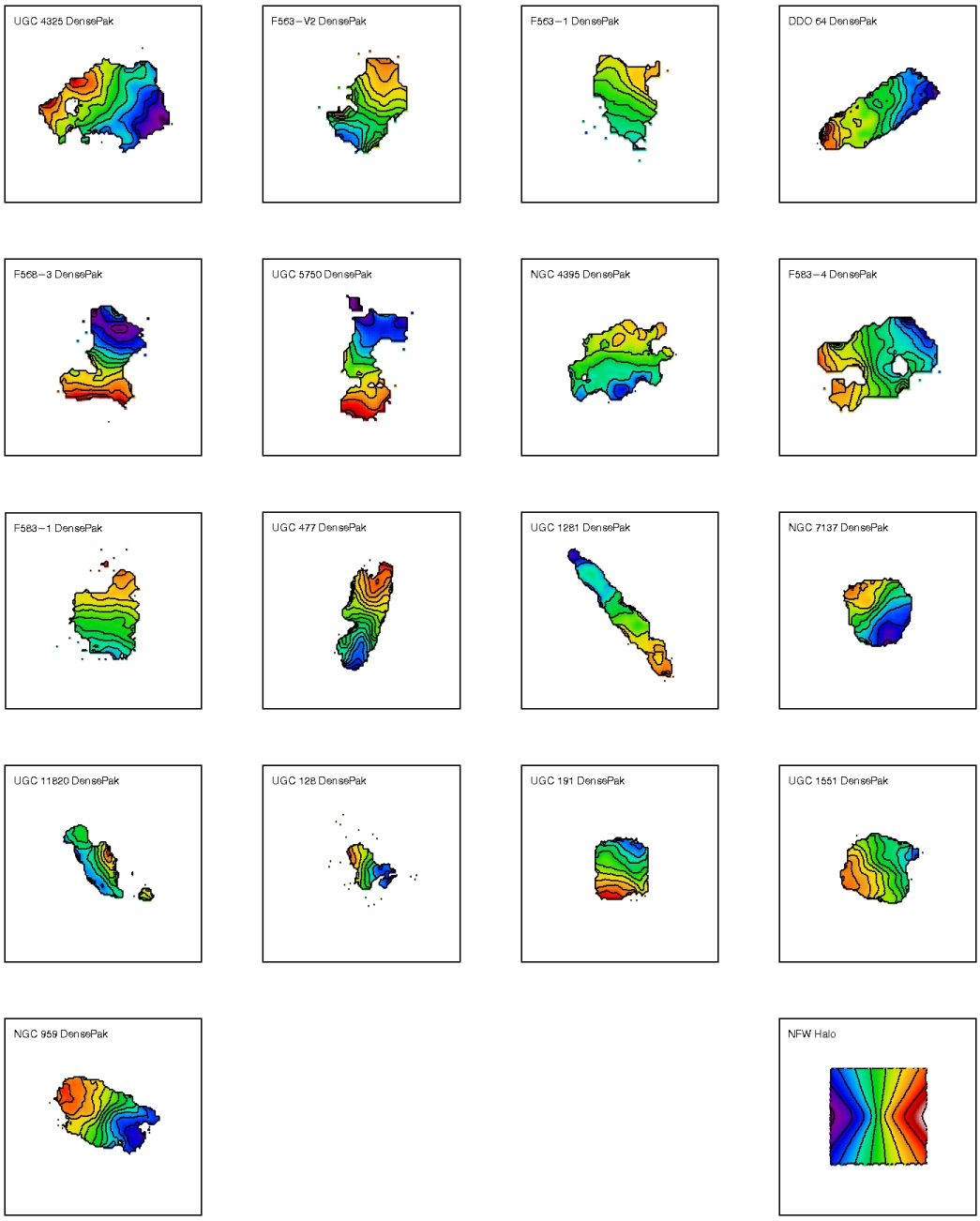

Figure 5.1: – DensePak velocity fields of observed galaxies. For comparison, in the lower right panel is the velocity field of an NFW halo with (c, V_{200}) = (8.6, 100 km s^{-1}) inclined at 60°. NOTE THE DISTINCTIVE PINCHING OF THE ISOVELOCITY CONTOURS WHICH IS CHARACTERISTIC OF NFW HALOS. Isovelocity contours are at 10 km s^{-1} intervals.

DensePak. We then compare the mock velocity field and the derived mock rotation curve to the real galaxy data.

We adopt a numerical approach to investigating non-axisymmetric halo potentials because once axisymmetry is broken, the data analysis becomes much more complicated. Noncircular motions and asymmetries are traditionally investigated by doing a Fourier decomposition of the velocity field. We have tried this approach, but it was not sufficiently well-constrained for these difficult LSB targets to give unique results. But we do find that useful constraints can still be extracted by simulating what is expected to be observed for various hypothesized halo potentials.

5.3 Description of Simulations

N-body simulations show that CDM halos of all sizes can be described by the NFW potential (Navarro, Frenk, & White 1996, 1997) and its variants (e.g., Diemand et al. 2005; Moore et al. 1999b; Navarro et al. 2004; Reed et al. 2003). These cuspy halo potentials show a steep rise in the mass density toward the center of the halo. Because the NFW potential is the least steeply rising, it serves as a lower limit on the slope of the density profile. If the NFW potential predicts a dark matter halo that is more massive than allowed by the observed galaxy data, then more steeply rising potentials are automatically excluded. It is for this reason that we choose to simulate the NFW halo.

Our goal is to compare mock DensePak velocity fields and rotation curves of NFW halos to observed DensePak velocity fields and rotation curves of LSB galaxies. To this

end, we developed a code[1] which does a fourth-order Runge-Kutta (RK4) test particle integration of points moving in a two-dimensional rigid analytic NFW potential. Specifically, the potential used is:

$$\Phi(R) = -\frac{GM_{200}\ln(1+\frac{R}{R_s})}{Rf(c)}, \tag{5.1}$$

where

$$R = \sqrt{x^2 + (y^2/q^2)}, \tag{5.2}$$

$$R_s = \frac{R_{200}}{c}, \tag{5.3}$$

and

$$f(c) = \ln(1+c) - \frac{c}{1+c}. \tag{5.4}$$

In these equations, M_{200} is the enclosed halo mass at radius R_{200}, q is the axis ratio ($q = y/x$), and c is the concentration of the halo ($c = R_{200}/R_s$). The halo parameters are set to those of the NFW_{constr} halo for each galaxy observed with DensePak. The simulated galaxy is an exponential disk of 10,000 test particles (100,000 test particles were used when simulating the nearby galaxies UGC 4325 and DDO 64). The test particles are placed randomly within the potential and given initial velocities with the velocity dispersion observed in the real galaxy. To wash out the numerical pattern noise of the initial conditions, we integrate for 50 half-mass rotation periods having 500 timesteps each. The simulated galaxy is given the disk scale length, spatial resolution, and inclination of the real galaxy. The simulated galaxy is then "observed" by DensePak. The number and alignment of the simulated DensePak pointings is roughly equivalent to the actual Dense-

[1]This code was written in collaboration with Professor Chris Mihos of Case Western Reserve University.

Table 5.1. Simulated NFW Halo Parameters

Galaxy	c	V_{200} km s^{-1}
UGC 4325	6.9	249
F563-V2	7.9	130
F563-1	8.4	101
DDO 64	9.2	62
F568-3	8.2	110
UGC 5750	9.1	67
F583-4	9.1	67
F583-1	8.7	83

Note. — NFW halo parameters for the simulated galaxies.

Pak pointings made on the real galaxy. The mock observations are then analyzed using ROTCUR.

5.4 Galaxy Modeling

In this section we present the mock DensePak velocity fields and rotation curves for NFW potentials of increasing complexity. The parameters of the NFW halos are the NFW_{constr} parameters for the zero disk case of each galaxy (see Table 5.1). We compare the simulations to the data to determine if it is possible to simultaneously match both the mock NFW velocity field and mock NFW rotation curve to the data.

5.4.1 Axisymmetric NFW Halos

The most obvious and simple starting point is to assume an axisymmetric halo potential. The axis ratio q is equal to 1 and the test particles move on circular orbits. This

straightforward potential will let us test three things. First, we can determine if DensePak is capable of detecting an NFW halo. Is the characteristic pinch of the NFW isovelocity contours seen in the simulated velocity field that DensePak observes? Second, we can determine if our data analysis procedure with ROTCUR is able to recover the NFW rotation curve from the simulated DensePak data. Lastly, we can compare the mock DensePak velocity field and rotation curve to the observed galaxy data to test whether or not the data are consistent with an axisymmetric NFW halo potential.

In Figure 5.2 we model the NFW_{constr} halo (c = 6.9) of UGC 4325 and observe the simulation with 5 pointings of the DensePak array. The observed mock DensePak velocity field clearly shows an hourglass-shaped pinching of the isovelocity contours. This demonstrates that the lack of pinching seen in the velocity fields of our observed sample of galaxies is not due to a failure of the instrument; DensePak *is* able to distinguish an axisymmetric NFW velocity field. Additionally, ROTCUR is able to extract the NFW rotation curve corresponding to the underlying NFW potential.

If DensePak observes a galaxy embedded in an axisymmetric NFW potential, the observed velocity field will appear pinched and a tilted-ring fitting program will recover the NFW rotation curve. That our sample of LSB galaxies observed with DensePak do not have pinched velocity fields nor have rotation curves consistent with those of the NFW_{constr} halos shows that if the underlying halo potential is NFW, it is not an axisymmetric NFW potential.

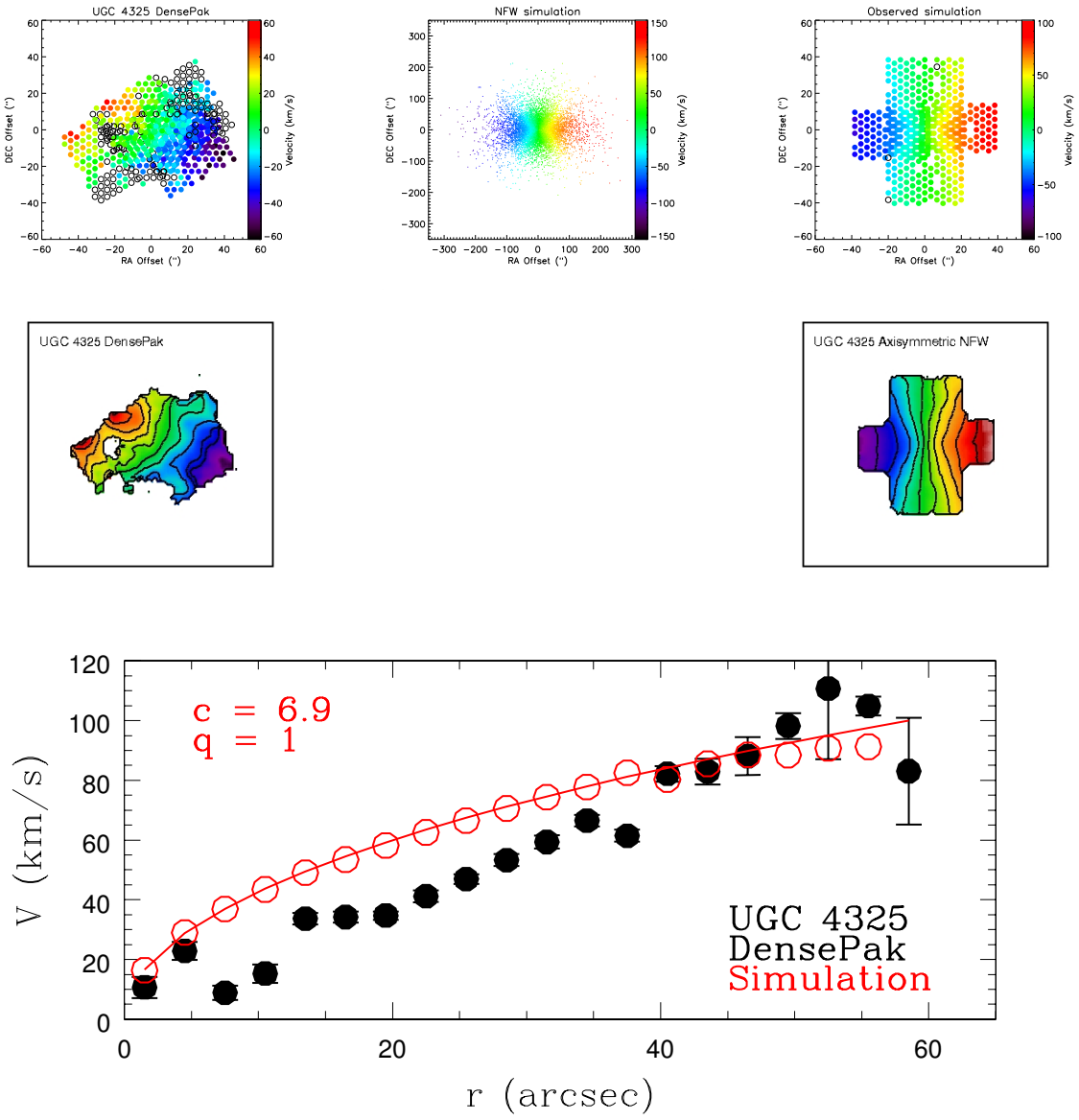

Figure 5.2: – *Left Column:* Observed DensePak velocity field of UGC 4325 plotted in raw fiber format (top) and smoothed with isovelocity contours at 10 km s^{-1} intervals (bottom). *Middle:* Simulated axisymmetric NFW halo with the parameters of the NFW_{constr} halo for UGC 4325. *Right Column:* Observed mock DensePak velocity field of the simulation plotted in raw fiber format (top) and smoothed with isovelocity contours at 10 km s^{-1} intervals (bottom). *Bottom:* Solid points are the observed DensePak rotation curve of UGC 4325. The solid red line is the NFW_{constr} rotation curve, and the open red circles are the rotation curve recovered from the mock DensePak velocity field.

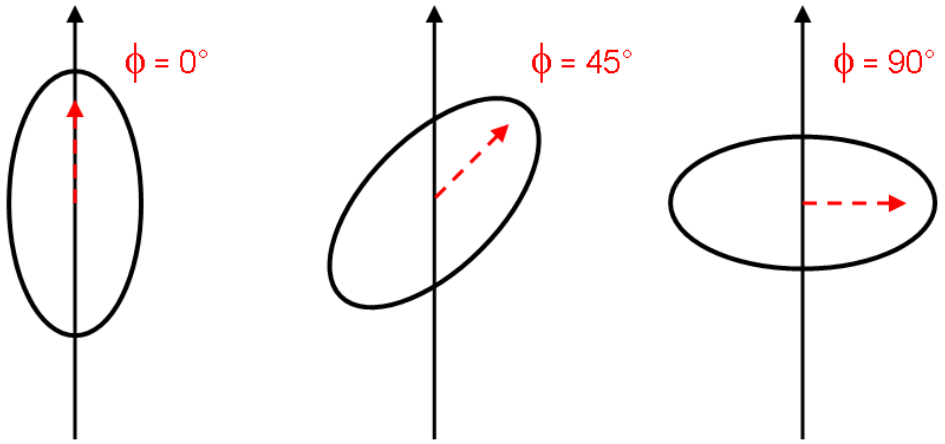

Figure 5.3: – Orientation (ϕ) of the elongated axis of the non-axisymmetric potential with respect to the observer's line-of-sight.

5.4.2 Non-axisymmetric NFW Halos: Fixed Axis Ratio

We next consider non-axisymmetric NFW potentials with axis ratios $q < 1$ that are constant with radius. We simulate halos with axis ratios q = 0.98, 0.96, 0.94, 0.92, 0.90, 0.88, 0.86, and 0.84. Because the test paticles are no longer moving on circular orbits, the observed mock DensePak velocity field and derived rotation curve are affected not only by the value of q, but also by the orientation (ϕ) of the potential's elongation with respect to the observer's line-of-sight (see Figure 5.3). For each value of q, the orientation of the potential is set to ϕ = 0°, 30°, 45°, 60°, 85°, 86°, 87°, 88°, 89°, and 90°.

The LSB galaxies we have observed with DensePak surely have some level of non-circular motions, but we have assumed circular motion when deriving the rotation curves with ROTCUR; we treat the mock observations the same way. The test particles are, by construction, no longer on circular orbits in these non-axisymmetric potentials, but because we did not correct for this in the real data, we do not correct for it in the mock observations. Any errors in the galaxy rotation curves which may have resulted from the assumption of circular motion will be reproduced in the rotation curves of the mock observations.

In Figure 5.4 we show the mock velocity fields of the NFW_{constr} (c = 6.9) halo of UGC 4325 with an axis ratio q = 0.86 and three values of ϕ. The potential is elongated along the observer's line-of-sight in the $\phi = 0^\circ$ case, whereas in the $\phi = 90^\circ$ case, the potential is elongated perpendicular to the observer's line-of-sight. For $0^\circ < \phi < 90^\circ$, the elongation is at an intermediate viewing orientation. In all mock velocity fields the characteristic NFW pinch is clearly visible. At the bottom of Figure 5.4 are the derived mock rotation curves for different values of ϕ along with the observed rotation curve of UGC 4325 and the rotation curve of the NFW_{constr} halo. The c = 6.9 NFW halo rotation curve is recovered if $\phi \approx 60^\circ$. If $\phi < 60^\circ$, the derived mock rotation curves are higher than the NFW_{constr} rotation curve and one would mistakenly infer too high of a concentration for the NFW halo. These combinations of (q, ϕ) produce results that move in the wrong direction for reconciling the differences between NFW and the observations. If $\phi > 60^\circ$, however, the opposite effect is seen, and the inferred mock rotation curve is lower than the rotation curve of the intrinsic NFW halo. At $\phi \approx 90^\circ$ the derived mock rotation curve of the non-axisymmetric NFW halo moves in a favorable direction for the NFW halo and

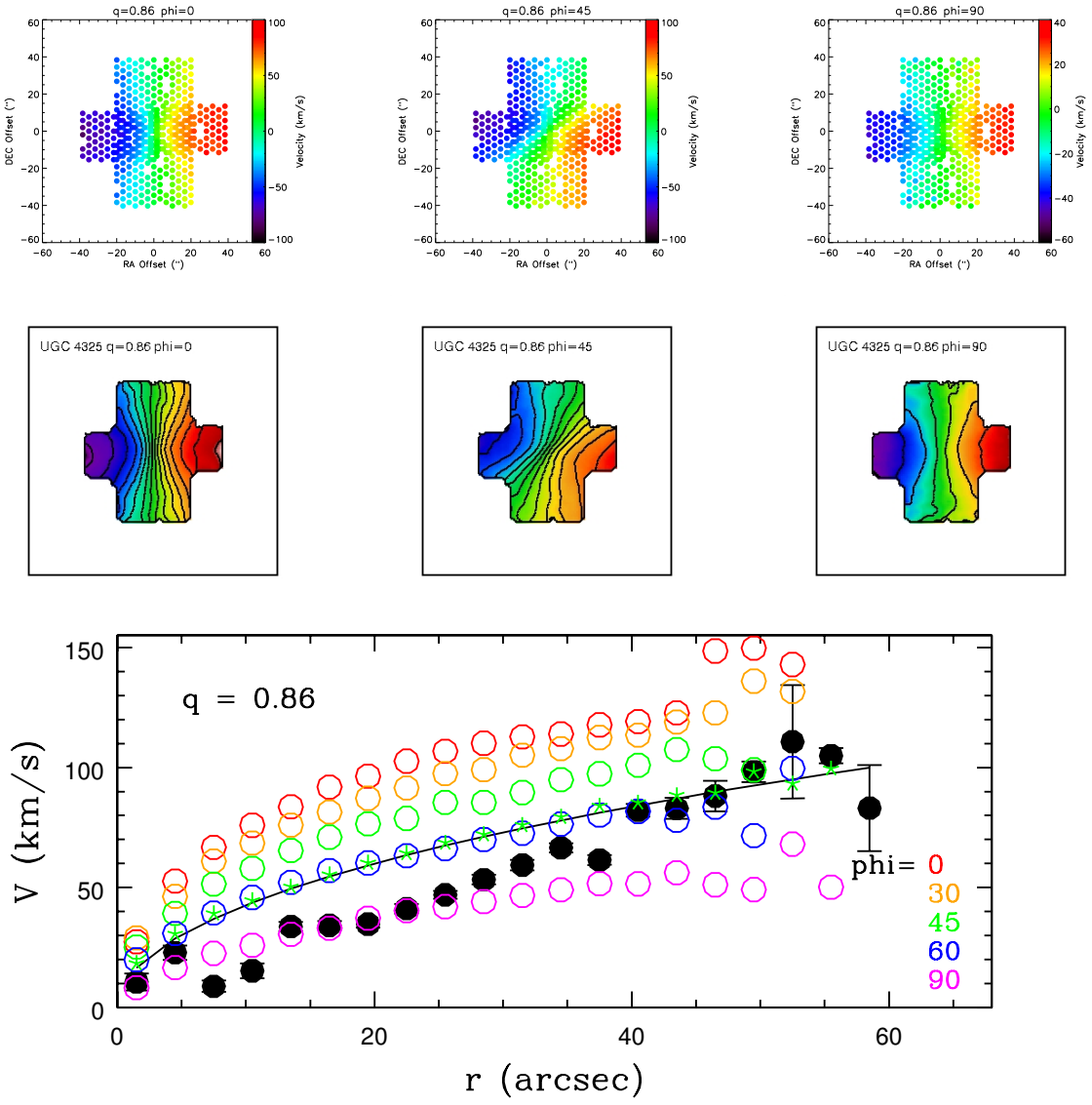

Figure 5.4: – *Top:* Observed mock DensePak velocity fields of the NFW$_{constr}$ halo for UGC 4325 with an axis ratio q=0.86 for three different viewing orientations. In the ϕ=0° orientation, the potential is elongated along the observer's line-of-sight; in the ϕ=90° orientation, the potential is elongated perpendicular to the observer's line-of-sight. The smoothed velocity fields are shown with isovelocity contours at 10 km s^{-1} intervals and the characteristic NFW pinch is clearly visible. *Bottom:* The open circles are the mock rotation curves for q=0.86 and different values of ϕ. The stars are the mock rotation curve of (q, ϕ) = (0.96, 45°).

appears consistent with a number of the points in the observed UGC 4325 rotation curve.

Given the behavior of the simulated rotation curves in Figure 5.4, one should expect to see higher than nominal concentrations as well as lower than expected, but this is not what is observed in long-slit data (McGaugh, Rubin, & de Blok 2001; de Blok & Bosma 2002). LSB and NFW rotation curves always differ in the sense that the observed rotation curve velocities must increase so that the data match the models, or equivalently, the NFW rotation curve velocities must decrease so the models match the data. LSB rotation curves which are higher than NFW rotation curves are not found.

There is a trade-off between q and ϕ such that different combinations of the two parameters can produce similar rotation curves. As shown in Figure 5.4, the mock rotation curve for a c = 6.9 NFW halo with (q, ϕ) = (0.86, 60°) is consistent with the mock rotation curve of a c = 6.9 NFW halo with (q, ϕ) = (0.96, 45°). In the next section, we explore what combination of (q, ϕ) minimizes the differences between the NFW halo and the DensePak galaxy observations.

5.4.2.1 Minimizing the Cusp Mass Excess with q and ϕ

In Chapter 4.5.1 and 4.5.2 we showed that there is a substantial cusp mass excess near the centers of the galaxies when the NFW_{constr} halo is used to describe the dark matter halo. In this section, we are interested in determining what combination of (q, ϕ) will minimize the cusp mass excess for each galaxy presented in Chapter 4.5.1. We compare the mock rotation curve for each combination of (q, ϕ) to the observed DensePak rotation curve out to the radius where the cusp mass excess in the zero disk case is ~ 0.

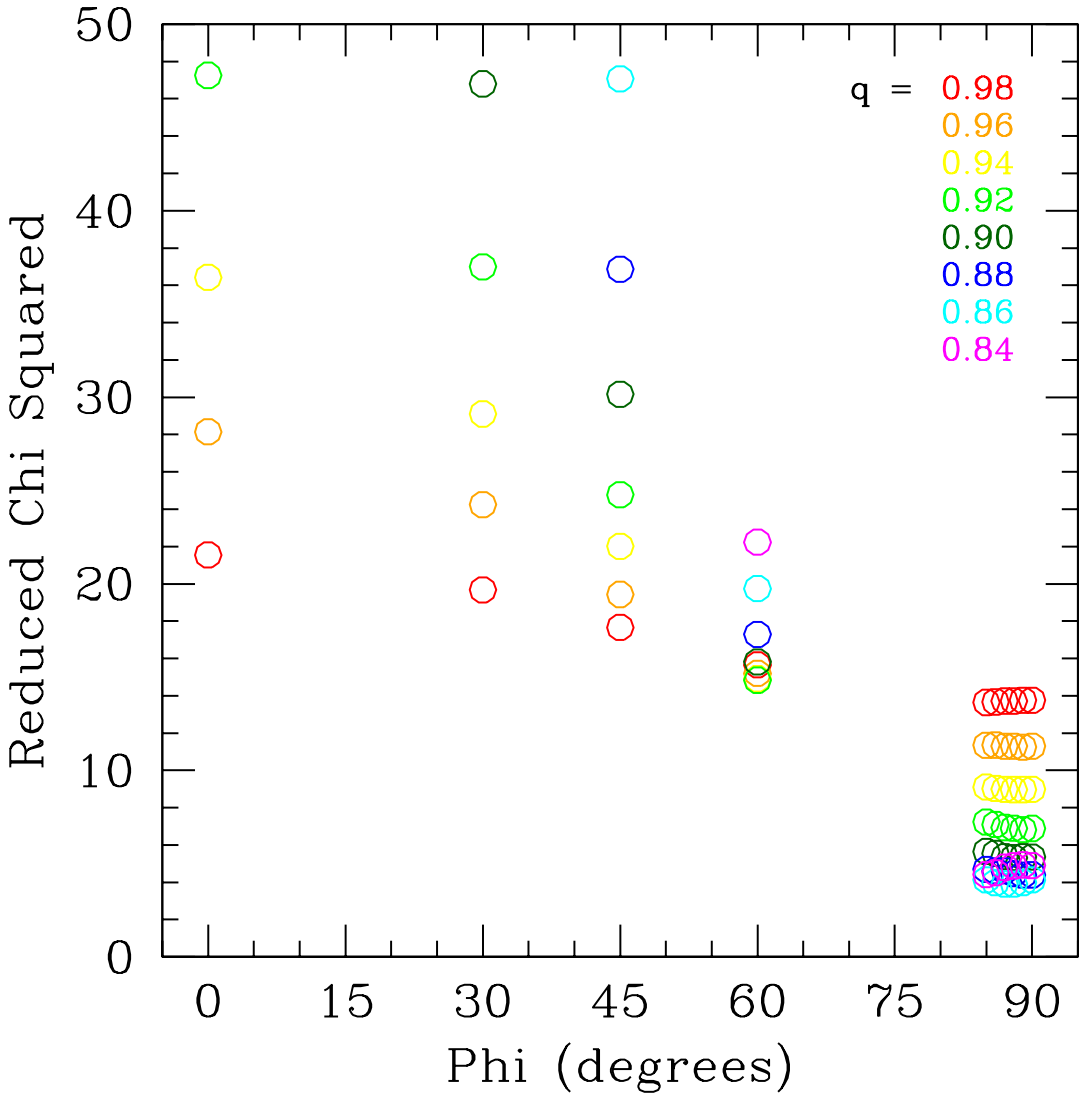

Figure 5.5: – Finding the combination of q and ϕ which maximizes the agreement between the mock rotation curve of the non-axisymmetric NFW potential and the observed DensePak rotation curve of UGC 4325. The rotation curves are compared out to $r \sim 40''$, or ~ 2 kpc, the radius at which the cusp mass excess is ~ 0. The cusp mass excess is reduced as $\phi \rightarrow 90°$, regardless of q. The NFW halo with (q, ϕ) = (0.86, 88°) is the closest match to the real data in this particular case.

In Figure 5.5 we show the results for UGC 4325. Regardless of how elongated the NFW potential is, there is marked reduction of the cusp mass excess as $\phi \rightarrow 90°$. The cusp mass excess is minimized IN THIS CASE when (q, ϕ) = (0.86, 88°). The (q, ϕ) = (0.86,

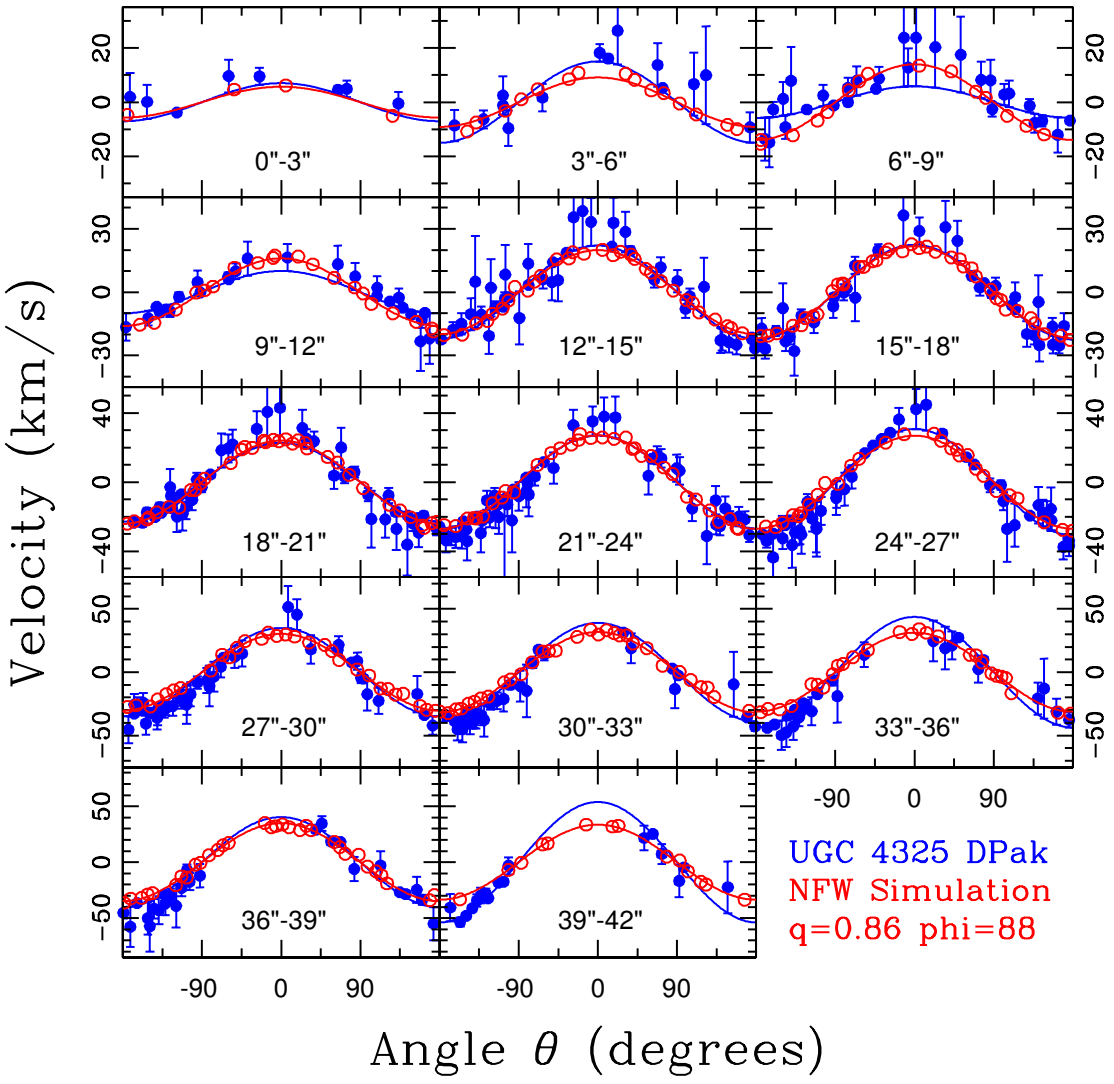

Figure 5.6: – The (0.86, 88°) simulation results (red) over-plotted with the observed UGC 4325 data (blue). The simulation and data match well between $\sim 12''$ - $30''$.

88°) simulation results are over-plotted with the observed data for UGC 4325 in Figure 5.6 to show how the two datasets compare on a ring-by-ring basis. The simulation and data match particularly well between $\sim 12''$ - $30''$. The differences between the simulation and data in the other rings, including those beyond $\sim 42''$ where the cusp mass excess is ~ 0, may possibly be reduced by invoking a non-axisymmetry that varies with radius

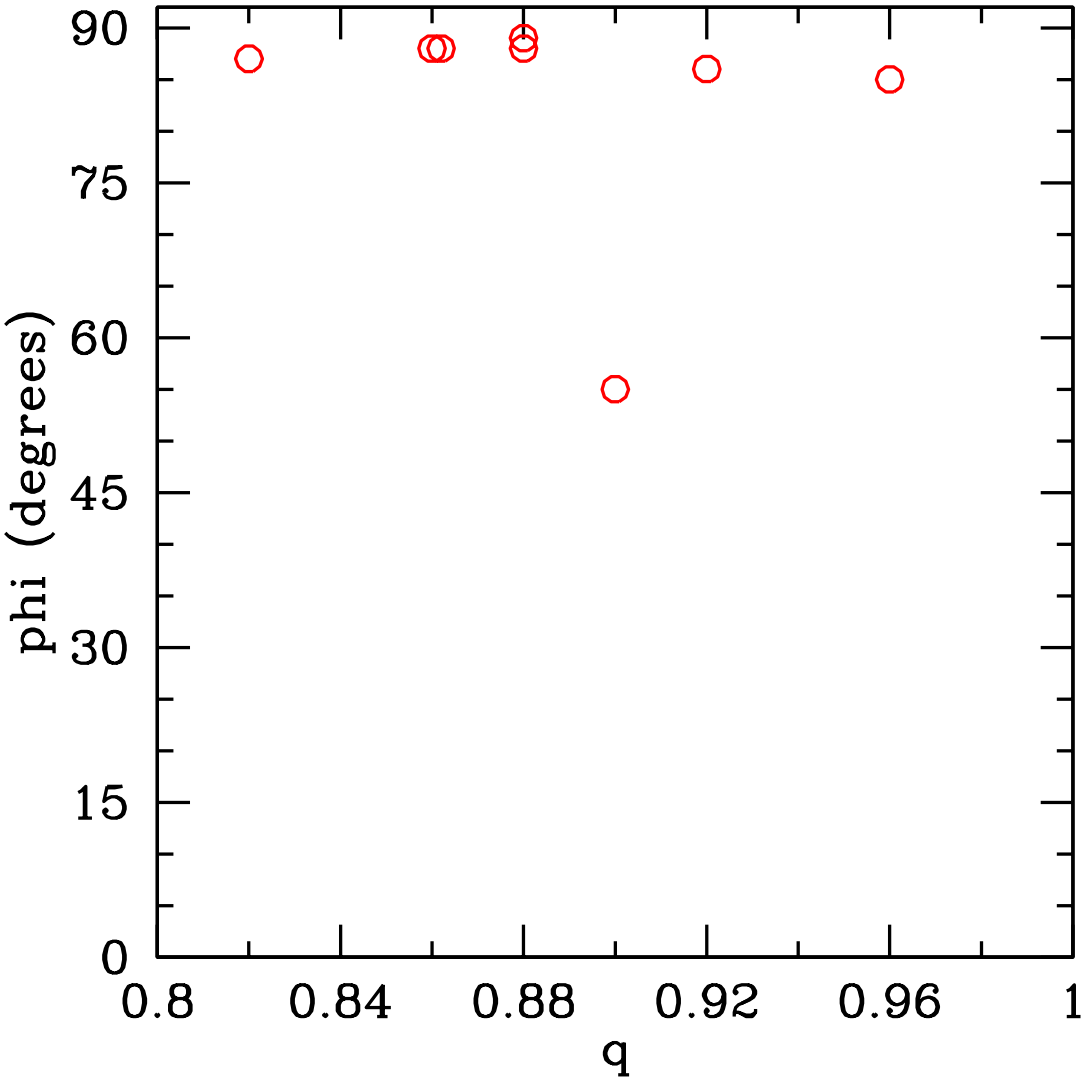

Figure 5.7: – The q and ϕ which minimize the cusp mass excess for each galaxy in the sample. The mock and observed rotation curves are compared out to the radius at which the cusp mass excess is ~ 0. The cusp mass excess is minimized when $\phi \rightarrow 90^{\circ}$ for all galaxies except F563-V2. F563-V2 has a bar that is approximately aligned with the elongated axis of the potential when $\phi \sim 55^{\circ}$.

(Hayashi, Navarro, & Springel 2007).

We determine the (q, ϕ) which minimizes the cusp mass excess for each galaxy in the sample and show the results in Figure 5.7. NGC 4395 is excluded from this analysis

because its rotation curve is consistent with an NFW halo and there is not a significant cusp mass excess. As shown in Figure 5.7, the cusp mass excess is minimized when $\phi \sim 90^\circ$ for all of the galaxies except for one. F563-V2 is the outlying galaxy and requires $\phi \sim 55^\circ$. There appears to be a central bar-like lump (see Figure 2.2) in F563-V2. The bar's position angle with respect to the major axis of the galaxy is approximately aligned with the elongated axis of the NFW potential when $\phi \sim 55^\circ$. It is possible that it is the bar, not the halo, that is responsible for this preferred angle (see also Spekkens & Sellwood 2007).

The simulations show that elongated NFW potentials must point perpendicular to our line-of-sight. This required ϕ is completely inconsistent with a random distribution of halo orientations on the sky. A non-axisymmetric potential may be able to bring the NFW rotation curve into agreement with the observed data FOR INDIVIDUAL GALAXIES, but IN GENERAL, very peculiar, observer-dependent conditions must occur.

5.4.2.2 Erasing the NFW Pinch with q and ϕ

It may be possible to "fix" the NFW rotation curve with a non-axisymmetric potential (if one can ignore the statistical argument against the required ϕ), but the velocity fields must also be "fixed." The NFW pinch must be erased from the observed mock DensePak velocity fields. Figure 5.8 shows the observed DensePak velocity fields for four galaxies along with the observed mock DensePak velocity fields for the best-fitting (q, ϕ). In all four mock velocity fields (as well as the additional four that are not shown), the NFW pinch remains clearly visible despite the noncircular motions caused by the

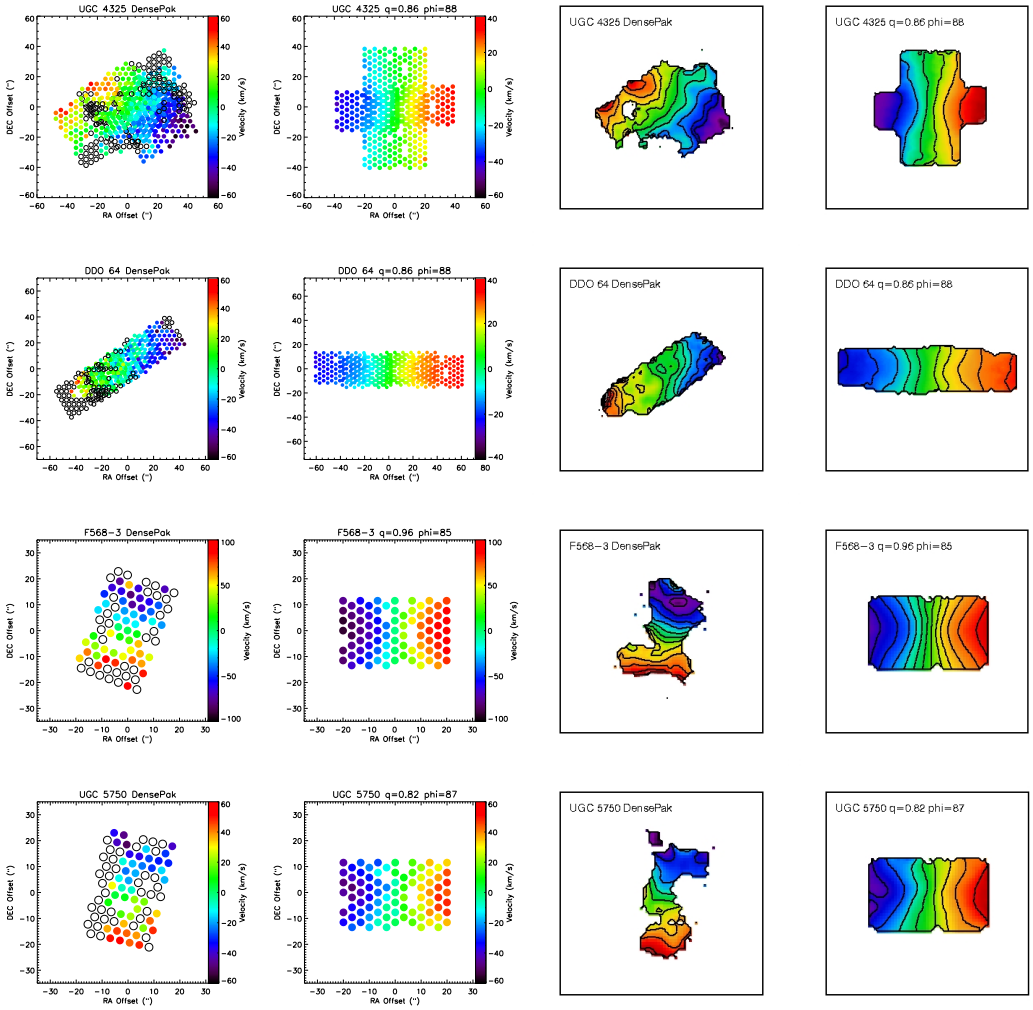

Figure 5.8: – *First and third columns:* Observed DensePak velocity fields (fiber format and smoothed) of UGC 4325, DDO 64, F568-3 and UGC 5750. *Second and fourth columns:* Mock observed DensePak velocity fields (fiber format and smoothed) of the non-axisymmetric NFW potentials with constant axis ratios. The characteristic NFW pinch remains clearly visible in the mock velocity fields.

non-axisymmetric potential. If an NFW halo is present, the pinch should be clearly visible in well-resolved, nearby galaxies such as UGC 4325 and DDO 64 where there are multiple DensePak pointings and abundant diffuse Hα emission. It is also easy to see the pinch in the velocity fields of the more distant and less well-resolved galaxies like

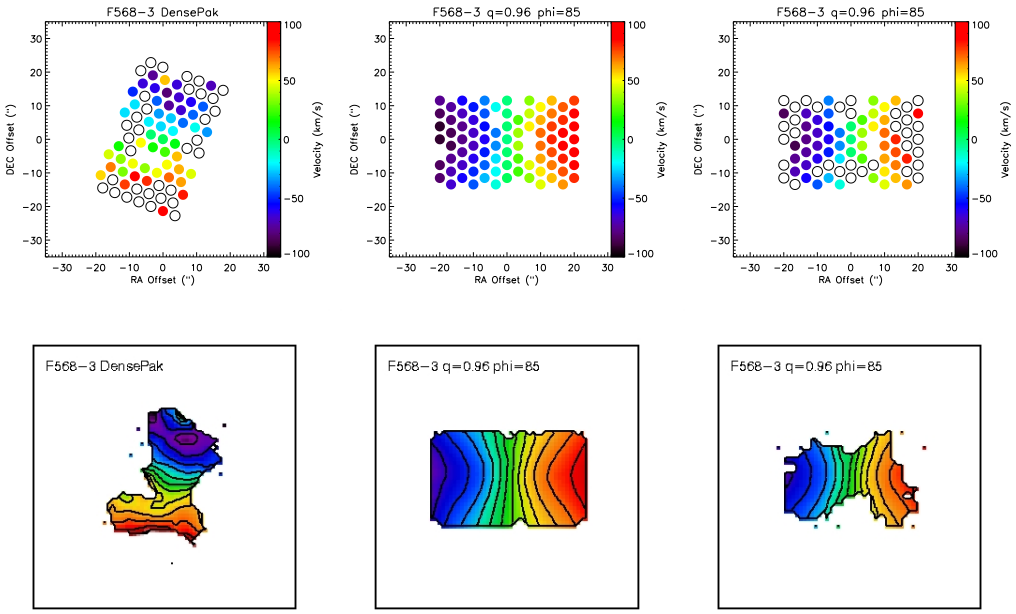

Figure 5.9: – *Left column:* Observed DensePak velocity field of F568-3. *Middle column:* Mock velocity field of F568-3. *Right column:* Mock velocity field of F568-3 with fiber detections removed to allow for direct comparison with the observed DensePak velocity field. The NFW pinch is easy to see when every fiber has a detection, but is not as immediately obvious when there is sparse emission. Isovelocity contours are at 10 km s^{-1} intervals in the smoothed versions of the velocity fields.

F568-3 and UGC 5750 when there is enough Hα emission. In Figure 5.9 we use F568-3 to demonstrate the importance of diffuse emission so that there are detections in as many fibers as possible. If we remove from the mock velocity field the fibers without detections in the observed velocity field, the NFW pinch, while still observed, is not as immediately obvious.

Non-axisymmetric NFW potentials with a fixed axis ratio are able to reconcile the differences between the expectations of CDM and the observed galaxy rotation curves, as well as eliminate the cusp mass excess. However, to do so, the elongated axis of the NFW

potential must always be aligned almost perpendicular to the observer's line-of-sight. There is no reason why all dark matter halos in the universe should have this particular orientation. Additionally, the noncircular motions induced by the non-axisymmetric potential are large enough to "fix" the mock rotation curves, but are not big enough to erase the characteristic NFW pinch from the velocity fields. The non-axisymmetric NFW potentials that we have simulated in this section do not provide a solution to the differences between CDM and the data.

5.4.3 Non-axisymmetric NFW Halos: Variable Axis Ratio

We have found that if the two-dimensional axisymmetric NFW potential is modified to be non-axisymmetric with a constant axis ratio, the NFW and observed galaxy rotation curves can be reconciled, but the velocity fields remain distinctly different. If we further modify the potential with a radially varying axis ratio, *q(r)*, can we reconcile both the rotation curves and the velocity fields?

Hayashi, Navarro, & Springel (2007) assert that galaxy-sized CDM halos are triaxial with radially varying axis ratios. They find the halo potential to be highly elongated near the center ((b/a) $\rightarrow$ 0.78 and (c/a) $\rightarrow$ 0.72) and increasingly more spherical at large radii (see Figure 5.10). In this section we simulate the NFW halo using their approximation of *q(r)*

$$\log q(r) = \alpha[\tanh(\gamma \log \frac{r}{r_\alpha}) - 1] \tag{5.5}$$

with (α, γ, r_α) = (0.06, 1.4, 1.2 R_s). These parameters correspond to a potential with a rapidly changing asymmetry and a central axis ratio $q(0) \sim 0.78$.

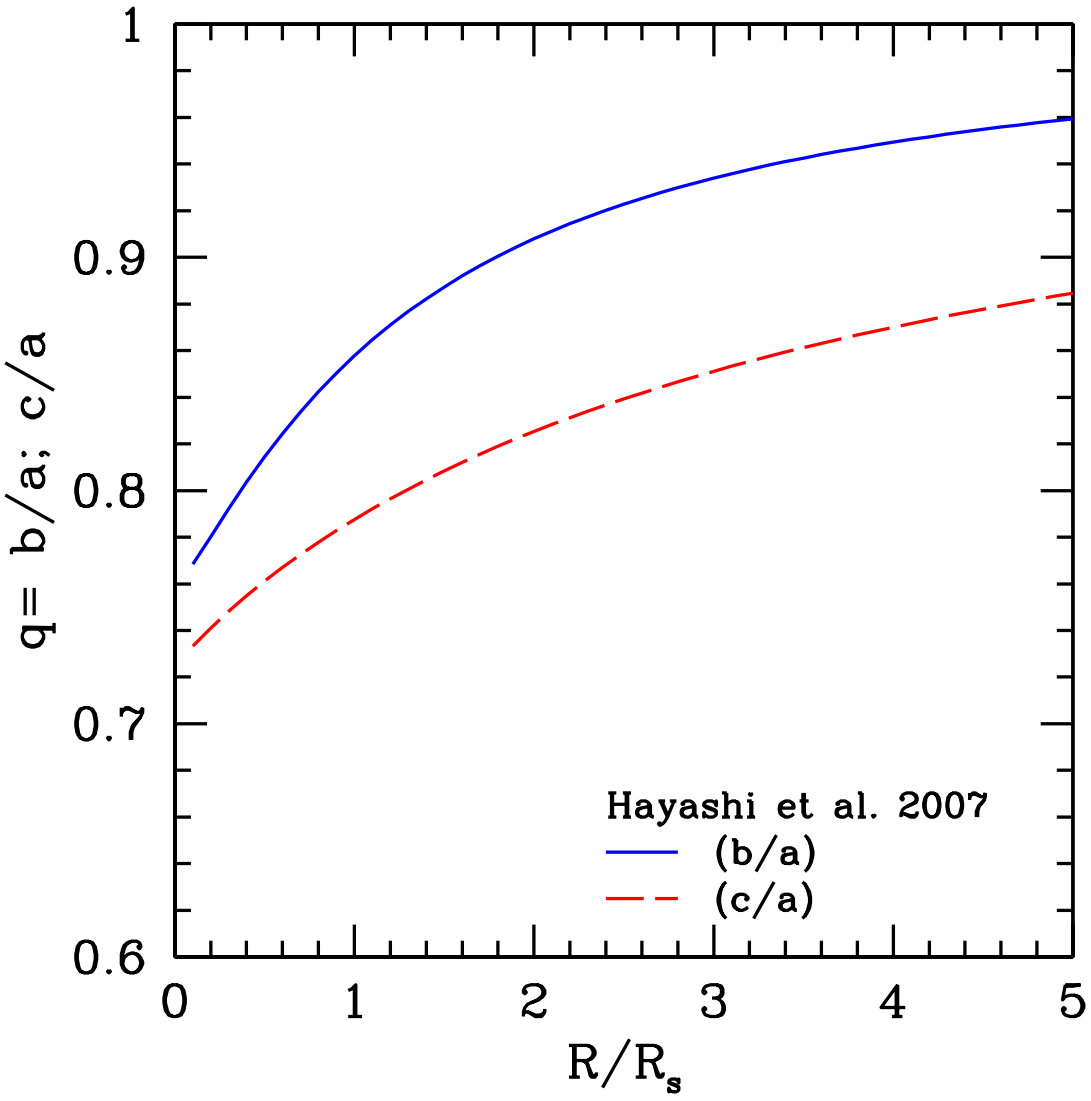

Figure 5.10: – Radially varying axis ratios of triaxial CDM halos (Hayashi, Navarro, & Springel 2007). The solid blue line indicates the function used in our simulations of the NFW potential. The simulated DensePak data are typically within 1 R_s.

In Figure 5.11 we show the resulting mock DensePak velocity fields for F568-3 and F583-1. A variable axis ratio is able to wash out the NFW pinch from the velocity fields, but in doing so, it introduces a twist to the isovelocity contours. The major and minor kinematic axes are not perpendicular in these velocity fields, a clear indication that the

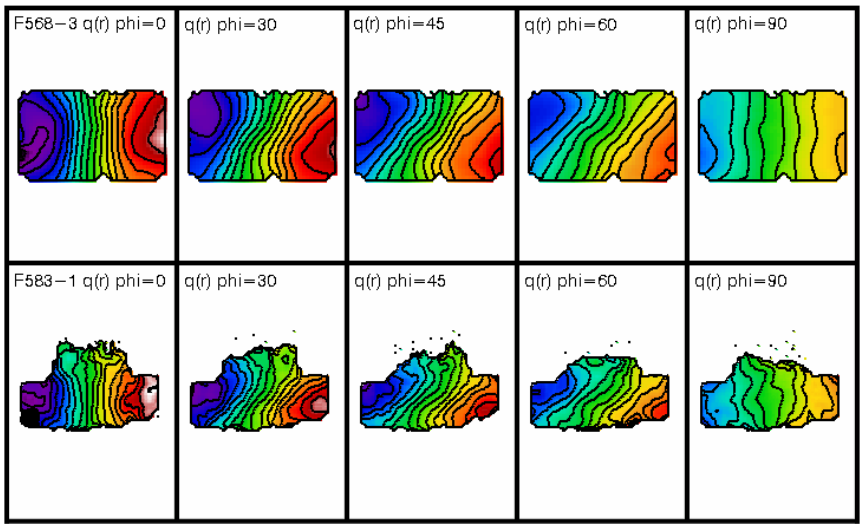

Figure 5.11: – Mock velocity fields of F568-3 (top) and F583-1 (bottom) resulting from a non-axisymmetric NFW potential with a radially varying axis ratio. The NFW pinch is erased, but is replaced with a bar-like twist.

test particles are moving on elliptical orbits. The position angle of the major axis is not constant with radius and is unconstrainable in the mock DensePak data. A velocity field with a bar-like signature requires a much more complicated analysis to properly treat the changing position angle and noncircular orbits. Because we cannot constrain the position angle, we do not determine rotation curves for these velocity fields, or test if there is a preferred ϕ for the *q(r)* potential.

While it is encouraging that a variable axis ratio is able to erase the NFW signature in the velocity field, such a potential introduces several extra parameters and uncertainties

that it makes it difficult to test. For instance, not only must one consider the viewing orientation, ϕ, and a variable position angle when comparing the simulations to the observed data, but also the parameters of the NFW halo being modeled. The *q(r)* determined by Hayashi, Navarro, & Springel (2007) depends on the parameters of the NFW halo, specifically R_s. It is possible to improve the fit to the data by using the (c, V_{200}) degeneracy to tweak the halo parameters so that *q(r)* changes a little differently.

The analysis of an NFW potential with a variable axis ratio is sufficiently complex that if one is to do it right, it should be done in three dimensions with interacting particles. If having a highly elongated potential is key to "fixing" the NFW velocity field and rotation curve, then adiabatic contraction should also be included, as it will round out the inner halo potential (Dubinski 1994). Adiabatic contraction also has the effect of increasing the dark matter density of the halo over its initial value and serves to worsen the concentration problem (e.g., Gnedin et al. 2004; Sellwood & McGaugh 2005). There is clearly no simple modification of the axisymmetric NFW potential that reconciles both the velocity field and rotation curve, but a variable axis ratio seems to warrant further exploration.

5.5 Discussion

Rotation curves of LSB galaxies have long posed a problem for CDM. They consistently show a preference for halos with nearly constant density cores. Rather than discard or revise a theory that seems to work well only on large scales, systematic errors are often cited as ways to wiggle out of the problem on small scales. For instance, rotation

curves derived from HI velocity fields that had poor NFW fits were questioned because of concerns of beam smearing; in only a few galaxies did this turn out to be the case (e.g., McGaugh, Rubin, & de Blok 2001; de Blok, McGaugh, & Rubin 2001). Conclusions from long-slit rotation curve studies have also been met with skepticism over concerns of slit misplacement and noncircular motions (e.g., Rhee et al. 2004; Swaters et al. 2003a). These concerns seem to often be exaggerated (e.g., Kuzio de Naray et al. 2005; de Blok, Bosma, & McGaugh (2003); but see Swaters et al. (2003)). Observing programs designed to obtain high resolution Hα velocity fields target the centers of LSB galaxies and find the data to typically probe the regime of solid-body rotation (Kuzio de Naray et al. 2006). Because the velocity field is solid-body, it is difficult for a tilted-ring fitting program to fix the center, position angle and inclination of the galaxy. Without the symmetry provided by a rotation curve that turns over and flattens out, the data are free to move about in *x*-*y*-*v* space. This has led to claims that the derived rotation curves are systematically uncertain and can be consistent with NFW rotation curves (Swaters et al. 2003a). However, we have shown in this chapter that the NFW potential never produces a solid-body velocity field. The pinch of the NFW isovelocity contours clearly stands out. In the case of a varying axis ratio where a twist replaces the pinch, the velocity field is still not purely solid-body. While it is true that there are observed velocity fields that show twists similar to those produced by a variable axis ratio, it is also true, and more important to recognize, the frequent observations of solid-body velocity fields and rotation curves of LSB and dwarf galaxies stand in stark contrast to the nature of the NFW halo.

5.6 Conclusions

In this chapter we have simulated the two-dimensional NFW halo and tested several modifications to the potential in an attempt to simultaneously reconcile both the NFW velocity field and rotation curve with observed galaxy data. We have found that it is difficult to make the cuspy NFW halo appear consistent with core-like data while keeping to a minimum extra parameters and degrees of freedom. The axisymmetric NFW potential is inconsistent with both the observed velocity fields and rotation curves of our sample of galaxies. The characteristic NFW pinch is visible in the mock velocity fields, and the NFW rotation curve is recovered by ROTCUR. We have also found that a non-axisymmetric NFW potential with a constant axis ratio is able to "fix" the rotation curve, with a caveat, but not the velocity field. The cusp mass excess in the observed galaxy data is reduced with such a potential, but the elongated axis of the potential must always be oriented perpendicular to the observer's line-of-sight. While successful at modifying the rotation curve, the magnitude of the noncircular motions of this elongated potential is unable to erase the NFW pinch from the mock velocity fields. A non-axisymmetric potential with a radially varying axis ratio has also been explored and found to be able to wash out the NFW pinch at the expense of creating a twisted velocity field having the signature of a bar.

The next step is to create simulations of increasing complexity that make the modeled systems as realistic as possible (e.g., three dimensions, interacting particles). While numerically difficult, physical processes involved in galaxy formation, such as adiabatic contraction, should be included. Though these future simulations will have many more

uncertainties than the simulations of this chapter, having high-resolution Hα velocity fields of galaxies will help to keep them grounded in reality.

Chapter 6

Conclusions

6.1 Results

This dissertation set out to investigate the problems of CDM on small scales, in particular the cusp-core problem. We have observed a large sample of dark matter-dominated galaxies and obtained high-resolution Hα velocity fields of their central regions. We have derived rotation curves from the velocity fields and have fit the dark matter halos with both cuspy and cored halo potentials under several assumptions about the baryons. We have compared our results to the results of previous long-slit and HI studies. We have also modeled the NFW potential to see if it is possible to reconcile both the NFW velocity field and rotation curve with observed galaxy data. We can now provide answers for the four sets of questions posed in Chapter 1.4.2.

> ***Question 1:*** Are galaxy rotation curves derived from well-resolved optical velocity fields more consistent with the cuspy NFW halos predicted by CDM or by cored isothermal halos?
>
> ***Short answer:*** The data prefer cored halos.

We come to this conclusion for several reasons. Halo fits made in the limit of minimum disk, where the velocity contribution to the rotation curves from the baryons is

ignored, give the NFW halo the best opportunity to fit the data. Under this assumption, we have found that for the majority of the galaxies, NFW halo fits either could not be made or the implied concentrations were too low for ΛCDM. Of the 17 galaxies with DensePak rotation curves, 13 are best described by the isothermal halo, one appears consistent with the NFW halo, and three do not show a clear preference for either halo type. We made two types of NFW fits to the data: NFW_{free} and NFW_{constr}. The NFW_{free} fit imposes no constraints on the halo parameters, whereas the NFW_{constr} fit was constructed to agree with cosmology. No NFW_{free} fit could be made to seven of the galaxies. Of these seven, the four galaxies which also have NFW_{constr} fits are significantly better fit by the isothermal halo than the NFW_{constr} halo. The NFW_{constr} halos overpredict the velocity at all radii interior to where they were forced to match the observed velocity. NFW_{free} fits were able to be made to the remaining 10 galaxies. Of these 10, half had concentrations consistent with ΛCDM. Given the expected scatter in concentration values, three(two) galaxies had NFW_{free} fits with concentrations lower(higher) than nominal. The concentrations derived in these fits are upper limits and are pushed even lower when baryons are considered. In addition, the shape of the NFW_{free} rotation curves were often found to be inconsistent with the shape of the galaxy rotation curves: an over-under-over fitting trend was commonly observed. The NFW halo overpredicts the velocities at small radii then underpredicts the velocities at intermediate radii and then again overpredicts the velocities at large radii.

In Chapter 4: Mass Models we found the problems for the NFW halo to worsen. As we considered scenarios in which the velocity contribution from the baryons became progressively more important, the NFW halo was shown to become increasingly more

inconsistent with the observations. With less room available for dark matter at the centers of the galaxies, the centrally concentrated NFW halo became extremely difficult to fit to the data. In fact, the maximum disk case and the NFW halo were shown to be mutually exclusive. We also found that the NFW halo predicts a substantial cusp mass excess near the centers of the galaxies. Ignoring the baryons, CDM predicts dark matter halos that are at least two times more massive than the data allow. The ratio of predicted to observed dark matter increases as baryons become more important.

> ***Question 2:*** How do these new rotation curves compare to rotation curves from previous long-slit and HI studies? How do the NFW halo fits compare? Have systematic effects significantly impacted the interpretation of these previous data?
>
> ***Short answer:*** The majority of DensePak rotation curves and halo fits are broadly consistent with published results of long-slit and HI studies. That the independent data sets agree suggests that systematic effects are not as severe as often suggested.

Eleven of our 17 galaxies have published long-slit and/or HI rotation curves. In Chapters 2 and 3 we plotted those data with the new DensePak rotation curves and found good overall agreement between the data sets. The DensePak rotation curves are broadly consistent with long-slit rotation curves in all cases (9 galaxies). There are only two galaxies in which the rotation curves differ, and even then it is only over a very limited radial range. Of the nine galaxies having HI data, six show good overall agreement between the rotation curves. Both the DensePak and long-slit data for two galaxies are slightly higher

than the HI data, and in one case, the HI rotation curve is higher than the optical data. The HI data for these three galaxies may be affected by beam smearing (or overcorrection for beam smearing in the case of the high HI rotation curve), although it is possible this is the intrinsic HI distribution. The DensePak rotation curves confirm the slowly rising rotation curves derived from long-slit and HI data. Slit misplacement and beam smearing seem not to be responsible for the gradual rise of these rotation curves; LSB galaxies really do not have steeply rising rotation curves.

These systematic effects have also not adversely influenced the halo fits, as has been suggested. We found that there is gross agreement between the DensePak halo parameters (both NFW and isothermal fits) and previous long-slit and HI halo parameters. While the addition of the DensePak data does not significantly change the fits, it is able to decrease the errors on the halo parameters by about a factor of 2 in the minimum disk case.

> ***Question 3:*** If the NFW halo is inconsistent with the data, what level of noncircular motions are required to resolve this discrepancy, and are those noncircular motions consistent with constraints provided by the data?
>
> ***Short answer:*** Noncircular motions on the order of 20 km s^{-1} are needed to reconcile the observed galaxy rotation curves with the expected NFW rotation curves. Noncircular motions of this magnitude are unsupported by the DensePak data.

In Chapter 4 we determined how large noncircular motions must be to bring the observed dark matter velocity into agreement with the expectations of CDM. We found that in general the inner regions of galaxies require $\sim$ 20 km s^{-1} noncircular motions for

the data to match the NFW_{constr} halo. This level of noncircular motion is inconsistent with constraints provided by the DensePak data: these noncircular motions are roughly twice as large as the velocity dispersion observed in the DensePak velocity fields. These 20 km s^{-1} noncircular motions are actually lower limits. When baryons are included, the noncircular motions must increase by 5-10 km s^{-1}.

Kinematic axes that are not perpendicular and isovelocity contours that are kinked and twisted are a few examples of manifestations of noncircular motions in velocity fields. While the DensePak velocity fields do show some indications of noncircular motions, it is not obvious that they are as severe as 20 km s^{-1} or more. The constraints provided by the visual inspection of the velocity fields leads to our fourth question.

> ***Question 4:*** Can a modification to the NFW halo potential, such as the introduction of an asymmetry, simultaneously cause the NFW velocity field to appear solid-body and the NFW rotation curve to appear linearly rising?
>
> ***Short answer:*** Our simulations have so far been unable to produce such a velocity field and rotation curve simultaneously, although an NFW potential with a variable axis ratio seems to warrant further exploration.

Our analysis in Chapters 2-4 has shown that DensePak rotation curves, like long-slit and HI data, are not steep at small radii. The slow rise of the rotation curves seems to be an intrinsic feature of the LSB data. We have also found that DensePak velocity fields very often look solid-body. In contrast, NFW rotation curves are steeply rising and the velocity fields are distinctly pinched. We asked in Chapter 5 if it is possible for a cuspy NFW halo to look like both the observed rotation curve and velocity field data. Our

simulations show that while the NFW rotation curve can sometimes be "fixed," the pinch is very difficult to erase from the velocity field.

We found that a non-axisymmetric NFW potential with a constant axis ratio could get the mock rotation curves to match the data, but the potential ultimately had to be considered unsuccessful because of two reasons: 1) the statistics of ϕ, and 2) the appearance of the velocity fields. The simulations show that the elongated NFW potentials must point perpendicular to our line-of-sight, an orientation completely inconsistent with a random distribution of halo orientations on the sky. Equally problematic is that the NFW pinch remains clearly visible in the mock DensePak velocity fields. This kind of potential is able to produce the necessary noncircular motions discussed in Question 3, but they are still not large enough to get the shape of the isovelocity contours right.

A non-axisymmetric NFW potential with a variable axis ratio, however, did have some success at altering the mock velocity fields: the pinch of the isovelocity contours is replaced by a twist. These mock velocity fields are still not purely solid-body, but it seems this kind of modification to the axisymmetric NFW potential may move the fit results in the right direction. We say this cautiously, however, as this potential introduces several extra parameters and uncertainties that makes it difficult to test.

6.2 Impact of the DensePak Observations

Our investigation of the cusp-core problem has benefitted in many ways from the new DensePak velocity fields and rotation curves. The DensePak rotation curves have been able to address concerns of slit misplacement and beam smearing in previous data.

The new data have also been able to reduce the errors on the NFW and isothermal halo fit parameters. The DensePak velocity fields have been particularly important because of the constraints they put on the NFW halo. Noncircular motions cannot be added at whim to rotation curves without consideration of their impact on the observed velocity fields. Likewise, the velocity fields dictate what level of noncircular motions are reasonable. The solid-body DensePak velocity fields also provide a strong argument against the NFW halo. No assumptions go into making velocity fields - they are simply a presentation of the raw data. That they do not show the NFW pinch says a lot. It is currently popular to blame the cusp-core problem on halos that are triaxial and/or potentials that are non-axisymmetric. We have found the DensePak velocity fields very useful when testing the validity of such claims. Well-resolved velocity fields of LSB galaxies have and will continue to provide important constraints on the cusp-core problem.

6.3 Possible Future Work

The results presented in this dissertation show that there are still unanswered questions about galaxy formation in the context of CDM. To move forward, we must work to integrate observations into simulations, using the strengths of each to determine the behavior of dark matter on small scales. We must study the kinematics of galaxies using both observed velocity fields and simulated galaxy-halo systems.

The most current simulations follow massless test particles in a diskless triaxial halo (Hayashi & Navarro 2006). New simulations of increasing complexity that include various effects and processes to make the galaxy-halo systems as realistic as possible are

needed. Constraints from well-resolved velocity fields of LSB galaxies will help guide the initial conditions of these simulations as well as serve as comparisons to the simulation output.

It is also worthwhile to explore the idea that the most straightforward interpretation of the observations is correct: that cusps are really not there. It is possible that dark matter is not cold dark matter, but instead a variant that produces cored halos on small scales. Well-motivated alternative dark matter candidates to CDM should be considered.

Galaxy formation is a complicated process. There is plenty of exciting research still to be done.

Appendix A

Master List of Thesis Observations

Table A.1 lists all of the spectroscopic and photometric observations made during the course of this thesis, as well as complimentary observations made by collaborators. Thesis observations were made at the WIYN 3.5m, KPNO 4 m, and KPNO 2.1 m telescopes. The quality of the observations is also indicated in the table.

Table A.1: Master List of Thesis Observations

Galaxy	RA-DEC	Spectra			Imaging									names
	(J2000)	DPak	LSlit	HI	U	B	V	R	I	J	K	Hα	r	
Cam B	04:53:07.1	*(R)*												KK98 44
	+67:05:57.0	*(11/04)*												
D512-2	14:33:20.1												*(R)*	F512-1
	+26:59:50.0												*(3/06)*	
D514-2	14:33:20.1						*(R)*		*(R)*			*(R)*	*(R)*	
	+26:59:50.0						*(3/06)*		*(3/06)*			*(3/06)*	*(3/06)*	
D572-5	11:48:16.4	[R]					*(R)*		*(R)*			*(R)*	*(R)*	
	+18:38:33.0	[4/06]					*(3/06)*		*(3/06)*			*(3/06)*	*(3/06)*	
D575-1	12:51:46.1	[R]	R	E			*(R)*		*(R)*			*(R)*	*(R)*	F575-2
	+21:44:07.0	[4/06]	4/04				*(3/06)*		*(3/06)*			*(3/06)*	*(3/06)*	IC 3840
D575-2	12:52:21.1	[R]	R	E			*(R)*		*(R)*		J(s)	*(R)*	*(R)*	UGC 8011
	+21:37:46.0	[4/06]	4/04				*(3/06)*		*(3/06)*		5/04	*(3/06)*	*(3/06)*	
D575-5	12:55:40.5		R	E						S*	J(s),S*	J,*(R)*	*(R)*	F575-3
	+19:12:33.0		4/04							1/06	5/04,1/06	5/04,*(3/06)*	*(3/06)*	
D584-2	16:01:49.3						*(R)*		*(R)*			*(R)*	*(R)*	UGC 10140
	+18:43:15.0						*(3/06)*		*(3/06)*			*(3/06)*	*(3/06)*	
D631-7	07:57:01.8	[R]	R				*(R)*		*(R)*			*(R)*	*(R)*	UGC 4115
	+14:23:27.0	[4/06]	4/04				*(3/06)*		*(3/06)*			*(3/06)*	*(3/06)*	
D640-13	10:56:14.0	[R]	R				*(R)*		*(R)*			*(R)*	*(R)*	F640-V1
	+12:00:37.0	[4/06]	4/04				*(3/06)*		*(3/06)*			*(3/06)*	*(3/06)*	
D646-7	12:58:40.4	[R]										*(R)*	*(R)*	UGC 8091
	+14:13:03.0	[4/06]										*(3/06)*	*(3/06)*	DDO 155
D656-2	16:13:20.5						*(R)*		*(R)*			*(R)*	*(R)*	UGC 10281
	+17:11:34.0						*(3/06)*		*(3/06)*			*(3/06)*	*(3/06)*	
DDO 64	09:50:22.4	R,R	dBB 9									*(R)*	*(R)*	UGC 5272
	+31:29:26.0	4/04,4/06										*(3/06)*	*(3/06)*	
DDO 185	13:54:45.7	*(R)*	dBB			E	E	E	E		J(s)	J		UGC 8837
	+53:54:03.0	*(4/04)*									5/04	5/04		Holmb.IV
DDO 189	14:22:32.2	*(R)*	dBB			E	E	E	E			J		UGC 9211
	+45:23:02.0	*(4/04)*										5/04		
DDO 210	20:46:51.8		*(R)*											
	-12:50:52.5		*(8/04)*											
F469-2	22:57:19.5	*(R)*	R			R		R				*(R)*		F535-1
	+27:59:04.0	*(9/06)*	8/04			9/04		9/04				*(9/06)*		
F544-1	02:01:20.9											*R*		
	+19:58:51.0											*(9/06)*		
F563-1	08:55:06.9	R,R	MRdB	BMH				E		S*	J(s),S*	E,*(R)*	*(R)*	D563-4
	+19:44:58.0	4/04,4/06	dBB							1/06	1/05,1/06	*(3/06)*	*(3/06)*	

Continued on Next Page…

Table A.1 – Continued

Galaxy	RA-DEC	Spectra			Imaging									names
	(J2000)	DPak	LSlit	HI	U	B	V	R	I	J	K	Hα	r	
F563-V2	08:53:03.7	R		BMH	S	S	S		S	S*	J(s),S*	S,*(R)*	*(R)*	D563-2
	+18:26:09.0	4/04								1/06	1/05,1/06	*(3/06)*	*(3/06)*	
F568-3	10:27:20.3	R	MRdB	BMH		E	E	E	E	S*	S*	S		
	+22:14:22.0	4/04					S			1/06	1/06	E		
F583-1	15:57:27.5	R,R	MRdB	BMH		E	E	E	E		J(s)	S,*(R)*	*(R)*	D584-4
	+20:39:58.0	4/04,4/06									5/04	*(3/06)*	*(3/06)*	
F583-4	15:52:12.7	R,R	MRdB	BMH		E	E	E	E			*(R)*	*(R)*	
	+18:47:06.0	4/04,4/06										*(3/06)*	*(3/06)*	
F750-4	23:44:20.2	*(R)*	R			R		R						
	+10:07:05.0	*(11/04)*	8/04			9/04		9/04						
KK98 251	20:30:32.9	*(R)*	R			R		R						
	+60:21:17.0	*(9/05)*	8/04			9/04		9/04						
NGC 784	02:01:16.9	*(R)*				R		R						UGC 1501
	+28:50:14.1	*(11/04,9/05)*				9/04		9/04						
NGC 959	02:32:23.9	R										*(R)*		UGC 2002
	+35:29:41.0	9/06										*(9/06)*		
NGC 1156	02:59:42.8	*(R)*				R		R						UGC 2455
	+25:14:28.2	*(11/04)*				9/04		9/04						
NGC 3104	10:03:57.4	*(R)*												UGC 5414
	+40:45:24.9	*(11/04)*												
NGC 4395	12:25:48.9	R	dBB			E	E	E	E			E		UGC 7524
	+33:32:48.3	4/04												
NGC 4455	12:28:44.1	*(R)*	dBB			E	E	E	E		J(s)	J		UGC 7603
	+22:49:21.0	*(4/04)*									5/04	5/04		
NGC 7137	21:48:13.0	R				*(R)*		*(R)*				*(R)*		UGC 11815
	+22:09:34.0	8/06				*(9/06)*		*(9/06)*				*(9/06)*		
NGC 7292	22:28:25.8	*(R)*	R			R		R				*(R)*		UGC 12048
	+30:17:33.0	*(8/06)*	8/04			9/04,*(9/06)*		9/04,*(9/06)*				*(9/06)*		
UGC 17	00:03:43.3		R			R		R						DDO 222
	+15:13:06.0		8/04			9/04		9/04						
UGC 128	00:13:50.9	R									J(s)	J,*(R)*		
	+35:59:39.0	9/06									10/03	11/03,*(9/06)*		
UGC 156	00:16:48.1					R		R						
	+12:20:53.0					9/04		9/04						
UGC 191	00:20:05.2	R										*(R)*		DDO 002
	+10:52:48.0	9/06										*(9/06)*		
UGC 477	00:46:13.1	R	R			R		R						
	+19:29:23.7	11/04	8/04			9/04		9/04						

Continued on Next Page…

Table A.1 – Continued

Galaxy	RA-DEC	Spectra			Imaging									names
	(J2000)	DPak	LSlit	HI	U	B	V	R	I	J	K	Hα	r	
UGC 891	01:21:18.9	*(R)*				R		R						DDO 10
	+12:24:43.0	*(9/05)*				9/04		9/04						
UGC 1176	01:40:09.9					R		R						DDO 13
	+15:54:17.0					9/04		9/04						
UGC 1195	01:42:27.0					R		R						IC 148
	+13:58:37.3					9/04		9/04						
UGC 1281	01:49:32.4	R	dBB			R		R						
	+32:35:10.3	11/04,9/05				9/04		9/04						
UGC 1551	02:03:37.5	R				R		R				*(R)*		
	+24:04:32.0	8/06,9/06				9/06		9/06				*(9/06)*		
UGC 2014	02:32:54.0					R		R						DDO 22
	+38:40:50.1					9/04		9/04						
UGC 2017	02:32:45.2					R		R						F415-3
	+28:50:26.9					9/04		9/04						
UGC 2034	02:33:42.9	*(R)*				R		R				R		DDO 24
	+40:31:41.0	*(8/06,9/06)*				9/06		9/06				9/06		
UGC 2053	02:34:29.3	*(R)*				R		R				*(R)*		DDO 26
	+29:44:59.4	*(9/06)*				9/04		9/04				*(9/06)*		
UGC 2259	02:47:55.4					R		R		J	J(s)	J		
	+37:32:18.6					9/04		9/04		10/03	10/03	5/04		
UGC 2684	03:20:23.7	*(R)*												
	+17:17:45.1	*(11/04)*												
UGC 4325	08:19:20.5	R,R	dBB									*(R)*	*(R)*	NGC 2552
	+50:00:35.0	4/04,4/06										*(3/06)*	*(3/06)*	
UGC 4543	08:43:21.6	*(R)*												
	+45:44:08.4	*(11/04)*												
UGC 4787	09:07:34.9	*(R)*										*(R)*	*(R)*	
	+33:16:36.0	*(11/04)*										*(3/06)*	*(3/06)*	
UGC 5750	10:35:45.1	R	MRdB					E			J(s)	E,*(R)*	*(R)*	
	+20:59:24.0	4/04	dBB								1/05	J5/04,*(3/06)*	*(3/06)*	
UGC 11583	20:30:15.3	*(R)*	MRdB			R,J	J	R,J			J(s)	J		KK98 250
	+60:26:25.0	*(9/05)*				9/04,6/03	6/03	9/04,6/03			10/03	11/03		
UGC 11820	21:49:30.6	R				R		R		J	J(s)	J,R		
	+14:13:01.3	8/06				9/06		9/06		10/03	10/03	5/04.9/06		
UGC 11944	22:12:00.7	*(R)*									J(s)	J,*(R)*		
	+17:54:10.0	*(9/06)*									10/03	5/04,*(9/06)*		
UGC 12082	22:34:11.0	*(R)*	R			R		R				*(R)*		DDO 213
	+32:51:43.8	*(8/06)*	8/04			9/04		9/04				*(9/06)*		

Continued on Next Page…

Table A.1 – Continued

Galaxy	RA-DEC	Spectra			Imaging									names
	(J2000)	DPak	LSlit	HI	U	B	V	R	I	J	K	Hα	r	
UGC 12212	22:50:30.3	*(R)*	R			R		R				*(R)*		
	+29:08:18.4	*(9/06)*	8/04			9/04		9/04				*(9/06)*		
UGC 12344	23:04:59.9	*(R)*	R			R		R						
	+18:42:12.0	*(11/04,9/05)*	8/04			9/04		9/04						
UGC 12613	23:28:36.3		*(R)*											DDO 216
	+14:44:34.5		*(8/04)*											
UGC 12632	23:29:58.7	*(R)*	R			R		R				R		DDO 217
	+40:59:24.8	*(8/06)*	8/04			9/04		9/04				9/06		
UGC 12713	23:38:14.7	*(R)*	R			R		R						
	+30:42:33.2	*(11/04)*	8/04			9/04		9/04						
UGC 12791	23:48:49.4	*(R)*	R			R		R						DDO 220
	+26:13:14.0	*(11/04)*	8/04			9/04		9/04						
WLM	00:01:58.2		R			R		R						DDO 221
	-15:27:39.3		8/04			9/04		9/04						

Note. – DensePak and Long slit: *(Unusable velocity field or long slit)*, [Observed in bad weather]. Imaging: *(Not photometric)*; 9/04 maybe photometric, 3/06 NOT photometric, 9/06 NOT photometric except maybe Night 1. R=Rachel Kuzio de Naray. J=Ji Hoon Kim; J(s) under K-band means *short*. S=Stacy McGaugh. E=W.J.G. de Blok. MRdB=McGaugh, Rubin & de Blok 2001, ApJ, 122, 2381. dBB=de Blok & Bosma 2002, A&A, 385, 816. BMH=de Blok, McGaugh & van der Hulst 1996, MNRAS, 283, 18. S*=Jim Schombert & Stacy McGaugh and is SQIID JHK.

Appendix B

BVRI and Hα Imaging at the KPNO 2.1 m Telescope

During the course of this thesis, 16 nights were spent at the KPNO 2.1 m telescope obtaining *BVRI* and Hα images of LSB and dwarf galaxies. Unfortunately, almost all of these nights were mostly to completely cloudy and the data are not photometric. In this Appendix we present the images obtained for the galaxies whose DensePak velocity fields have been analyzed in Chapters 2 and 3. All of the galaxies that were imaged are in listed in Table A.1. The images have been reduced following standard procedures (bias subtraction, flat fielding, etc.) using the appropriate IRAF tasks. Two images were taken in each filter to correct for cosmic rays. Total exposure times were as follows: 1200 s in *B*, 1200 s in *V*, 600 s in *R*, 600 s in *I*, and 1800 s in Hα. The images are 5 arcmin on a side, and are displayed with North up and East to the left. The stretch of the greyscale has been optimized for each image so that faint features can be seen.

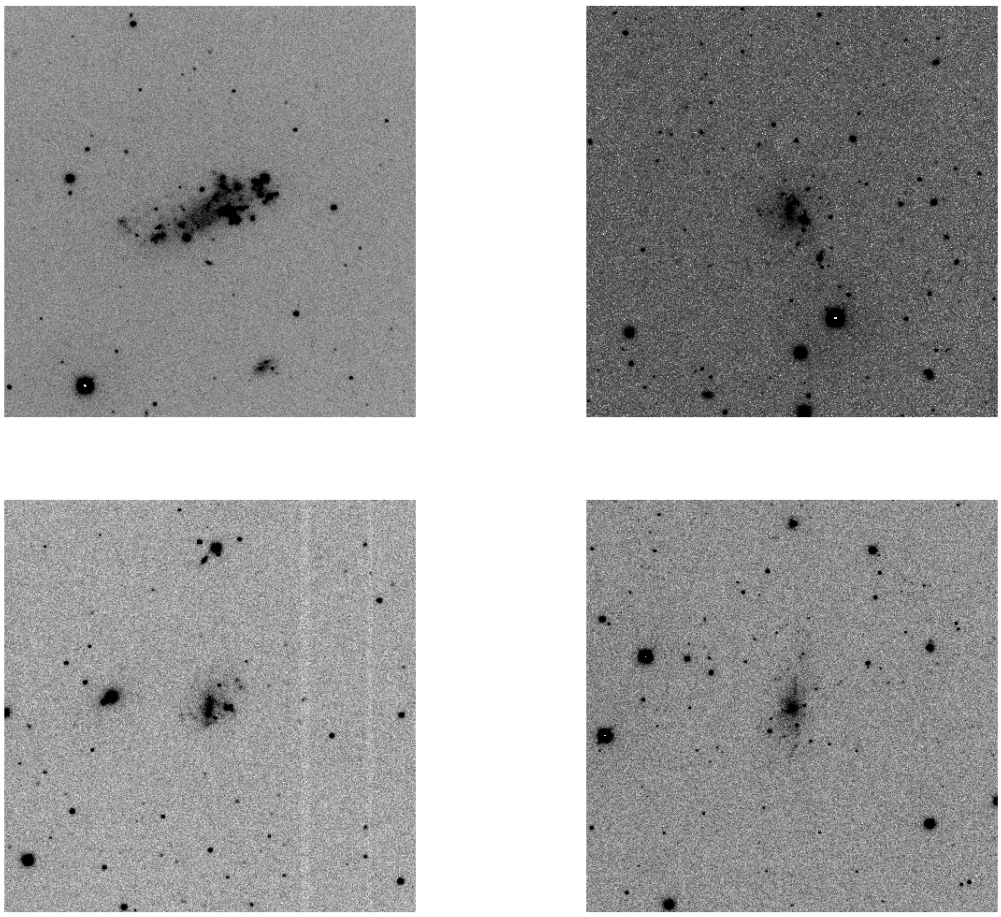

Figure B.1: – Clockwise from top left: Hα image of DDO 64, F563-1, F583-1, and F563-V2. Images are 5 arcmin on a side. North is up; East is to the left.

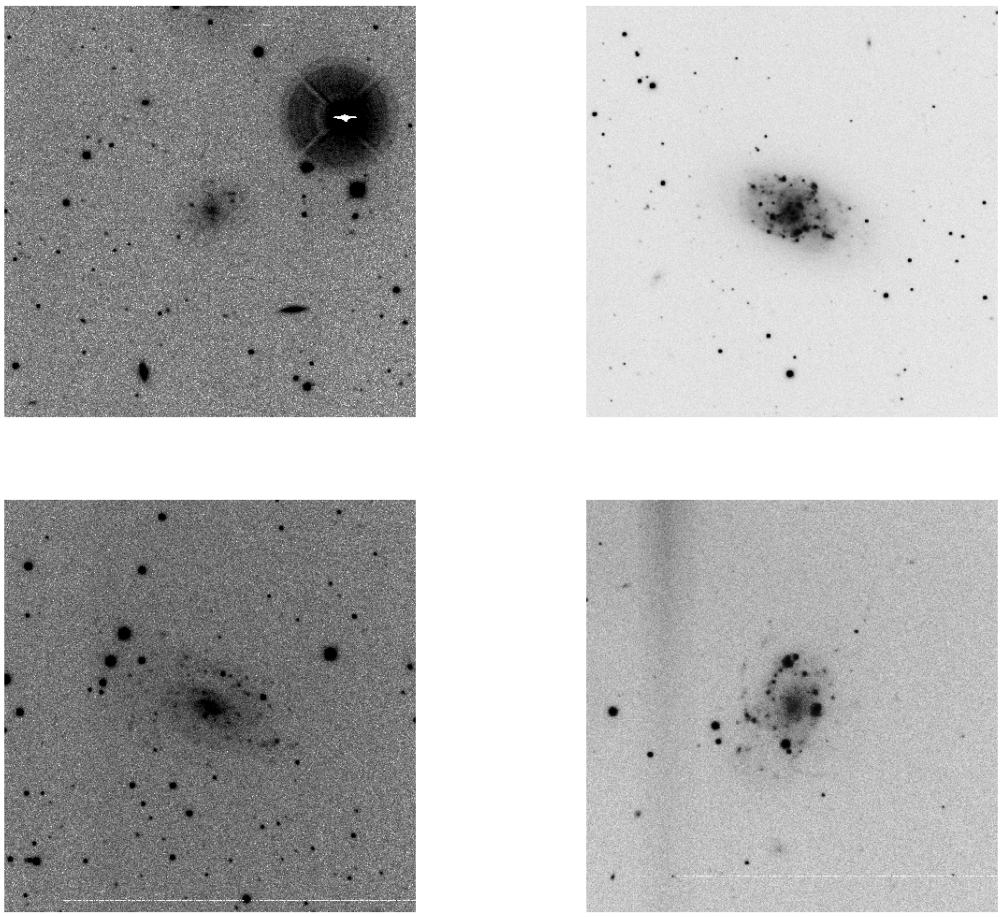

Figure B.2: – Clockwise from top left: Hα image of F583-4, NGC 959, UGC 191, and UGC 128. Images are 5 arcmin on a side. North is up; East is to the left.

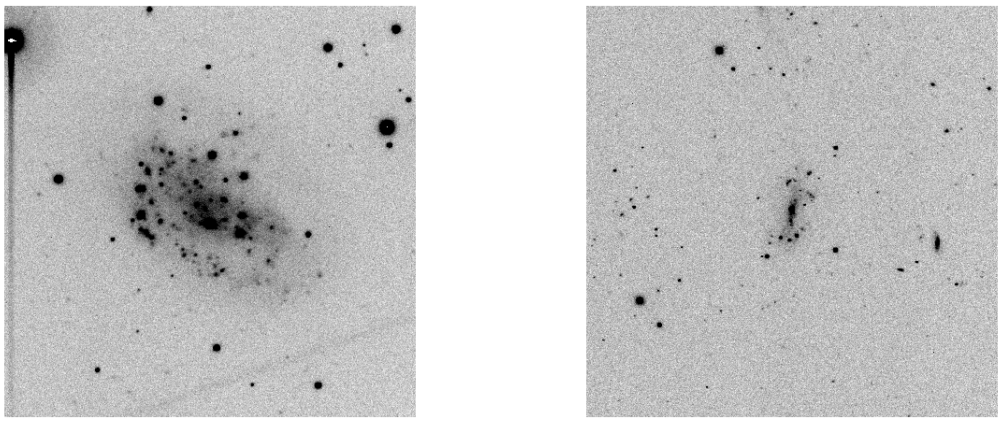

Figure B.3: – Hα image of UGC 4325 (left) and UGC 5750 (right). Images are 5 arcmin on a side. North is up; East is to the left.

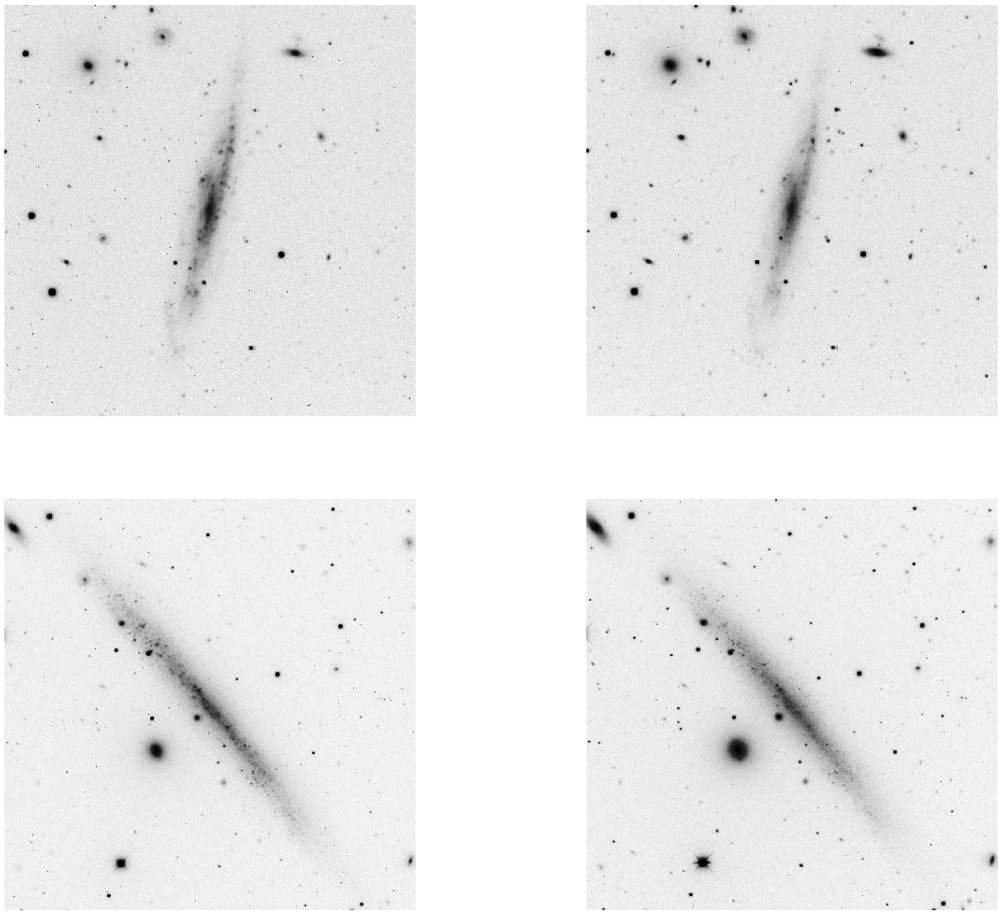

Figure B.4: – UGC 477 in *B* (top left) and *R* (top right); UGC 1281 in *B* (bottom left) and *R* (bottom right). Images are 5 arcmin on a side. North is up; East is to the left.

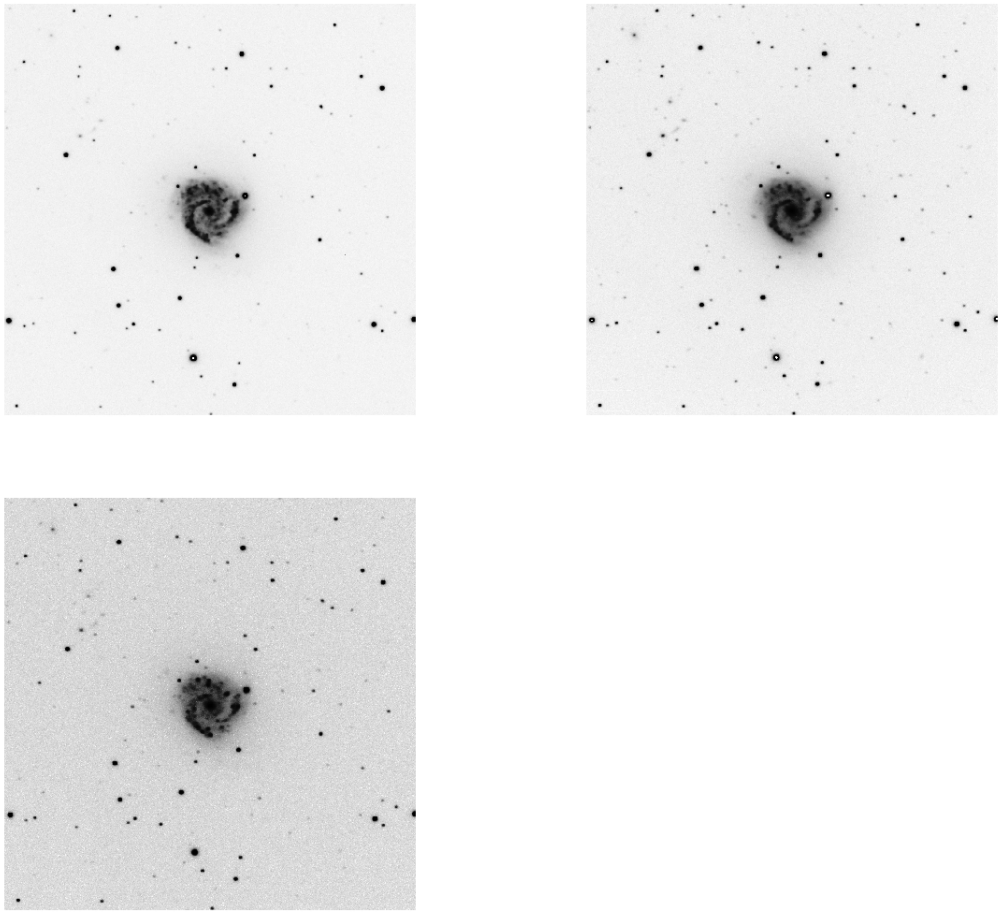

Figure B.5: – NGC 7137 in *B* (top left) and *R* (top right) and Hα (bottom left). Images are 5 arcmin on a side. North is up; East is to the left.

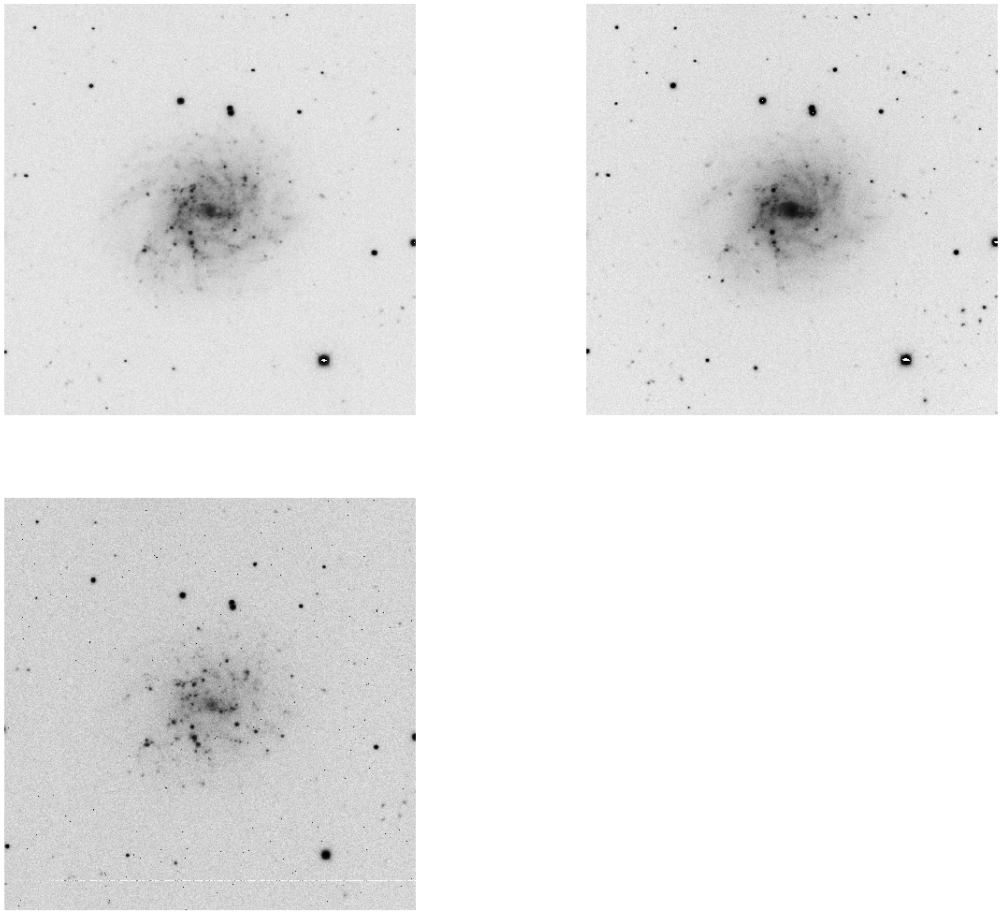

Figure B.6: – UGC 1551 in *B* (top left) and *R* (top right) and Hα (bottom left). Images are 5 arcmin on a side. North is up; East is to the left.

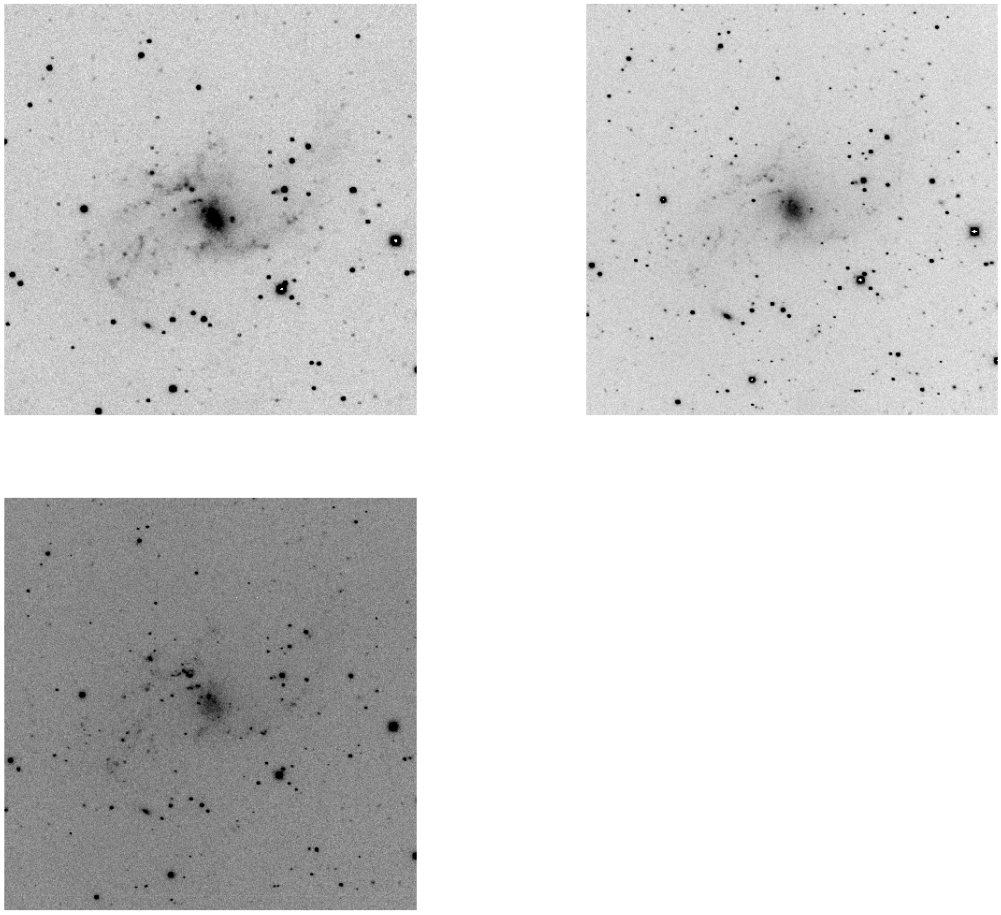

Figure B.7: – UGC 11820 in *B* (top left) and *R* (top right) and Hα (bottom left). Images are 5 arcmin on a side. North is up; East is to the left.

Appendix C

DensePak Data Reduction Steps

C.1 Initial DensePak Reduction in IRAF

1. Remove any files marked as BAD at the telescope

2. Check values of trimsec and biassec in fileheader:

    imhead filename l+ *and* implot filename

3. Load `noao.imred.ccdred`

    setinstrument fibers

    check that output type is “real”

    :q

    in params for ccdproc:

        biassec = image

        enter values for trimsec

    :q

4. Check file types with ccdlist *.fits

5. Combine the zero (bias) frames with epar zerocombine

    input = n#*.fits

    output = ZeroN#

    :go

6. Run ccdproc on ALL images for overscan, bias, trim and zero correction

epar ccdproc

images = n#*.fits

overscan = yes

trim = yes

zerocor = yes

darkcor = no

flatcor = no

illumcor = no

check values of biassec and trimsec

enter name of combined zero from step 5

:go

look at a few with “yes”; exit with “NO”

7. Combine the dome flats

epar flatcombine

use crreject

output = FlatN#

readnoise = NOISE_12 (check this)

gain = GAIN_12 (check this)

:go

C.2 DensePak Reduction with `dohydra`

1. Create an aperture identification file “apid.txt” with 3 columns:

   fiber #, type id (−1=broken/unused; 0=sky; 1=object), title

   Sky = 8, 32, 68, 90

   Unused = 23, 28

   Broken = 35*, 36, 40, 46, 59, 93

2. Load `noao.imred.hydra`

   epar dohydra

      objects = @gal.txt (need to put multiple files in this list)

      apref and flat = FlatN#.fits

      arcs1 = use before and after CuAr lamps;

         in wavelength calibration, hν increases to right, λ to left

      readnoise = NOISE_12 (check this)

      gain = GAIN_12 (check this)

      fibers=97; width=12; minsep=8; maxsep=12

      yes to everything except skyalign, skysubtract, redo, batch, listonly

      − do not sky subtract because no guarantee that fibers do not fall
        within galaxy

      − to do a list of spectra, redo must be set to no, otherwise the ap. ids
        get messed up and it fails

   :go

3. For the very first reduction of the night:

Resize ap. for FlatN#? yes

Edit ap. for FlatN#? yes

Check that ap # are correct: to zoom in Shift-X;

to redraw: r; when done, q

Fit trace? yes

Smooth scattered light? yes

Look and then q quit; Look again and q quit

Wait awhile for it to Create response, Extract flat

Fit and ratio flat: Look and then q

Determine λ in CuAr:

mark with m: 7030.25, 6871.29, 6752.83, 6677.28

type l then q

Fit disp. func? NO

Change λ coordinate assignment? NO

Fit scattered for object? no

Smooth object? no

Splot object? yes

go forward with ‘)’ and backwards with ‘(’; q to quit

4. All others in same night:

   First step is to determine λ for new CuAr files

   Rest of steps are same for the object frames

5. Combine images with `scombine` (for spectra with different λ ranges):

   input = @gal.txt

   output = galaxyn#p#.fits (night, position)

   group = apertures

   combine = average

   reject = crrject

   first = no

   w1 ... nw = INDEF

   scale = mode

   lsigma, hsigma = 2.5

   rdnoise = NOISE_12 (check this)

   gain = GAIN_12 (check this)

display all images & check that output is ok

6. Can use `specplot` to plot multiple spectra on one plot

C.3 Measuring Lines

1. Look up systemic velocities to get rough idea of λ of Hα, [NII] and [SII]
2. Look for Sky lines close to these wavelengths
3. Order galaxies by priority
4. Use `noao.imred.hydra.splot` to measure lines:

    Create a logfile galaxyn#p#.log (epar splot: save_fi)

    a to expand

    c to clear and redraw full view

    r to clear and redraw expanded view

    k to measure lines

) to cycle to next fiber

5. Cycle through and note fibers with particularly strong signal

C.4 DensePak Fiber Positions

In Table C.1 we present the DensePak aperture identifications that are needed for `dohydra` data reduction as described in Appendix C.2. In Table C.2 we present the relative positions of the DensePak fibers. Fiber spacing has been determined by centering a bright star in a fiber and repeatedly shifting between fibers and across the array. Fibers are $3''$ and fiber separation is $3''.84$. In Figure C.1 we present a mapping of the DensePak fibers.

Table C.1. Aperture Identification File

*Ap.	Fiber		*Ap.	Fiber	
1	1		54	61	
2	2		55	62	
.	.		56	63	
8	8	Sky	57	64	
.	.		58	65	
22	22		59	66	
23	24		60	67	
24	25		61	68	Sky
25	26		62	69	
26	27		63	70	
27	29		64	71	
28	30		65	72	
29	31		66	73	
30	32	Sky	67	74	
31	33		68	75	
32	34		69	76	
33	37		70	77	
34	38		71	78	
35	39		72	79	
36	41		73	80	
37	42		74	81	
38	43		75	82	
39	44		76	83	
40	45		77	84	
41	47		78	85	
42	48		79	86	
43	49		80	87	
44	50		81	88	
45	51		82	89	
46	52		83	90	Sky
47	53		84	91	
48	54		85	92	
49	55		86	94	
50	56		87	95	
51	57		88	96	
52	58		89	97	
53	59				

Note. — DensePak aperture identification needed for reduction in `dohydra`.

Table C.2. Relative DensePak Fiber Positions

Fiber	Xpos (arcsec)	Ypos (arcsec)	Fiber	Xpos (arcsec)	Ypos (arcsec)
1	-5.76	-16.65	52	13.44	3.33
2	-1.92	-16.65	53	17.28	3.33
3	1.92	-16.65	54	-7.68	6.66
4	5.76	-16.65	55	-3.84	6.66
5	9.60	-16.65	56	0.00	6.66
6	13.44	-16.65	57	3.84	6.66
7	17.28	-16.65	58	7.68	6.66
9	-7.68	-13.32	60	15.36	6.66
10	-3.84	-13.32	61	-5.76	9.99
11	0.00	-13.32	62	-1.92	9.99
12	3.84	-13.32	63	1.92	9.99
13	7.68	-13.32	64	5.76	9.99
14	11.52	-13.32	65	9.60	9.99
15	15.36	-13.32	66	13.44	9.99
16	-5.76	-9.99	67	17.28	9.99
17	-1.92	-9.99	69	-7.68	13.32
18	1.92	-9.99	70	-3.84	13.32
19	5.76	-9.99	71	0.00	13.32
20	9.60	-9.99	72	3.84	13.32
21	13.44	-9.99	73	7.68	13.32
22	17.28	-9.99	74	11.52	13.32
24	-7.68	-6.66	75	15.36	13.32
25	-3.84	-6.66	76	-5.76	16.65
26	0.00	-6.66	77	-1.92	16.65
27	3.84	-6.66	78	1.92	16.65
29	7.68	-6.66	79	5.76	16.65
30	11.52	-6.66	80	9.60	16.65
31	15.36	-6.66	81	13.44	16.65
33	-5.76	-3.33	82	17.28	16.65
34	-1.92	-3.33	83	-7.68	19.98
37	9.60	-3.33	84	-3.84	19.98
38	13.44	-3.33	85	0.00	19.98
39	17.28	-3.33	86	3.84	19.98
41	-3.84	0.00	87	7.68	19.98
42	0.00	0.00	88	11.52	19.98
43	3.84	0.00	89	15.36	19.98
44	7.68	0.00	91	-5.76	23.31
45	11.52	0.00	92	-1.92	23.31
47	-5.76	3.33	94	5.76	23.31
48	-1.92	3.33	95	9.60	23.31
49	1.92	3.33	96	13.44	23.31
50	5.76	3.33	97	17.28	23.31
51	9.60	3.33			

Note. — Relative fiber positions in arcsec. To put Fiber 50 at the center, subtract $5''.76$ from the x-positions and $3''.33$ from the y-positions.

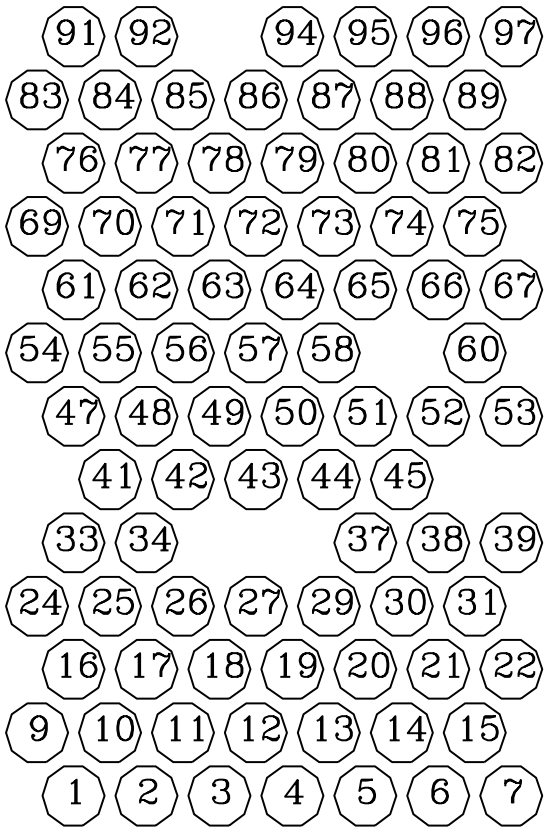

Figure C.1: – Map of DensePak fibers. Sky fibers 8, 32, 68, and 90 are outside of the main array and are not shown.

Bibliography

Avila-Reese, V., Firmiani, C., & Hernandez, X. 1998, ApJ, 505, 37

Baggett, W. E., Baggett, S. M., & Anderson, K. S. J. 1998, AJ, 116, 1626

Begeman, K. 1989, A&A, 223, 47

Bell, E. F., McIntosh, D. H., Katz, N., & Weinberg, M. D. 2003, ApJS, 149, 289

Biviano, A., & Girardi, M. 2003, ApJ, 585, 205

Blais-Ouellette, S., Amram, P., & Carignan, C. 2001, AJ, 121, 1952

Bolatto, A. D., Simon, J. D., Leroy, A., & Blitz, L. 2002, ApJ, 565, 238

Borriello, A., & Salucci, P. 2001, MNRAS, 323, 285

Bosma, A. 2004, IAUS, 220, 39

Bullock, J. S., Kolatt, T. S., Sigad, Y., Somerville, R. S., Kravtsov, A. V., Klypin, A. A., Primack, J. R., & Dekel, A. 2001, MNRAS, 321, 559

Clowe, D., Bradač, M., Gonzalez, A. H., Markevitch, M., Randall, S. W., Jones, C., & Zaritsky, D. 2006, ApJ, 648, L109

Cole, S., & Lacey, C. 1996, MNRAS, 281, 716

Cole, S., et al. 2005, MNRAS, 362, 505

Côté, S., Carignan, C., & Freeman, K. C. 2000, AJ, 120, 3027

Croft, R. A. C., Weinberg, D. H., Bolte, M., Burles, S., Hernquist, L., Katz, N., Kirkman, D., Tytler, D. 2002, ApJ, 581, 20

de Blok, W. J. G. 2004, in IAU Symp. 220, Dark Matter in Galaxies, ed. S. D. Ryder, D. J. Pisano, M. A. Walker, & K. C. Freeman (San Francisco: ASP), 69

de Blok, W. J. G., & Bosma, A. 2002, A&A, 385, 816 (BB02)

de Blok, W. J. G., Bosma, A., & McGaugh, S. S. 2003, MNRAS, 340, 657

de Blok, W. J. G., & McGaugh, S. S. 1996, ApJ, 469, L89

———- . 1997, MNRAS, 290, 533

de Blok, W. J. G., McGaugh, S. S., Bosma, A., & Rubin, V. C. 2001, ApJ, 552, L23

de Blok, W. J. G., McGaugh, S. S., & Rubin, V. C. 2001, AJ, 122, 2396 (BMR01)

de Blok, W. J. G., McGaugh, S. S., & van der Hulst, J. M. 1996, MNRAS, 283, 18 (BMH96)

de Blok, W. J. G., & van der Hulst, J. M. 1998, A&A, 336, 49

de Blok, W. J. G., van der Hulst, J. M., & Bothun, G. D. 1995, MNRAS, 274, 235

de Jong, R. S. 1996, A&AS, 118, 557

de Naray, R. K., McGaugh, S. S., & de Blok, W. J. G. 2004, MNRAS, 355, 887

Diemand, J., Zemp, M., Moore, B., Stadel, J., & Carollo, M. 2005, MNRAS, 364, 665

Dubinski, J. 1994, ApJ, 431, 617

Flores, R. A., & Primack, J. R. 1994, ApJ, 427, L1

Fuchs, B. 2003, Ap&SS, 284, 719

Garrido, O., Marcelin, M., Amram, P., & Boulesteix, J. 2002, A&A, 387, 821

Gentile, G., Burkert, A., Salucci, P., Klein, U., & Walter, F. 2005, ApJ, 634, L145

Gentile, G., Salucci, P., Klein, U., & Granato, G. L. 2007, MNRAS, 375, 199

Gentile, G., Salucci, P., Klein, U., Vergani, D., & Kalberla, P. 2004, MNRAS, 351, 903

Gnedin, O. Y., Kravtsov, A. V., Klypin, A. A., & Nagai, D. 2004, ApJ, 616, 16

Goerdt, T., Moore, B., Read, J. I., Stadel, J., Zemp, M. 2006, MNRAS, 368, 1073

Guth, A. H. 1981, Phys. Rev. D, 23, 347

Hayashi, E., et al. 2004, MNRAS, 355, 794

Hayashi, E., & Navarro, J. F. 2006, MNRAS, 373, 1117

Hayashi, E., Navarro, J. F., & Springel, V. 2007, MNRAS, 377, 50

Heraudeau, P., & Simien, F. 1996, A&AS, 118, 111

Hogan, C. J., & Dalcanton, J. J. 2000, PhysRevD, 62, 063511

James, P. A., et al. 2004, A&A, 414, 23

Jing, Y. P., & Suto, Y. 2000, ApJ, 529, L69

Klypin, A., Kravtsov, A. V., Bullock, J. S., & Primack, J. R. 2001, ApJ, 554, 903

Kregel, M., van der Kruit, P. C., & Freeman, K. C. 2004, MNRAS, 351, 1247

Kuzio de Naray, R., McGaugh, S. S., de Blok, W. J. G., & Bosma, A. 2006, ApJS, 165, 461

Marchesini, D., D'Onghia, E., Chincarini, G., Firmani, C., Conconi, P., Molinari, E., & Zacchei, A. 2002, ApJ, 575, 801

McGaugh, S. S. 2005, ApJ, 632, 859

McGaugh, S. S., Barker, M. K., & de Blok, W. J. G. 2003, ApJ, 584, 566

McGaugh, S. S., & de Blok, W. J. G. 1998, ApJ, 499, 41

McGaugh, S. S., de Blok, W. J. G., Schombert, J. M., Kuzio de Naray, R., & Kim, J. H. 2007, ApJ, 659, 149

McGaugh, S. S., Rubin, V. C., & de Blok, W. J. G. 2001, AJ, 122, 2381 (MRB01)

McGaugh, S. S., Schombert, J. M., & Bothun, G. D. 1995, AJ, 109, 2019

Mihos, J. C., Spaans, M., & McGaugh, S. S. 1999, ApJ, 515, 89

Moore, B. 1994, Nature, 370, 629

Moore, B., Ghingna, S., Governato, F., Lake, G., Quinn, T., Stadel, J., & Tozzi, P. 1999a, ApJ, 524, L19

Moore, B., Quinn, T., Governato, F., Stadel, J., Lake, G. 1999b, MNRAS, 310, 1147

Navarro, J. F., Frenk, C. S., & White, S. D. M. 1996, ApJ, 462, 563

———- . 1997, ApJ, 490, 493

Navarro, J.F., et al. 2004, MNRAS, 349, 1039

Nilson, P. 1973, Uppsala General Catalogue of Galaxies, Uppsala Astron. Obs. Ann. 6

Noordermeer, E., Sparke, L. S., & Levine, S. E. 2001, MNRAS, 328, 1064

Osterbrock, D. E., Fulbright, J. P., Martel, A. R., Keane, M. J., Trager, S. C., & Basri, G. 1996, PASP, 108, 277

Pickering, T. E., Impey, C. D., van Gorkom, J. H., & Bothun, G. D. 1997, AJ, 114, 1858

Pickering, T. E., van Gorkom, J. H., Impey, C. D., & Quillen, A. C. 1999, AJ, 118, 765

Pisano, D. J., Wilcots, E. M., & Elmegreen, B. G. 1998, AJ, 115, 975

Power, C., Navarro, J. F., Jenkins, A., Frenk, C. S., White, S. D. M., Springel, V., Stadel, J., & Quinn, T. 2003, MNRAS, 338, 14

Reed, D., Gardner, J., Quinn, T., Stadel, J., Fardal, M., Lake, G., & Governato, F. 2003, MNRAS, 346, 565

Regan, M. W., Thornley, M. D., Helfer, T. T., Sheth, K., Wong, T., Vogel, S. N., Blitz, L., & Bock, D. C. J. 2001, ApJ, 561 218

Rhee, G., Valenzuela, O., Klypin, A., Holtzman, J., & Moorthy, B. 2004, ApJ, 617, 1059

Ricotti, M. 2003, MNRAS, 344, 1237

Rines, K., Geller, M. J., Diaferio, A., Kurtz, M. J., & Jarrett, T. H. 2004, AJ, 128, 1078

Rosenberg, J. L., & Schneider S. E. 2003, ApJ, 585, 256

Schombert, J. M., Bothun, G. D., Impey, C. D., & Mundy, L. G. 1990, AJ, 100, 1523

Sellwood, J. A., & McGaugh, S. S. 2005, ApJ, 634, 70

Simon, J. D., Bolatto, A. D., Leroy, A., & Blitz, L. 2003, ApJ, 596, 957

Simon, J. D., Bolatto, A. D., Leroy, A., Blitz, L., & Gates, E. 2005, ApJ, 621, 757

Spekkens, K., Giovanelli, R., & Haynes, M. P. 2005, AJ, 129, 2119

Spekkens, K., & Sellwood, J. A. 2007, ApJ, in press (astro-ph/0703688)

Spergel, D. N., et al. 2007, ApJS, 170, 377

Springel, V., et al. 2005, Nature, 435, 629

Stil, J. 1999, Ph.D. Thesis, University of Leiden

Strigari, L. E., Kaplinghat, M., & Bullock, J. S. 2007, PhysRevD, 75, 061303

Swaters, R. A. 1999, Ph.D. Thesis, University of Groningen

Swaters, R. A., & Balcells, M. 2002, A&A, 390, 863

Swaters, R. A., Madore, B. F., & Trewhella, M. 2000, ApJ, 531, L107

Swaters, R. A., Madore, B. F., van den Bosch, F. C., & Balcells, M. 2003a, ApJ, 583, 732

Swaters, R. A., van Albada, T. S., van der Hulst, J. M., & Sancisi, R. 2002, A&AP, 390, 829

Swaters, R. A., Verheijen, M. A. W., Bershady, M. A., & Andersen, D. R. 2003b, ApJ, 587, L19

Tegmark, M., et al. 2004, Phys. Rev. D, 69, 103501

Teuben, P. J. 1995, in ASP Conf. Ser. 77, Astronomical Data Analysis Software and Systems IV, ed. R. Shaw, H. E. Payne, & J. J. E. Hayes (San Francisco: ASP), 398

Tully, R. B. 1988, Nearby Galaxies Catalogue (Cambridge: Cambridge Univ. Press)

van den Bosch, F. C., Robertson, B. E., Dalcanton, J. J., & de Blok, W. J. G. 2000, AJ, 119, 1579

van den Bosch, F. C., & Swaters, R. A. 2001, MNRAS, 325, 1017

van der Hulst, J. M., Skillman, E. D., Smith, T. R., Bothun, G. D., McGaugh, S. S., & de Blok, W. J. G. 1993, AJ, 106, 548

van der Kruit, P. C., & Searle, L. 1981, A&AP, 95, 105

van Zee, L. 2000, AJ, 119, 2757

van Zee, L., & Haynes, M. P. 2006, ApJ, 636, 214

van Zee, L., Haynes, M. P., Salzer, J. J., & Broeils, A. H. 1997, AJ, 113, 1618

Verheijen, M., & de Blok, W. J. G. 1999, Ap&SS, 269, 673